

**UNIVERSIDADE FEDERAL DE SANTA CATARINA  
PROGRAMA DE PÓS-GRADUAÇÃO  
EM ENGENHARIA ELÉTRICA**

Rafael Gonçalves Licursi de Mello

**MODERN TECHNIQUES TO LOCATE AND IDENTIFY  
RADARS WITH LOW VOLUME, WEIGHT, COSTS AND  
PROCESSING CAPABILITIES**

Dissertação submetida ao Programa de Pós-Graduação da Universidade Federal de Santa Catarina para a obtenção do Grau de Mestre em Engenharia Elétrica.

Orientador: Prof. Dr. Fernando Rangel de Sousa.

Florianópolis  
2018

Ficha de identificação da obra elaborada pelo autor,  
através do Programa de Geração Automática da Biblioteca Universitária da UFSC.

Mello, Rafael Gonçalves Licursi de  
Modern techniques to locate and identify radars  
with low volume, weight, costs and processing  
capabilities / Rafael Gonçalves Licursi de Mello ;  
orientador, Fernando Rangel de Sousa, 2018.  
129 p.

Dissertação (mestrado) - Universidade Federal de  
Santa Catarina, Centro Tecnológico, Programa de Pós  
Graduação em Engenharia Elétrica, Florianópolis, 2018.

Inclui referências.

1. Engenharia Elétrica. 2. Radar Signal  
Processing. 3. Direction Finding. 4. Pattern  
Recognition. 5. Electronic Warfare. I. Sousa,  
Fernando Rangel de. II. Universidade Federal de  
Santa Catarina. Programa de Pós-Graduação em  
Engenharia Elétrica. III. Título.

Rafael Gonçalves Licursi de Mello

**MODERN TECHNIQUES TO LOCATE AND IDENTIFY  
RADARS WITH LOW VOLUME, WEIGHT, COSTS AND  
PROCESSING CAPABILITIES**

Esta Dissertação foi julgada adequada para obtenção do Título de  
“Mestre” e aprovada em sua forma final pelo Programa de  
Pós-Graduação em Engenharia Elétrica.


Florianópolis, 25 de maio de 2018.



---


Prof. Marcelo Lobo Heldwein, Dr.  
Coordenador do Curso

**Banca Examinadora:**



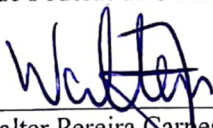
---

Prof. Fernando Rangel de Sousa, Ph.D.  
Orientador  
Universidade Federal de Santa Catarina – UFSC




---

Prof. Eduardo Augusto Bezerra, Dr.  
Universidade Federal de Santa Catarina – UFSC



---

Prof. Walter Pereira Carpes Junior, Ph.D.  
Universidade Federal de Santa Catarina – UFSC



---

Prof. Cynthia Cristina de Barros Junqueira, Dr.  
Universidade Estadual de Campinas – UNICAMP (Videoconferência)

*Prof. Marcelo Lobo Heldwein, Dr.  
Coordenador do Programa de  
Pós-Graduação em Engenharia Elétrica  
UFSC*



Este trabalho é dedicado àqueles que  
nele acreditaram.



## AGRADECIMENTOS

Um grande empenho foi necessário para o desenvolvimento desta pesquisa. Um empenho de muitas pessoas.

Meus pais, Luiz Antônio Licursi de Mello e Leni Maria Gonçalves Licursi de Mello, deram-me a oportunidade de estudar e de crescer em um ambiente saudável.

Minha noiva, Monike Mary Clasen, apoiou-me nas horas difíceis, e compreendeu quando tivemos que abrir mão de nossos momentos.

Meu Professor Orientador, o Prof. Dr. Fernando Rangel de Sousa, teve a sabedoria para direcionar minhas energias para as áreas corretas, de forma a construirmos conhecimentos sólidos sobre bases outrora trabalhadas por minha Professora Orientadora precedente, a Prof.<sup>a</sup> Dr.<sup>a</sup> Cynthia Cristina Martins Junqueira.

A Prof.<sup>a</sup> Dr.<sup>a</sup> Adriane Marie Salm Coelho auxiliou-me pacientemente, com sugestões sobre o uso da língua inglesa, a lapidar a apresentação da obra.

Por fim, eu gostaria de deixar meus sinceros agradecimentos àqueles que, de uma forma desinteressada, acreditaram que um trabalho contributivo estava em curso, e com ele colaboraram.





*“Qual é o grande dragão ao qual o espírito não mais chama de senhor e deus? ‘Tu deves’ chama-se o grande dragão. Mas o espírito do leão diz ‘eu quero’.*

*Assim Falou Zaratustra.”*

(Nietzsche, 1883).



## RESUMO

O início do século XXI apresenta o radar como um utensílio indispensável, com aplicações não mais restritas àquelas outrora exclusivas da Aviação e da Marinha, permeando a vida do homem contemporâneo e variando em diferentes complexidades. Nesse cenário, a capacidade de detectar radares proporciona inúmeras vantagens, tanto no contexto civil quanto no militar. O mundo moderno, entretanto, não raramente impõe restrições de volume, peso e custos à Eletrônica, o que se opõe ao processamento complexo demandado por detectores de radar para desembaralhar o sinal resultante da superposição de sinais recebidos de diversos emissores. Esta pesquisa propõe técnicas de processamento de sinais que consideram peculiaridades de radiofrequência a fim de amenizar a carga de trabalho do processador, e, assim, possibilitar detectores com baixo volume, peso, custos e poder computacional disponível. Experimentos foram realizados com um protótipo de um Sistema de Medidas de Apoio à Guerra Eletrônica (MAGE) com processamento em *tablet*, baseado em Rádio Definido por Software (RDS). Resultados mostram que o desempenho da técnica proposta de medição de pulsos se degradou significativamente apenas quando as amplitudes dos pulsos foram  $\leq 3.7$  mV na entrada do RDS empregado. Eles também mostram que o método sugerido de medição de direção de chegada exibiu distribuições gaussianas para as medições, com desvio padrão tão maior quanto menor a amplitude dos pulsos recebidos, o que permite, através do segundo, efetuar inferências sobre o primeiro. Beneficiando-se disso, o algoritmo de agrupamento de pulsos desenvolvido definiu, diante de 6 distribuições, agrupamentos com taxas de enclausuramento  $\geq 92.71$  %. Por fim, resultados também demonstraram que o algoritmo de reconhecimento de padrões, ao receber padrões de 4 radares simulados, com diferentes tipos de varredura de antena, desembaralhou os 4 padrões, com taxas de atribuição apropriada do intervalo de repetição de pulsos  $\geq 96.30$  %, além de estimar o intervalo de repetição de pulsos com erros da ordem de  $10^{-5}$ . Este estudo é indicado para as áreas de Processamento de Sinais de Radar, Medição de Direção de Chegada, Reconhecimento de Padrões e Guerra Eletrônica.

**Palavras-chave:** Detector de radar. Guerra Eletrônica. Sistema MAGE. RDS. Medição de pulsos. Medição da direção de chegada. Agrupamento de pulsos. Desembaralhar por intervalos.



## RESUMO EXPANDIDO

### Introdução

O século XX proporcionou à humanidade uma forma inovadora de sensoriamento eletrônico chamada *radar*, oriunda de interações entre a tecnologia e a filosofia militar. Inicialmente, esses dispositivos eram aplicados exclusivamente para defesa aérea, a partir de plataformas terrestres, marítimas e aéreas. Eles provaram-se efetivos em vigilância de longo alcance, em detecção de alvos próximos e à baixa altura, no controle de armas e no guiamento de mísseis. Posteriormente, proporcionaram segurança ao controle de tráfego aéreo, separando aeronaves entre si, bem como disponibilizando informações meteorológicas e leituras precisas de altitude às tripulações. Aplicações marítimas são análogas às da Aviação, e o uso do radar permite medidas de distância entre embarcações, detecções de ilhas e faróis, a coordenação de tráfego próximo a portos, além do guiamento de mísseis contra embarcações inimigas. O início do século XXI apresenta o radar como um utensílio indispensável, e suas aplicações são cada vez mais comuns, variando em diferentes complexidades, do monitoramento de ventos e precipitações por meteorologistas e o mapeamento da crosta terrestre por geólogos, até o monitoramento da velocidade de veículos nas rodovias e a abertura de portas automáticas nos centros comerciais. Em um cenário como esse, a capacidade de localizar e identificar radares proporciona inúmeras vantagens, tanto no contexto civil quanto no militar. O mundo moderno, contudo, não raramente impõe restrições de volume, peso e custos aos equipamentos eletrônicos. Em contraposição a isso, para discriminar sinais de radares, detectores devem efetuar um processamento complexo para desembaralhar o sinal resultante da superposição de sinais recebidos de diversos emissores, que podem estar posicionados, cada um, a uma diferente direção e distância.

### Objetivos

O objetivo da presente pesquisa é propor técnicas de processamento de sinais que considerem peculiaridades da área de radiofrequência para amenizar a carga de trabalho demandada ao processador, e, assim, possibilitar o desenvolvimento de detectores com baixo volume, peso, custos e poder computacional disponível.

## Metodologia

Para atingir o objetivo proposto, primeiramente, um cenário simples de Guerra Eletrônica é descrito, e, a partir dele, a complexidade envolvida no funcionamento de um detector de radar genérico é derivada. Uma arquitetura abrangente de detector, porém já com vistas à economia de recursos computacionais, é proposta, e peculiaridades relacionadas a radiofrequência são apontadas. Em seguida, os diversos estágios de processamento, como a detecção de pulsos, a medição da direção de chegada, o agrupamento de pulsos segundo essa medição e a necessidade de desembaralhar padrões em cada um dos agrupamentos, são desenvolvidos. A técnica de medição de pulsos apresentada é baseada nas variações da envoltória do sinal resultante da superposição de sinais recebidos de diversos emissores. Ela pode detectar pulsos que estão sobrepostos no domínio do tempo, o que diminui a taxa de pulsos perdidos dentro de um determinado padrão, evitando assim complicações no reconhecimento do mesmo, no último estágio de processamento. O método proposto para a medição da direção de chegada visa permitir a medição deste parâmetro, sem ambiguidades, em regiões angulares nas quais as antenas do arranjo apresentam lóbulos secundários. Dessa forma, o setor angular de interesse pode ser dividido por um número menor de canais do que aquele possibilitado por técnicas analíticas convencionais, que operam apenas na região do lóbulo principal das antenas. Isso possibilita a economia de recursos computacionais pelo fato de os pulsos recebidos serem processados, no estágio de medição de pulsos, em menos canais, além da economia de custo, volume e peso associados aos canais. O algoritmo de agrupamento de pulsos se beneficia da confiabilidade da medição da direção de chegada para criar agrupamentos de pulsos que serão entregues ao último estágio, de reconhecimento de padrões. As características das distribuições das medições de direção de chegada, associadas ao conhecimento do sistema e da amplitude dos pulsos, permitem inferências sobre como cada agrupamento deve ser formado, o que proporciona acurácia e economia de recursos computacionais para o método. Por último, um algoritmo baseado apenas nos intervalos entre pulsos sequenciais desembaralha padrões presentes em cada um dos agrupamentos que foram formados com base na direção de chegada. Para esse estágio final, foram aplicadas mudanças sobre o método clássico e consagrado de Mardia. Elas possibilitaram a supressão do estágio de busca sequencial e a determinação das faixas de períodos adequadas para análise de padrões dentro de cada agrupamento, além de

uma estimativa precisa do intervalo de repetição de pulsos. Para validação das técnicas propostas, experimentos foram implementados com um protótipo de um Sistema de Medidas de Apoio à Guerra Eletrônica (MAGE) baseado em Rádio Definido por Software (RDS) e com processamento em dispositivo do tipo *tablet*.

## **Resultados e Discussão**

O desempenho da técnica de medição de pulsos degradou-se significativamente apenas quando as amplitudes dos pulsos foram menores ou iguais a 3.7 mV na entrada do RDS empregado. Tais resultados sugerem que o algoritmo evita que, acima desse limiar, pulsos sejam perdidos, mesmo quando os mesmos estão sobrepostos no domínio do tempo, o que evita complicações no reconhecimento de padrões, no último estágio de processamento. O método de medição de direção de chegada apresentou distribuições com características gaussianas para as medições. As distribuições apresentam desvio padrão tão maior quanto menor a amplitude dos pulsos, o que permite, através do segundo, efetuar inferências sobre o primeiro. Essas características das distribuições sugeriram que o agrupamento dos pulsos baseado na direção de chegada, realizado no próximo estágio de processamento, pudesse ser efetuado com uma estimativa de densidade kernel baseada na função gaussiana, ou a partir de uma filtragem dos histogramas das medições por filtros gaussianos. O algoritmo de agrupamento de pulsos formou, em um cenário com 6 distribuições de medições de direção de chegada, agrupamentos de pulsos com taxas de enclausuramento maiores ou iguais a 92.71 % quando o fator de ajuste do tamanho dos agrupamentos foi configurado para 2. Essas taxas, aliadas ao desempenho da técnica de medição de pulsos, garantem que os padrões de intervalos de repetição de pulsos sejam entregues ao último estágio, responsável por reconhecê-los, com poucas corrupções. Por fim, o algoritmo de reconhecimento dos padrões de intervalo de repetição de pulsos, ao receber um agrupamento de pulsos contendo padrões de 4 radares simulados que apresentavam diferentes tipos de varredura de antena, desembaralhou os 4 padrões e apresentou taxas de atribuição apropriada do intervalo de repetição de pulsos maiores ou iguais a 96.30 %. Além disso, a técnica proposta para estimativa do intervalo de repetição de pulsos apresentou erros da ordem de  $10^{-5}$ . Esses resultados mostram que a supressão da busca sequencial contida no método de Mardia, que salvou recursos computacionais, não causou prejuízos no desempenho do algoritmo.

## **Considerações Finais**

Os métodos introduzidos nesta pesquisa permitem que sinais de radares sejam totalmente processados e desembaralhados uns dos outros. Cada passo dos algoritmos, assim como o todo, foi desenvolvido para demandar poucos recursos computacionais, o que, associado aos poucos canais de recepção necessários, resultam em baixo peso, volume e custos para o detector de radar, de forma a cumprir o objetivo do trabalho. A comparação dos parâmetros medidos desses sinais com um banco de dados pré-cadastrados pode fornecer, finalmente, a identificação dos radares. Este estudo é recomendado para as áreas de Processamento de Sinais de Radar, Medição de Direção de Chegada, Reconhecimento de Padrões e Guerra Eletrônica.

**Palavras-chave:** Detector de radar. Guerra Eletrônica. Sistema MAGE. RDS. Medição de pulsos. Medição da direção de chegada. Agrupamento de pulsos. Desembaralhar por intervalos.



## ABSTRACT

The beginning of the 21st century presents the radar as an indispensable utility, with applications no longer restricted only to those formerly exclusive of Aviation and Navy, permeating the life of the contemporary man and varying in different complexities. In this scenario, the ability to detect radars provides numerous advantages, both in the civilian and military contexts. The modern world, however, often imposes volume, weight, and costs constraints on Electronics, which opposes the complex processing demanded by radar detectors to deinterleave the signal that resulted from the superposition of signals received from many emitters. This research proposes signal processing techniques that look at radiofrequency peculiarities in order to soften the processing workload and to allow the design of radar detectors that present low volume, weight, costs and available computational power. Experiments were carried out with a prototype of an Electronic Support Measures (ESM) system with tablet processing, based on Software-Defined Radio (SDR). Results show that the performance of the proposed pulse measurement technique degrades significantly only when the pulse amplitudes are  $\leq 3.7$  mV at the input of the used SDR. They also show that the suggested direction-finding method presents Gaussian distributions for the measurements, with a standard deviation as high as the lower the amplitude of incoming pulses, which allows, according to the latter, to make inferences about the former. Benefiting from this, the developed pulse-clustering algorithm defined, in front of 6 distributions, clusters of pulses with enclosure rates  $\geq 92.71$  %. Finally, the results show that the proposed pattern recognition algorithm, when it received a cluster of pulses with patterns of 4 simulated radars, with different types of antenna scan, deinterleaved the 4 patterns, with rates of correct assignment of the pulse repetition interval  $\geq 96.30\%$ , besides estimating the pulse repetition interval with errors of the order of  $10^{-5}$ . This study is recommended for the areas of Radar Signal Processing, Direction Finding, Pattern Recognition and Electronic Warfare.

**Keywords:** Radar detector. Electronic Warfare. ESM system. SDR. Pulse measurement. Direction finding. Pulse clustering. Interval-only deinterleaving.



## LIST OF FIGURES

Fig. 1.1 – Radar detector network to control air traffic.....	34
Fig. 1.2 – An ELINT system embedded on a tablet. ....	35
Fig. 1.3 – A simple EW scenario faced by a radar detector. ....	36
Fig. 1.4 – Type of the resulting signals on the detector’s receivers. ....	36
Fig. 1.5 – Example of amplitude-based DF method.....	37
Fig. 1.6 – Redrawing of Fig. 1.3 in more detail. ....	38
Fig. 1.7 – Radar detector schematic to handle the context of Fig. 1.6. ....	39
Fig. 1.8 – Simplified block diagram of classical radar receivers. ....	41
Fig. 1.9 – Adequate pattern for amplitude-based analytical methods. ..	42
Fig. 1.10 – Expansion of the processing box of Fig. 1.7.....	43
Fig. 2.1 – Interleaved signals received by a radar detector. ....	51
Fig. 2.2 – The sampling of the leading edge of a generic pulse. ....	53
Fig. 2.3 – Superimposed signals.....	55
Fig. 2.4 – Combination of P5 and P6 at antenna terminations. ....	56
Fig. 2.5 – Output of a logarithmic receiver with P5 and P6. ....	57
Fig. 2.6 – Nonlinearity correction of signals of Fig. 2.5. ....	58
Fig. 2.7 – P7 measurements at 10 ns sample time.....	59
Fig. 2.8 – Moving average of P7 sample value variations .....	60
Fig. 2.9 – Variation-based pulse detection algorithm flowchart. ....	61
Fig. 2.10 – SDR-based ESM system prototype. ....	63
Fig. 2.11 – A couple of received superimposed pulses .....	65
Fig. 3.1 – Conventional amplitude-based DF methods. ....	70
Fig. 3.2 – Example of pattern as a function of $\lambda$ . ....	71
Fig. 3.3 – Amplitude-based DF technique at 4 GHz with 8 spirals.....	73
Fig. 3.4 – Amplitude-based DF technique at 16 GHz with 4 spirals.....	74
Fig. 3.5 – Amplitude-based DF technique at 10 GHz with 4 spirals.....	76
Fig. 3.6 – DOA measurements in the absence of noise.....	79
Fig. 3.7 – DOA measurement simulation at high SNR. ....	80
Fig. 3.8 – DOA measurement simulation at low SNR. ....	80
Fig. 3.9 – Definitive disposition of the antennae.....	81
Fig. 3.10 – Estimated prototype normalized patterns at 1.5 GHz. ....	82
Fig. 3.11 – Results from DOA measurements.....	83
Fig. 3.12 – Results with signals 12 dB below. ....	83
Fig. 4.1 – The clustering of pulses according to their DOA.....	87
Fig. 4.2 – Histogram of DOA ( $\Phi_{rx} = 126^\circ$ ). ....	90
Fig. 4.3 – Filtering of histogram of Fig. 4.2. ....	91
Fig. 4.4 – Histogram of DOA ( $\Phi_{rx} = 250^\circ$ ). ....	92
Fig. 4.5 – Plot of the $DOA_i \times p\sigma$ plane.....	93

Fig. 4.6 – Gaussian-filtered distribution. ....	94
Fig. 4.7 – DOA histogram of signals of Table 4.1. ....	98
Fig. 4.8 – Complex scenario on the $DOA_i \times p\sigma$ plane. ....	98
Fig. 4.9 – Scaled moving average of scenario of Fig. 4.8. ....	99
Fig. 4.10 – Gaussian-filtered distribution. ....	99
Fig. 5.1 – Pulse sequence of signal whose PRI = 100 samples. ....	104
Fig. 5.2 – Histogram of first differences of TOAs of Fig. 5.1. ....	105
Fig. 5.3 – Pulse sequence of two radar signals. ....	105
Fig. 5.4 – Histogram of first differences of TOAs of Fig. 5.3. ....	106
Fig. 5.5 – CDIF evaluated until the second difference order. ....	106
Fig. 5.6 – CDIF evaluated until the third difference order. ....	107
Fig. 5.7 – Proposed algorithm flowchart. ....	112
Fig. 5.8 – Timeline of R1-R4 signals inside cluster. ....	114
Fig. 5.9 – CDIF evaluated until the tenth difference order. ....	114
Fig. 5.10 – Estimate of the time-density of pulses. ....	115
Fig. 5.11 – Variations related to the pulse time-density estimate. ....	116
Fig. 5.12 – CDIF of subcluster SC1, until the second order. ....	117
Fig. 5.13 – CDIF of subcluster SC2, until the second order. ....	118
Fig. 5.14 – CDIF of subcluster SC4, until the third order. ....	118

## **LIST OF FRAMES**

Frame 1.1 – Features of the state-of-the art and of this work.....	46
Frame 3.1 – Summary of the presented DF technique. ....	78
Frame 4.1 – Summary of the presented pulse clustering technique. ....	96



## LIST OF TABLES

Table 2.1 – Hypothetical pulses. ....	54
Table 2.2 – Pulses emitted by USRP B200. ....	64
Table 2.3 – Results of P8 alone. ....	66
Table 2.4 – Results in front of P8 and P9 superimposed pulses. ....	66
Table 2.5 – Results in front of P10 and P11 superimposed pulses. ....	66
Table 4.1 – Pulsed signals joined in the $DOA_i \times p\sigma$ plane. ....	97
Table 4.2 – Results with CSAF = 1. ....	100
Table 4.3 – Results with CSAF = 2. ....	101
Table 5.1 – Pulsed signals in the same DOA-based cluster. ....	113
Table 5.2 – Detected time-density-based subclusters. ....	116
Table 5.3 – Results of the interval-only technique. ....	119





## LIST OF ACRONYMS

A/D – analog-to-digital;  
AWGN – additive white Gaussian noise;  
CDIF – cumulative histogram of differences of sequential TOAs;  
CSAF – cluster size adjusting factor;  
DF – direction finding;  
DOA – direction of arrival;  
ELINT – Electronics Intelligence;  
ESM – Electronic Support Measures;  
EW – Electronic Warfare;  
FC – frequency of carrier;  
FPGA – field programable gate array;  
IF – intermediate frequency;  
IoT – Internet of Things;  
IP – instantaneous power;  
LNA – low-noise amplifier;  
PA – pulse amplitude;  
POI – probability of interception;  
PRI – pulse repetition interval;  
PW – pulse width;  
RF – radiofrequency;  
RWR – Radar Warning Receiver;  
SDR – Software-Defined Radio;  
SNR – signal-to-noise ratio;  
TOA – time of arrival; and  
VCO – voltage-controlled oscillator.



## LIST OF SYMBOLS

- $A$  – array representing distribution of pulses in the  $DOA_i \times p_\sigma$  plane;  
 $a_{ij}$  – elements of  $A$ ;  
 $BW_{rx}$  – bandwidth on receiving;  
 $C$  – set which contains the subsets  $C_k$  measured at FCs of interest;  
 $C_k$  – subsets of  $C$ , containing vectors  $\vec{v}_i$  concerning a specific FC;  
 $CDIF(diff)$  – occurrences on the  $diff$  bin of CDIF histogram;  
 $CDIF'(diff'_k)$  – CDIF histogram after moving averaged procedure;  
 $CDIF_j(diff)$  – occurrences on the  $diff$  bin of CDIF of subcluster  $j$ ;  
 $d(\vec{p}, \vec{v}_i)$  – Euclidean distance between  $\vec{p}$  and  $\vec{v}_i$ ;  
 $d'(\vec{p}, \vec{v}_i)$  – weighted Euclidean distance between  $\vec{p}$  and  $\vec{v}_i$ ;  
 $diff$  – CDIF histogram bin relative to specific difference of TOAs;  
 $diff'_k$  – bin of the moving averaged  $CDIF'$  histogram;  
 $DF(\Phi_{rx})$  – azimuthal direction-finding function;  
 $DF_i$  – inverse function of  $DF(\Phi_{rx})$  function;  
 $DOA_i$  – discrete domain of DOA measurements;  
 $doa_s$  – sample of DOA measurement in the discrete domain;  
 $E(x)$  – envelope function;  
 $E'(PRI)$  – expectation of PRI;  
 $\mathcal{F}$  – array generated from the filtering of  $MA$ ;  
 $\vec{f}$  – vector containing the maximum values of each row of  $\mathcal{F}$ ;  
 $F(t)$  – output of receiver;  
 $F_i$  – the inverse function of  $F(t)$ ;  
 $f_s$  – sampling rate, in samples per second;  
 $g$  – Gaussian filter;  
 $\Phi$  – azimuthal angle;  
 $\Phi_{left}$  – azimuthal angle to where the left antenna main lobe is directed;  
 $\Phi_{right}$  – azimuthal angle to where the right antenna main lobe points;  
 $\Phi_{rx}$  – azimuthal angle referred to the receiver coordinate system;  
 $\Phi_{tx}$  – azimuthal angle referred to the transmitter coordinate system;  
 $G$  – gain factor in ideal logarithmic receiver;  
 $G_{rx}$  – gain function of the radar detector antenna;  
 $G_{tx}$  – gain function of the radar antenna;  
 $h$  – Gaussian scaling factor;  
 $hist$  – histogram of the measured  $doa_s$  samples;  
 $h_j$  – Gaussian scaling factor dimensioned according to column  $j$ ;  
 $K$  – constant of Boltzmann;  
 $L_p$  – losses on all stages of propagation, whether or not guided;

$m_\phi$  – number of measurements along angular sector of interest;  
 $MA$  – array generated from the scaled moving average procedure of  $A$ ;  
 $ma_{ij}$  – elements of  $MA$ ;  
 $\mu$  – mean of Gaussian function;  
 $n_{ch}$  – number of channels, in units;  
 $n_h$  – number of Gaussian scales used in the filtering procedure;  
 $n_i$  – number of intervals between samples;  
 $n_m$  – number of measurements;  
 $n_s$  – number of  $doa_s$  samples, in units;  
 $n_{tx}$  – number of radars, in units;  
 $N$  – size of the data frame, in data samples;  
 $N_j$  – size of the data frame of subcluster  $j$ , in data samples;  
 $NF$  – noise figure;  
 $\vec{p}$  – vector of normalized PAs in each channel of incoming pulse;  
 $PA_{left}$  – PA of pulse found on the left receiver used on DF technique;  
 $PA_{right}$  – PA of pulse found on the right receiver used on DF technique;  
 $P_d$  – probability of detection of pulses;  
 $P_f$  – probability of false alarm of pulses;  
 $P_l$  – probability of the event  $\tau_{n_i}$ , relative to a leading edge;  
 $p_\sigma$  – predicted standard deviation  $\sigma$  of distribution;  
 $P_t$  – probability of the event  $\tau_{n_i}$ , relative to a trailing edge;  
 $P_{rx}$  – peak power of pulse on the radar detector receiver;  
 $P_{tx}$  – peak power of pulse on the radar transmitter;  
 $q_{FC}$  – number of subsets  $C_k$ , measured at different FCs of interest;  
 $\rho_p$  – pulse density, in pulses per second;  
 $R$  – distance between radar and radar detector;  
 $R_{max}$  – range of the radar detector to detect a specific pulse;  
 $S_{min}$  – sensitivity of the system;  
 $SNR_i$  – minimum SNR on the receiver input to achieve a specific  $P_d$ ;  
 $SNR_o$  – minimum SNR on the receiver output to achieve a specific  $P_d$ ;  
 $\sigma$  – standard deviation of Gaussian function;  
 $T_a$  – physical temperature of the antenna;  
 $T_e$  – time relative to leading or trailing edge;  
 $T_f$  – time relative to one frame of data;  
 $T_r$  – radiation temperature of the antenna;  
 $T_s$  – time relative to one sample;  
 $\theta$  – elevation angle;  
 $\theta_{rx}$  – elevation angle referred to the receiver coordinate system;  
 $\theta_{tx}$  – elevation angle referred to the transmitter coordinate system;

$\tau_{n_i}$  – event in which an edge lies on  $n_i$  intervals between samples;  
 $v(t)$  – input of an ideal logarithmic receiver;  
 $\vec{v}_i$  – vector of normalized PAs in each channel in a specific  $\Phi_{rx}$  and FC;  
 $v_j$  – elements of  $\vec{v}_i$ ;  
 $\lambda$  – wavelength;  
 $w_{MA}$  – moving average window;  
 $WF$  – threshold weighting factor;  
 $WT(diff)$  – weighted threshold of *diff* bin of CDIF histogram;  
 $WT_j(diff)$  – weighted threshold of *diff* bin of CDIF of subcluster  $j$ ;  
and  
 $Z_0$  – reference impedance.



## SUMMARY

<b>1</b>	<b>INTRODUCTION.....</b>	<b>33</b>
1.1	THE CONTEXT .....	33
1.2	RESEARCH QUESTIONS.....	35
1.3	THE PROBLEM.....	35
1.4	OBJECTIVES .....	43
<b>1.4.1</b>	<b>General objective.....</b>	<b>43</b>
<b>1.4.2</b>	<b>Specific objectives .....</b>	<b>43</b>
1.5	THIS WORK AND THE STATE-OF-THE-ART .....	44
1.6	RELATED PUBLISHED WORKS .....	47
1.7	OUTLINE OF THE DISSERTATION .....	49
<b>2</b>	<b>PULSE MEASUREMENT .....</b>	<b>51</b>
2.1	PRELIMINARIES .....	52
2.2	CASE STUDIES .....	54
<b>2.2.1</b>	<b>Superimposed pulses on a generic receiver.....</b>	<b>54</b>
<b>2.2.2</b>	<b>Nonlinearity correction and low SNR case .....</b>	<b>56</b>
<b>2.2.3</b>	<b>Sampling .....</b>	<b>58</b>
2.3	PROPOSED ALGORITHM .....	61
2.4	EXPERIMENTAL SETUP .....	62
2.5	RESULTS AND DISCUSSION .....	64
2.6	FINAL REMARKS OF THE CHAPTER.....	67
<b>3</b>	<b>DOA MEASUREMENT .....</b>	<b>69</b>
3.1	PRELIMINARIES .....	70
3.2	CASE STUDIES .....	72
<b>3.2.1</b>	<b>Operation in the main lobe zone .....</b>	<b>72</b>
<b>3.2.2</b>	<b>Sidelobe ambiguity .....</b>	<b>73</b>
<b>3.2.3</b>	<b>Frequency of carrier dependence .....</b>	<b>75</b>
3.3	PROPOSED ALGORITHM .....	77

3.4	SIMULATIONS .....	79
3.5	EXPERIMENTAL SETUP.....	81
3.6	RESULTS AND DISCUSSION.....	82
3.7	FINAL REMARKS OF THE CHAPTER .....	84
<b>4</b>	<b>PULSE CLUSTERING .....</b>	<b>87</b>
4.1	PRELIMINARIES.....	88
4.2	CASE STUDIES.....	90
<b>4.2.1</b>	<b>Close to ideal Gaussian case.....</b>	<b>90</b>
<b>4.2.2</b>	<b>Not close to ideal Gaussian case.....</b>	<b>91</b>
4.3	PROPOSED ALGORITHM.....	95
4.4	EXPERIMENTAL SETUP.....	97
4.5	RESULTS AND DISCUSSION.....	99
4.6	FINAL REMARKS OF THE CHAPTER .....	102
<b>5</b>	<b>DEINTERLEAVING INSIDE DOA CLUSTERS .....</b>	<b>103</b>
5.1	CLASSICAL APPROACH .....	104
5.2	PROPOSED CHANGES .....	108
<b>5.2.1</b>	<b>Suppression of the sequence search procedure .....</b>	<b>108</b>
<b>5.2.2</b>	<b>Precise PRI estimation.....</b>	<b>109</b>
<b>5.2.3</b>	<b>Definition of the size of the frame to be processed.....</b>	<b>110</b>
<b>5.2.4</b>	<b>Extra threshold condition .....</b>	<b>111</b>
5.3	VALIDATION.....	113
5.4	FINAL REMARKS OF THE CHAPTER .....	119
<b>6</b>	<b>CONCLUSIONS .....</b>	<b>121</b>
	<b>REFERENCES.....</b>	<b>125</b>



# 1 INTRODUCTION

## 1.1 THE CONTEXT

In the 20th century, interactions between technology and military philosophy provided the world with the advent of an innovative way of electronic sensing called *radar*.

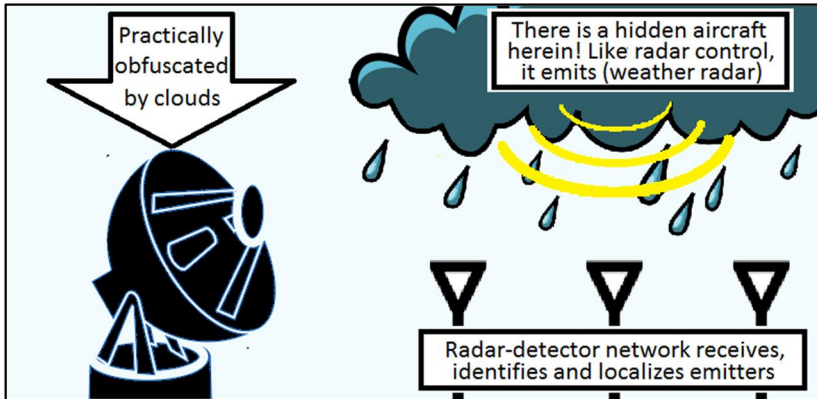
Initially, the chief application of such devices was for air defense from land, sea and/or air. In this scenario, radars have proved effective in long-range air surveillance, short-range detection of low-altitude targets, weapon control, missile guidance and noncooperative target recognition. In an offensive way, fighter aircraft have used air-to-air radar to target enemies and launch their radar-guided missiles against them. Furthermore, specialized military aircraft could carry more sophisticated airborne radars to surveil large areas of the theatre of operations and send bombers against threats. In Civil Aviation, radars have provided safety on the air traffic control, they have allowed the separation of aircraft between each other, as well as they have displayed weather information and accurate altitude readings to crews. Maritime applications are analogue to those of Aviation in both civilian and military contexts, with the use of radars to measure bearing and distance between ships, to detect islands and lightships, to coordinate traffic in waters that are close to ports and to guide missiles against war vessels [1].

The beginning of the 21st century features radars as an indispensable utility, and their applications are becoming increasingly common, varying in different complexities, from the monitoring of wind and precipitation by meteorologists and the mapping of Earth's crust by geologists to the monitoring of vehicle speeds on the roads and the opening of automatic doors in shopping centers, among many others.

In a world populated by so many radars, the capability to locate and identify them provides lots of advantages, in both civilian and military contexts.

One of the civilian applications of radar detectors regards weather disruptions on air traffic radar controls. The processing of the pulsed weather radar signals of aircraft themselves, even those weak due to reflections in heavy clouds, can provide the location and the identification of emitters, if a synchronized network of receivers is set up. Fig. 1.1 illustrates this application.

Fig. 1.1 – Radar detector network to control air traffic.

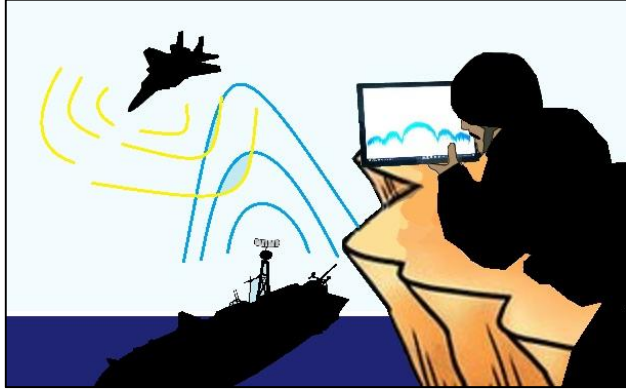


Source: own elaboration.

In Defense, radar detectors can work mainly as complete Electronics Intelligence (ELINT) or Electronic Support Measures (ESM) systems if their receivers are wideband and pattern recognition methods are used. These systems are designed to intercept, locate, classify and identify radiofrequency (RF) emitters through the passive monitoring of the electromagnetic environment. In front of the most advanced modern radars, they are considered successful when they "detect while stay undetected". To do that, they must be able to receive and process the weakest signals transmitted by the furthest emitters [2]. Radar Warning Receivers (RWR), which warn crews about threatening radars, present the same range constraints, but missile guidance systems usually do not. In their case, the maximum range is commonly determined by the propulsion system.

It is worth mentioning at this point that the modern world often requires features of low volume, weight and costs to its electronic equipment. For instance, a radar detector embedded in an anti-radiation missile head cannot exceed a certain size, and the RWR of a nation that resists in an asymmetric war cannot be expensive or hard to build. These factors result in the need of radar detectors that require low computational power, in parallel to the constraints of volume, weight and costs. Fig. 1.2 exemplifies an ELINT system embedded on a tablet device, which would present features of low volume, weight and costs, besides furtiveness, accessibility to where trucks do not go and communication with other devices using conventional networks.

Fig. 1.2 – An ELINT system embedded on a tablet.



Source: own elaboration.

## 1.2 RESEARCH QUESTIONS

In front of the context described on Section 1.1, the following research questions are unavoidable:

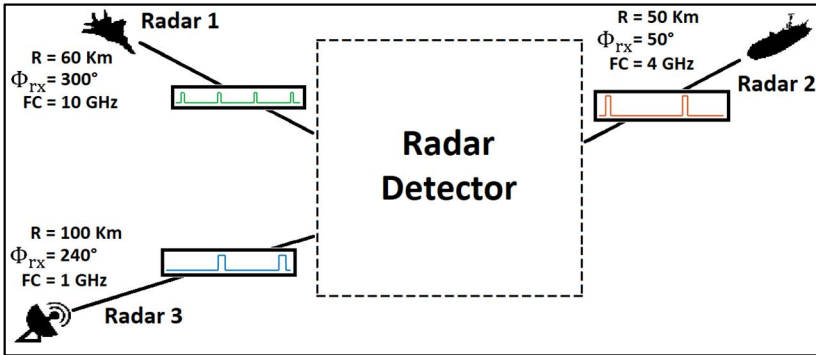
- a) “How to design equipment such as radar detectors having restricted resources?”
- b) “Is it possible to design them with low volume, weight, costs and processing capabilities?”

## 1.3 THE PROBLEM

Despite the need of low computational power required by the modern world, the complexity demanded by radar detectors to process radar signals makes their design very challenging. Before locating and identifying surrounding radars, detectors must deinterleave the signals thereof.

Fig. 1.3 exemplifies a simple Electronic Warfare (EW) scenario, in which a radar detector must deal with the signals of  $n_{tx} = 3$  radars that are embedded on 3 different platforms. On the illustrated case, each radar emits a pulsed signal with a specific pulse width (PW) and pulse repetition interval (PRI) pattern, at a specific frequency of carrier (FC).

Fig. 1.3 – A simple EW scenario faced by a radar detector.

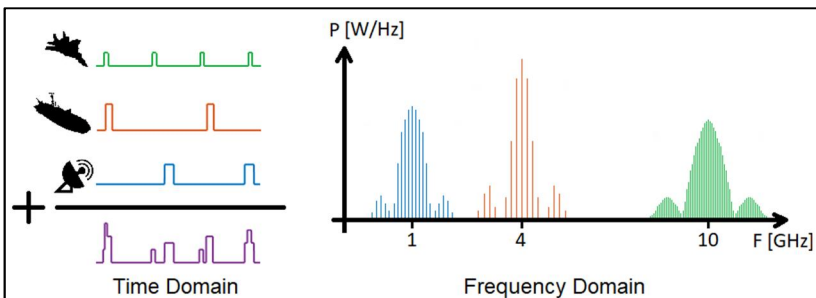


Source: own elaboration.

Regarding the envelopes and the FCs of the signals of Fig. 1.3, the resulting signal on the receivers of the radar detector is similar to the one illustrated on Fig. 1.4, in both time and frequency domains. Some pulses of different radars can be superimposed in the time domain.

Each illustrated radar operates at a specific FC and presents an antenna with gain  $G_{tx}(\theta_{tx}, \Phi_{tx})$ , considered function only of its elevation  $\theta_{tx}$  and azimuthal  $\Phi_{tx}$  angles. The radar detector, however, faces emitters whose FCs are unknown to it. Its antennae do not have necessarily similar radiation patterns in front of each radar signal. Therefore, the gain of the receiving antennae  $G_{rx}(\theta_{rx}, \Phi_{rx}, \lambda)$  is also a function of the wavelength  $\lambda$  on this work. On Fig. 1.4, discriminating signals by their PW or FC is enough to deinterleave them. However, modern radars may present agility on these parameters, thereby making approaches based solely on them unreliable [1, 2].

Fig. 1.4 – Type of the resulting signals on the detector's receivers.

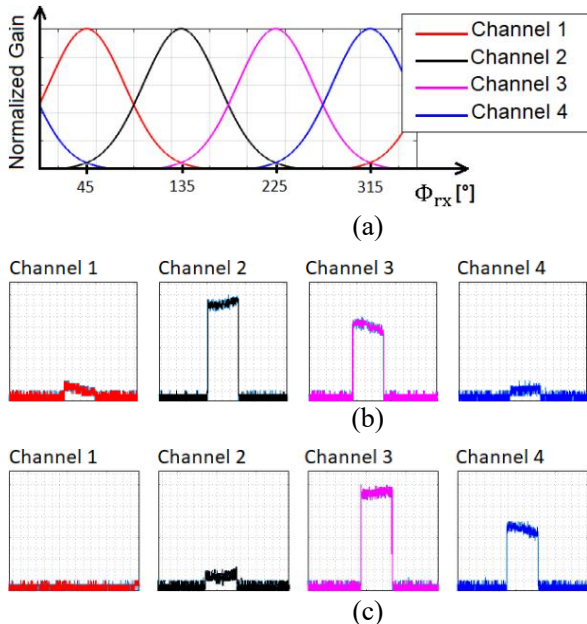


Source: own elaboration.

On Fig. 1.3, an azimuthal angle  $\Phi_{rx}$  is associated to the position of each radar around the detector. On the example, none platform can move fast enough in a considerable range in front of the PRI time order, which makes the position of emitters a reliable parameter, in which the measurement of the direction of arrival (DOA) is based. Clustering pulses according to their DOA is sufficient to deinterleave them on the case of Fig. 1.3, because the radars are azimuthally far away from each other. To measure DOA without degrading the probability of interception (POI), a multichannel architecture, consisted of  $n_{ch}$  mechanically fixed antennae and synchronized receivers [3], is used. Direction-finding (DF) methods based on the pulse amplitude (PA) require directive antennae. These antennae are designed to present suitable gain functions  $G_{rx}(\theta_{rx}, \Phi_{rx}, \lambda)$  dependent on angles  $\theta_{rx}$  and  $\Phi_{rx}$ , which allows, for a single received pulse, the measuring of different values of PA in the channels. Fig. 1.5 exemplifies a case in which the patterns of  $n_{ch} = 4$  antennae are distributed on the azimuth and two pulses are received with different PAs on the system channels.

Fig. 1.5 – Example of amplitude-based DF method.

(a) Normalized radiation patterns dividing the azimuth, (b) the receiving of a pulse from  $\Phi_{rx} = 170^\circ$ ; and (c) from  $\Phi_{rx} = 255^\circ$ .



Source: own elaboration.

When platforms are azimuthally close to each other, or a unique platform has multiple radars, pulses from various radars lie in the same DOA-based cluster. On these cases, the PRI patterns within these clusters must be distinguished. The missing pulses phenomenon, consisted of the absence of a number of pulses in a pattern, hampers recognition methods of PRI patterns, usually requesting more processing stages to make it succeed [2].

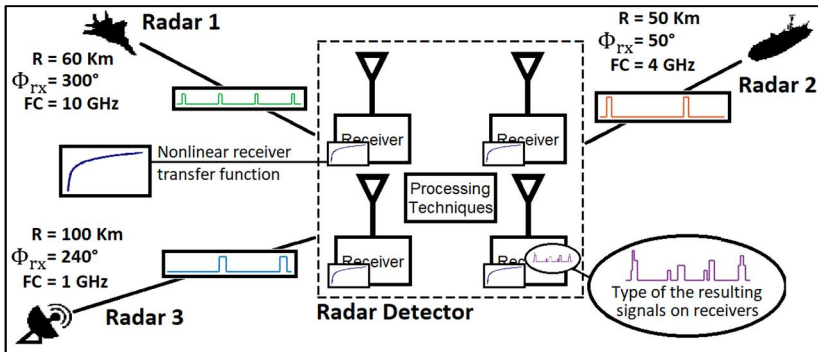
Each radar of Fig. 1.3 may employ a different peak power  $P_{tx}$  to its pulses. Furthermore, they may use specific antenna scan patterns, changing the  $\theta_{tx}$  and  $\Phi_{tx}$  angle values each time in their antenna gain functions  $G_{tx}(\theta_{tx}, \Phi_{tx})$ , which amplitude-modulates pulses. Still, they are located at different distances  $R$  from the radar detector. The received peak power  $P_{rx}$  of a pulse arriving at the input of the receivers of the radar detector is defined by the *one-way radar equation* [2]:

$$P_{rx} = \frac{P_{tx} G_{tx}(\theta_{tx}, \Phi_{tx}) G_{rx}(\theta_{rx}, \Phi_{rx}, \lambda) \lambda^2}{(4\pi R)^2 L_p} \quad (1.1)$$

where  $L_p$  encompasses losses of all stages of propagation, whether or not guided. The trio  $P_{tx}$ ,  $G_{tx}(\theta_{tx}, \Phi_{tx})$  and  $R$  results in a wide range of possible received amplitudes  $P_{rx}$  in (1.1), which requires a wide dynamic range of the detector. This issue is faced on radar detectors with nonlinear receiver transfer functions.

After these initial considerations, the EW scenario of Fig. 1.3 may be redrawn in more detail, as illustrated on Fig. 1.6:

Fig. 1.6 – Redrawing of Fig. 1.3 in more detail.



Source: own elaboration.

The approach of this work is to develop signal processing techniques that look at the mentioned RF peculiarities. The techniques aim to soften the processing workload, thereby allowing the design of radar detectors with low volume, weight, costs and available computational power.

Fig. 1.7 suggests the schematic of a radar detector to handle with the context illustrated on Fig. 1.6. On the proposed schematic, the higher the number  $n_{ch}$  of channels, the greater the accuracy in DF techniques [4], the need of computational power to process the received pulses in each of the  $n_{ch}$  channels, the volume, the weight and the costs.

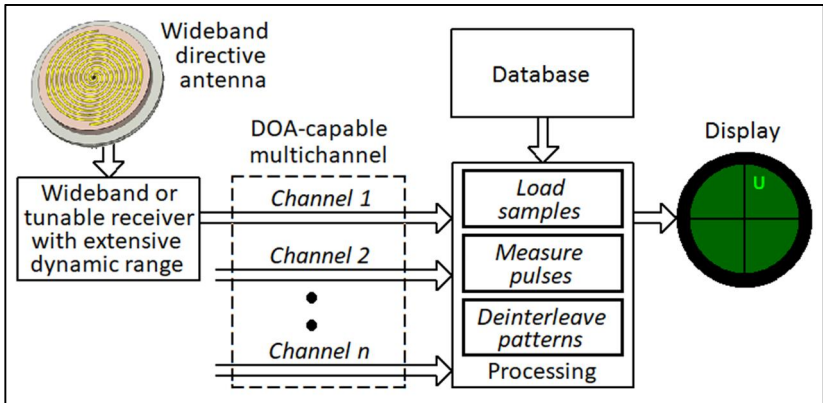
The system performance to detect a specific pulse is found from the development of (1.1), which shows the detector range  $R_{max}$  [2]:

$$R_{max} = \sqrt{\frac{P_{tx} G_{tx}(\theta_{tx}, \Phi_{tx}) G_{rx}(\theta_{rx}, \Phi_{rx}, \lambda) \lambda^2}{(4\pi)^2 S_{min} L_p}} \quad (1.2)$$

where  $S_{min}$  is the sensitivity of the radar detector, evaluated as [5]:

$$\begin{aligned} S_{min} &= SNR_i K (T_a + T_r) BW_{rx} \\ &= SNR_o NF K (T_a + T_r) BW_{rx} \end{aligned} \quad (1.3)$$

Fig. 1.7 – Radar detector schematic to handle the context of Fig. 1.6.



Source: own elaboration.

where  $SNR_o$  is the minimum signal-to-noise ratio (SNR) required by the signal processing algorithm on the output of the receivers to achieve specific rates of probability of detection  $P_d$  and false alarm  $P_f$  of pulses;  $SNR_i$  is the same parameter, but referred to the receiver input;  $NF$  is the noise figure of the receivers;  $BW_{rx}$  is the bandwidth on the receiving;  $K$  is the constant of Boltzmann,  $T_a$  is the antenna physical temperature; and  $T_r$  is the antenna radiation temperature, defined as [6]:

$$T_r = \frac{1}{\Omega_a} \int_0^\pi \int_0^{2\pi} T(\theta_{rx}, \Phi_{rx}) U'(\theta_{rx}, \Phi_{rx}) d\Omega \quad (1.4)$$

where  $T(\theta_{rx}, \Phi_{rx})$  is the thermic radiation distribution function comprised by  $BW_{rx}$ ;  $U'(\theta_{rx}, \Phi_{rx})$  is the normalized radiation intensity function of the antenna; and  $\Omega_a$  is the antenna beam solid angle.

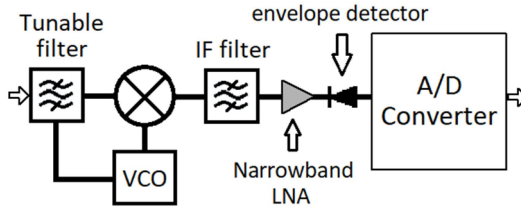
To handle the wide range of FCs exemplified on the context of Fig. 1.4, tunable and wideband receivers are classically employed on radar detectors [7]. Fig. 1.8 illustrates the simplified block diagrams for both a scanning super-heterodyne (tunable) and a crystal video (wideband) types of radar receivers.

Scanning super-heterodyne receivers – Fig. 1.8 (a) – do not cover all the frequency range of interest instantaneously. Therein, a tunable filter sweeps the range of frequency of interest and the admitted signals are beaten with the signal of a voltage-controlled oscillator (VCO), which down-converts them to an intermediate frequency (IF). POI is not near a hundred percent in super-heterodyne receivers, but the narrowband low-noise amplifiers (LNA) of such receivers typically determine, in (1.3), low values of noise figure  $NF$  [7]. On the other hand, POI is a hundred percent in crystal video receivers – Fig. 1.8 (b) – but their wideband LNAs, among other factors, tend to make them present higher values of  $NF$  than super-heterodynes. Furthermore, the receiving bandwidth  $BW_{rx}$  appears in both (1.3) and (1.4). These features result in a sensitivity  $S_{min}$  that is greater on systems based on wideband receivers than on systems based tunable ones, if the other parameters are unchanged [7]. This drawback of the wideband receivers can be minimized if a channelized architecture takes place, which increases weight, volume and costs. Additionally, tunable receivers provide FC information, while wideband ones do not. Both types of receivers are widely employed on radar detectors, and, therefore, the signal processing techniques proposed on this research consider both.

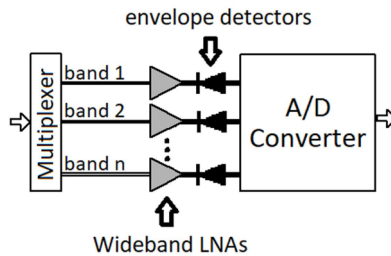


Fig. 1.8 – Simplified block diagram of classical radar receivers.

(a) crystal video and (b) scanning super-heterodyne.



(a)



(b)

Source: own elaboration.

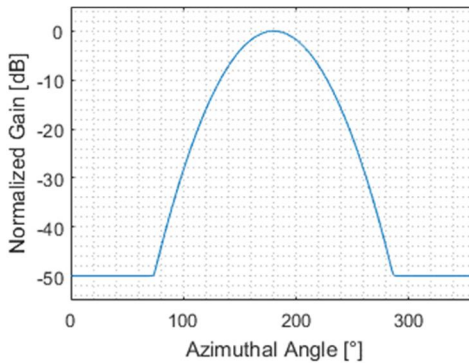
A logarithmic response on receivers increases the dynamic range of the system in relation to the dynamic range of a system with linear response, if the other parameters are unchanged. This enables the processing of a wide range of combinations of the trio  $P_{tx}$ ,  $G_{tx}(\theta_{tx}, \Phi_{tx})$  and  $R$  in (1.1), but it requires a compensation function to recover the linearity of the system on the processing.

On the first stage of the processing, samples of all receivers, which present a sampling rate  $f_s$  of the analog-to-digital (A/D) conversion, are loaded. High values of  $f_s$  define high resolutions of measurements of PW and PRI on the following stages of the processing, but, considering  $n_{ch}$  channels, the processor must load  $n_{ch} f_s$  samples per second. If the measurement of the DOA parameter is based on amplitudes, rather than on phase or time of arrival (TOA), there exist a non-enforceability of high values of  $f_s$ . On measuring PW, TOA and

DOA, the processor workload is proportional to  $n_{ch} \rho_p$ , where  $\rho_p$  is the time-density of the measured pulses. The pulse measurement algorithm states the minimum SNR required by the processing,  $SNR_0$ . The pattern deinterleaving processing workload is proportional mainly to the number  $n_{tx}$  of radars, with less dependence on the density of pulses  $\rho_p$  and none on the number of channels  $n_{ch}$  and the sampling rate  $f_s$ .

In conventional analytical DF methods, to perform well in the context of Fig. 1.6, the antennae must present wideband behaviour so that their radiation patterns vary minimally as a function of the wavelength  $\lambda$  within the range of FC of interest [8]. Conventional PA-based approaches also require the pattern of the antennae to be close to Gaussian functions, with a main lobe basically covering their respective sectors of interest, and the most insignificant possible sidelobes, such as the one illustrated on Fig. 1.9.

Fig. 1.9 – Adequate pattern for amplitude-based analytical methods.

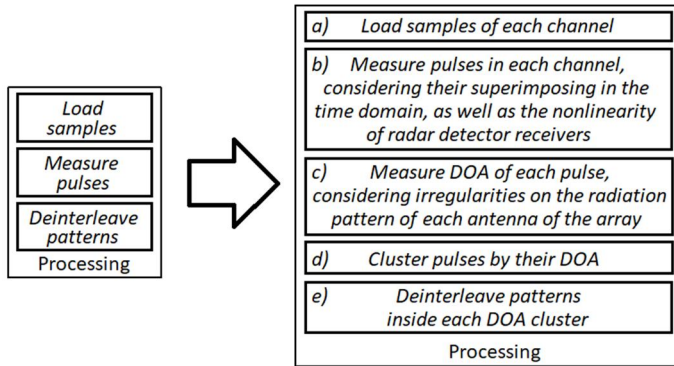


Source: own elaboration.

In practice real wideband antennae may present patterns that vary with  $\lambda$ , besides unforeseen sidelobes. Analytical methods require a high number  $n_{ch}$  of channels to divide the angular sector of interest in a way that each subsector is exclusively covered by main lobes.

Now, the *processing* box of Fig. 1.7 can be expanded to explicit the present work, as shown in Fig. 1.10, considering every peculiarity approached in this section.

Fig. 1.10 – Expansion of the processing box of Fig. 1.7.



Source: own elaboration.

## 1.4 OBJECTIVES

### 1.4.1 General objective

The general objective of this work is: “to propose signal processing techniques that look at RF peculiarities in order to soften the processing workload and to allow the design of radar detectors which present low volume, weight, costs and available computational power”.

### 1.4.2 Specific objectives

To achieve the general objective, the following means are specific objectives:

- a) state an efficient way of measuring pulses, considering the phenomenon of pulse superimposing and the nonlinearity of receivers, solving tasks (a) and (b) of Fig. 1.10;
- b) define a DF method that considers antenna sidelobes and  $\lambda$  dependence, to reliably measure pulse DOAs using as few channels as possible, thus solving task (c) of Fig. 1.10;
- c) determine an efficient way of clustering pulses based on their DOA, thereby solving task (d) of Fig. 1.10; and
- d) determine an efficient way to deinterleave different radar signals contained in each DOA-based pulse cluster, solving task (e) of Fig. 1.10.

## 1.5 THIS WORK AND THE STATE-OF-THE-ART

Recent published papers employ different signal processing approaches to process pulses, deinterleave patterns and classify signals as a means to identify radars. The subject is sensitive and may require confidential data, and, therefore, the literature regarding it is sparse and rare.

To identify patterns of the PRI parameter of interleaved incoming radar signals, Ahmad, Ayeni and Kamal [9] have designed an algorithm that utilizes the Hilbert transform to obtain the analytical version of signals before a Hamming window function is used to smooth their instantaneous power (IP). Following, the first, the second and the third orders of differences of sequential TOAs of received pulses are evaluated and they are used to form rules and to allow the application of a rule-based classifier, which determines the level of PRI agility, but which can handle only pulsed signals with stable and staggered PRI. The entire method is not computationally light.

Gençol, Kara, and At [10, 11] have proposed the use of wavelets to extract features from the signal generated from differences of sequential TOAs of received pulses, to recognize PRI modulation patterns such as stable, jittered, stagger, dwell & switch, sliding and periodic. A multiresolution decomposition of the second difference of sequential TOAs is done by utilizing a discrete Haar wavelet, followed by a support vector machine algorithm that classifies the signals. While the works present capability of handling modern scenarios, the wavelet multilevel decomposition requires the computation of large matrixes.

Kim *et al.* have chosen, rather than the difference of sequential TOAs, the PA parameter in a pattern recognition method based not on the PRI parameter, but on the scanning of the radar antenna. In their work [12], an older approach of correlating the disposition of PAs with a plurality of known scan patterns [13] benefits from the insertion of a new feature analysis, namely, the variance of the difference in the amplitude peak-to-peak intervals. It also benefits from the definition of a new category of scan pattern entitled ‘unidentified’, which allows a decision tree classifier to reduce its false classifications in the categories ‘conical’, ‘circular’, ‘sector’, ‘raster’ and ‘helical’. The identification of the radar antenna scan pattern can easily reveal the associated mission and the level of threatening of the radar, but PA-based methods are sensitive to reflection and scattering phenomena, becoming useful only in air-to-air engagements, since only in this operational condition the communication channel is clean enough.

Despite this constraint, Gençol, Kara, and At have also presented a work based on the PA [14], in which its tracking is faced as a nonlinear least squares estimation problem, and so the scan rate of the radar antennae can be estimated and it can feed a neural network clustering method, alongside DOA, FC and PW parameters.

The approach of Liu and Cui [15] also clusters DOA, FC and PW parameters. It has origins on the density-based clustering method of [16], but its self-adaptive features allow the determination of the density threshold by the data itself and the generation of multiple density thresholds per the characteristics of the incoming radar signals.

In the work of Sheng, Hou and Si [17], clusters are defined by the smallest spheres that enclose a nonlinear transformation of vectors consisted of the PW and FC parameters of incoming pulses. Nevertheless, the authors themselves assume that the number of computations required by this method, known as support vector clustering, is very high and impracticable. Therefore, they suggest dividing the entire set of pulses in smaller subsets, but the method is restricted to environments that are not electromagnetically dense.

Regardless of the type of the clustering method that is used, the increasingly ability presented by modern radars of varying the parameters of PW and FC requires also increasingly elaborated techniques and computational power on all the multiparameter clustering-based radar detectors [2].

In the literature, the above approaches consist of the state-of-the-art of processing pulses, classifying patterns and identifying radars in modern scenarios, but they are not useful to the purposes of this work, since they do not prime for simplicity and they demand great computational power.

To reach the objectives of this work, rather than designing complex and demanding algorithms, the approach of work achieves robustness by examining simple details of the problem defined on Section 1.2 – such as, for instance, the superimposing of pulses in the time domain, which leads in the missing pulses phenomenon in traditional detectors; the irregularities in antenna patterns, which cause DOA measurement ambiguities; and the features of the receiver employed, that reflect on the POI, on the availability of FC information and on the features of the DOA measurement distributions. After such considerations on the early stages, substantial enhancements are promoted, first, to a Gaussian kernel density estimator, allowing the glimpse of a Gaussian filter whose purpose is to cluster pulses by their DOA, and then to a classical interval-only deinterleaving method [18].

Frame 1.1 shows the features of the state-of-the-art radar signal processing works and of the present research, for comparative purposes.

Frame 1.1 – Features of the state-of-the art and of this work.

Work	Year	Approach	Restrictions	Simplicity	Low processing power	Missing pulses sensitive
[9]	2015	Hilbert transform / filtering / rule-based classifier	only stable and staggered PRI	no	no	yes
[10]	2015	wavelet transform / support vector machine	none	no	no	yes
[12]	2014	correlate PA and scan patterns / decision tree	only air-to-air	no	no	yes
[14]	2017	nonlinear least squares / neural network clustering	only air-to-air	no	no	yes
[15]	2015	self-adaptive density-based clustering	none	no	no	yes
[17]	2017	support vector clustering	only non-dense EM scenarios	no	no	yes
Ours	2018	Gaussian-filtering DOA measures / enhanced interval-only method	none	yes	yes	no

Source: own elaboration.

## 1.6 RELATED PUBLISHED WORKS

The knowledge employed on this research was obtained during the development of the following works, during the master's degree program:

- **Paper 1:** Polarization diversity on ESM systems [19].  
**Vehicle:** Journal of Microwaves, Optoelectronics and Electromagnetic Applications (JMoe);  
**Abstract:** Polarization diversity antenna arrays are applied to Electronic Support Measures (ESM) systems since the 1980s. However, even today modern systems are conceived with the employment of the traditional and inconvenient spiral antennae and there are no studies that evidences most of the benefits of this technique applied to them. This paper aims at showing not only the advantages on polarization matching issues, but also the benefits in gain, in simpler truncation effect problems and in costs and time spent on design and production. After a brief approach strictly applied to ESM of the main features of spiral antennae and bow-tie antennae compounding a polarization diversity array, equations of the power available from the last were developed from the concept of effective length. The results demonstrate that the array could provide a power 8.7 dB higher than a modern spiral would to an ESM system when it receives vertical or horizontal linearly polarized waves, which multiplies by 2.7 the range of the system, besides also presenting a better performance in case of circularly polarized incident waves. This work has contributed to propose a replacement to the very common use of spiral antennae on the upcoming ESM system projects. This study is recommended for the areas of Electronic Warfare, Electromagnetic Devices and Applications and Ultra-Wideband Antennae.
- **Paper 2:** Proposta de um MAGE RDS com processamento em tablet: desafios de hoje e perspectivas do amanhã [20].  
**Vehicle:** Revista Spectrum 2016;  
**Abstract:** The voluble interactions between military philosophy and technologies related to advances in digital signal processing show that the concept of Software Defined Radio (SDR) could be used to develop a new way of Electronic Support Measures

(ESM) on tablets. The 5G technology expectations, that promises a revolution in telecommunications, justifies the proposition of a research that aims an SDR ESM System with tablet processing. This paper discusses the main challenges and the prospects for the future related to the research of this equipment.

- **Paper 3:** SDR-based radar-detectors embedded on tablet devices [21].

**Vehicle:** 2017 SBMO/IEEE MTT-S International Microwave & Optoelectronics Conference (IMOC 2017).

**Abstract:** Software-Defined Radio (SDR) technology has already cleared up passive radar applications. Nevertheless, until now, no work has pointed how this flexible radio could fully and directly exploit pulsed radar signals. This paper aims at introducing this field of study presenting not only an SDR-based radar-detector but also how it could be conceived on a low power consumption device as a tablet, which would make convenient a passive network to identify and localize aircraft as a redundancy to the conventional air traffic control in adverse situations. After a brief approach of the main features of the equipment, as well as of the developed processing script, indoor experiments took place. Their results demonstrate that the processing of pulsed radar signal allows emitters to be identified when a local database is confronted. All this commitment has contributed to a greater proposal of an Electronic Intelligence (ELINT) or Electronic Support Measures (ESM) system embedded on a tablet, presenting characteristics of portability and furtiveness. This study is suggested for the areas of Software-Defined Radio, Electronic Warfare, Electromagnetic Devices and Radar Signal Processing.

- **Paper 4:** Demonstrador de um sistema MAGE com a antena do P-95 e processamento em tablet [22].

**Vehicle:** XIX Simpósio de Aplicações Operacionais em Áreas de Defesa (SIGE 2017);

**Abstract:** A Software-Defined Radio (SDR)-based Electronic Support Measurement (ESM) system demo with tablet processing and the antenna of the ESM system of the P-95



aircraft is presented. Experiments showed that the system, when confronted with characteristic emissions of radar signals, was able to detect pulses and their parameters with an error rate of about 0.05% when only one signal was received or when a complex electromagnetic environment was simulated. The system was also able to detect superimposed pulses, in addition to identifying simulated emitters according to a pre-recorded database. The results of this work suggest that the processing capacity of the tablets and the SDR technology approach now allow ESM systems to operate on these portable and convenient devices.

- **Paper 5:** Precise techniques to detect superimposed radar pulses on ESM systems [23].

**Vehicle:** IET Radar, Sonar & Navigation;

**Abstract:** The latest works on the radar pulse deinterleaving in Electronic Support Measures (ESM) systems have not completely solved the missing pulses problem yet. We present a pulse detection algorithm that aims at, if not eliminating it, diminishing the rate of pulses not detected because of the fact of being superimposed in other ones. Experiments set up on an ESM system based on Software-Defined Radio (SDR) showed that the algorithm detection rate was near a hundred percent and the false alarm rate was near zero when pulse amplitudes were higher than 3.9 mV in the SDR input. This work is suggested for the areas of Digital and Radar Signal Processing and Electronic Warfare.

## 1.7 OUTLINE OF THE DISSERTATION

This study is further organized and structured as follows:

- Chapter 2 carries about the pulse measurement algorithm;
- Chapter 3 shows the proposed DF technique;
- The DOA-based clustering of pulses is shown in Chapter 4;
- The deinterleaving procedure to be made inside each DOA-based cluster is approached on Chapter 5; and
- Chapter 6 concludes the dissertation.



## 2 PULSE MEASUREMENT

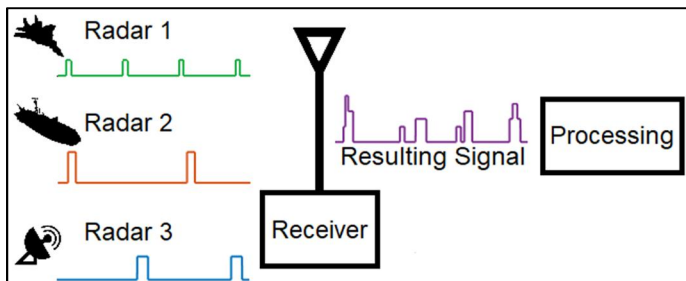
All the recent published papers about radar signal processing mentioned on Section 1.5 [9-17] have in common the fact that they are somehow sensitive to missing pulses – a phenomenon mentioned on Section 1.2 in which the radar detector does not detect every pulse emitted by a radar and which makes pattern recognition methods not succeed on deinterleaving radar signals, or makes them request more processing stages to do that [2].

In the classical work of Mardia [18], this problem was already identified, and the author dealt with it weighting the threshold level to be exceeded on histograms that register occurrences of differences of sequential TOAs. On this approach, if missing pulses avoided the threshold surpassing, true PRI patterns would not be detected. On the other hand, if the threshold was excessively lowered by the weighting, false PRI patterns would be indicated. Subsequent papers based on histograms, for instance [24, 25], have tried to improve the threshold weighting, but they have not found a better solution to this issue.

A technique frequently employed to measure pulses relies on the crossing of a predefined threshold level by the PA envelope. Unfortunately, common detection algorithms fail when two or more pulses from different emitters overlap [2], which could lead to the occlusion or distortion thereof. Fig. 2.1 consists of an extract of Fig. 1.6 and illustrates the signal resulted from the superimposing of pulses of radars 1-3.

This chapter introduces a pulse measurement technique that can process pulses which are superimposed in the time domain, such as the couple consisted of the first pulse of Radar 1 and the first pulse of Radar

Fig. 2.1 – Interleaved signals received by a radar detector.



Source: own elaboration.

2 and the couple consisted of the last pulse of Radar 1 and the last pulse of Radar 3. The proposed method is related to tasks (a) and (b) of Fig. 1.10 and differs from conventional ones in that it focuses on the variations of the resulting amplitude envelopes.

To explain the development of the algorithm, studies of the behaviour of a generic radar detector receiver subjected to two pulses at a time are presented. Cases in which pulses present different FC and in which components present nonlinear response are covered, as well as A/D conversion issues. Moreover, an experiment implemented on a Software-Defined Radio (SDR)-based ESM system showed that the performance of the proposed algorithm degrades only when the amplitude envelopes are lower than 3.7 mV on the input of the used SDR.

## 2.1 PRELIMINARIES

The presence of two or more pulses at the same time in a generic radar detector receiver may result in an amplitude envelope other than the superposition of the single envelopes, depending on their FC and/or phase-mismatching. Nevertheless, enough information is available to detect superimposed pulses if an algorithm based on comparing variations of the resulting envelope is used, since to the beginning and to the end of each pulse are associated certain variations of the envelope which are symmetric between each other.

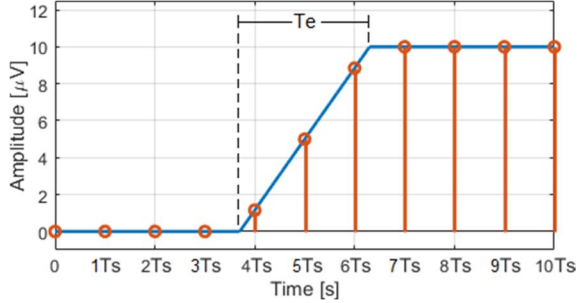
The comparison between variations, however, must consider peculiarities of radar detectors, which look to handle various combinations of  $P_{tx}$ ,  $G_{tx}(\theta_{tx}, \Phi_{tx})$  and  $R$  in (1.1), commonly presenting nonlinear receivers in the modern context, as explained in Section 1.2. In the output data of such a receiver, the comparison of the variations related to the begin and to the end of a pulse fails if those variations do not occur close to the same amplitude level. Therefore, signal processing techniques, for instance [26], must be used to correct the nonlinearity of a system that uses the proposed algorithm.

In parallel, priming for the greater possible values of  $R_{max}$  in (1.2), the processing must request the lowest possible value of  $SNR_o$ , when amplitude variations related to noise are significant with respect to variations related to the amplitude envelope of pulses. This issue must be faced with a variation threshold level.

Moreover, the relation between the rise/fall time of pulses of a radar signal and the sample time of the A/D converter of the radar detector can lead to the spreading of pulse edges among various samples

of the measured data and can influence on how the sample value variations become arranged. It can make the variations that characterize begin and end of a pulse to be different between each other. Consider a pulse with random TOA and rise time equal to  $T_e$ . Fig. 2.2 illustrates the sampling of its leading edge by a radar detector with sample time of  $T_s$ .

Fig. 2.2 – The sampling of the leading edge of a generic pulse.



Source: own elaboration.

Observe that the leading edge illustrated in Fig. 2.2 lies on  $n_i$  intervals between samples, occupying them even if not completely. The probability of the event  $\tau_{n_i}$ , in which a leading edge lies on exactly  $n_i$  intervals between samples, is:

$$P_l(\tau_{n_i}) = \begin{cases} 2 - n_i + \frac{T_e}{T_s}, & (n_i - 2) T_s < T_e \leq (n_i - 1) T_s \\ n_i - \frac{T_e}{T_s}, & (n_i - 1) T_s < T_e \leq n_i T_s \\ 0, & otherwise \end{cases}$$

$$n_i = 1, 2, 3, \dots \quad (2.1)$$

If PW is random, (2.1) is used for the probability  $P_t(\tau_{n_i})$  as well, related to the trailing edge of the same pulse, but  $P_l(\tau_{n_i}) \neq P_t(\tau_{n_i})$  if rise and fall times are different. Even if  $P_l(\tau_{n_i}) = P_t(\tau_{n_i})$ , both edges of a specific pulse are not necessarily going to lie on the same number of intervals between samples, and even in cases in which both edges are spread in the same number of intervals, the variations between the samples related to each edge are rarely going to present similar

arrangements of absolute values. The solution to this problem is to calculate the moving average of the variations of the sample values. In this procedure, variations that lie beneath the moving average window are all computed, independent of their arrangement. The moving average local maxima, within the range of the window size, characterize position of edges. As it differently affects each sample, noise prevents the moving average procedure from resulting in repetitive sequenced elements, which would make not possible to find local maxima. Noise can also make the local maxima to be displaced – an issue that must be considered on the pulse parameter measurements on low SNR cases. The moving average window size should be defined per the lowest bandwidth radars that the radar detector is designed to confront.

## 2.2 CASE STUDIES

Several case studies exemplifying the issues presented on Section 2.1 can be made with the aid of the hypothetical pulses described on Table 2.1, whose parameters were purposely dimensioned for the convenience of the examples:

Table 2.1 – Hypothetical pulses.

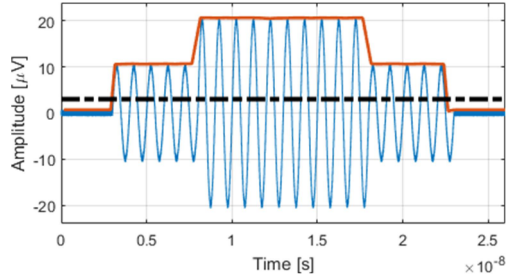
Id	TOA (ns)	PW (ns)	PA ( $\mu$ V)	FC (GHz)	Initial Phase	Rise (ns)	Fall (ns)
P1	3	20	10	1	0	0.25	0.25
P2	8	10	10	1	0	0.25	0.25
P3	8	10	10	1	150°	0.25	0.25
P4	8	10	10	3	0	0.08	0.08
P5	8	10	10	10	0	0.02	0.02
P6	3	10	20	1	0	0.25	0.25
P7	37 (42)	random	10	1	0	26.4	22.6

Source: own elaboration.

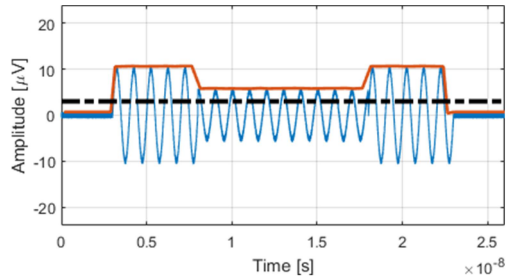
### 2.2.1 Superimposed pulses on a generic receiver

Suppose that P1, combined with P2, P3, P4 or P5, was available on the terminations of a linear-response frequency-independent antenna, whose performance and receiving gain  $G_{rx}$  are not function of the wavelength  $\lambda$ . The resulting amplitudes (in blue) and the crossing of a threshold level (in dashed black) by their envelopes (in red) are shown in Fig. 2.3, considering a low noise floor of -110 dBm/Hz@50 $\Omega$ .

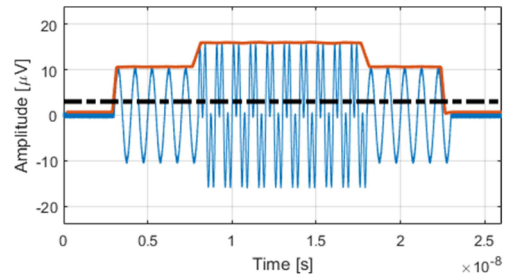
Fig. 2.3 – Superimposed signals  
 (a) P1+P2, (b) P1+P3, (c) P1+P4 and (d) P1+P5.



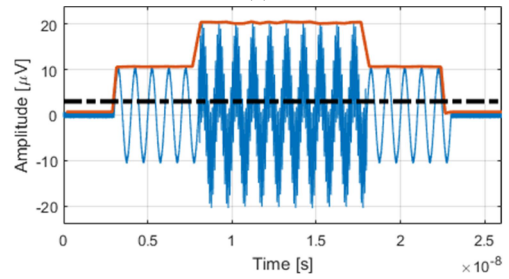
(a)



(b)



(c)



(d)

Source: own elaboration.

A common amplitude envelope-based algorithm detects only P1 in all the cases of Fig. 2.3 – as in all the cases the envelopes cross up the threshold level only in the begin of P1 and then they cross it down only at its end – even when the superimposed pulses are frequency separated. A worst case, in which two minor and untrue pulses would be indicated, would occur if P3 initial phase were nearer  $180^\circ$  in Fig. 2.3 (b), as the envelope would cross down the threshold in the begin of P3, computing a pulse end, and would cross it up at its end, recording a pulse begin.

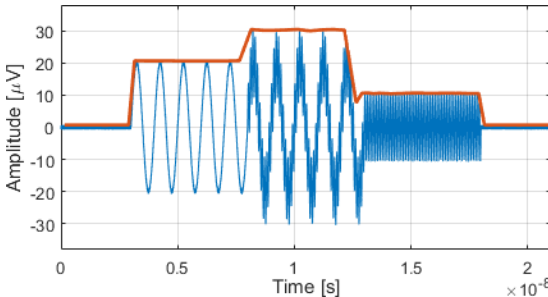
## 2.2.2 Nonlinearity correction and low SNR case

Logarithmic receivers are frequently used on radar detectors to obtain radar signals on baseband while handling with extensive combinations of  $P_{tx}$ ,  $G_{tx}(\theta_{tx}, \Phi_{tx})$  and  $R$  in (1.1). The output  $F(t)$  of an ideal logarithmic receiver can be modelled as the envelope function  $E(x)$  of a logarithmic scale of the IP of its input  $v(t)$ :

$$F(t) = E \left\{ 10 \log \left[ G \frac{v(t)^2}{Z_0} \right] \right\} \quad (2.2)$$

where  $G$  is a gain factor and  $Z_0$  is a reference impedance. Suppose that a frequency-independent antenna, located at a distance  $R = r$  from two radars located at a single platform, provides a receiver with the already seen P5 together with P6, which TOA is 3 ns and PW is 10 ns. Fig. 2.4 shows the superimposed pulses and the resulting envelope on the antenna terminations, again with  $-110 \text{ dBm/Hz}@50\Omega$  of noise floor at this stage. Observe that P5 and P6 have different amplitudes.

Fig. 2.4 – Combination of P5 and P6 at antenna terminations.

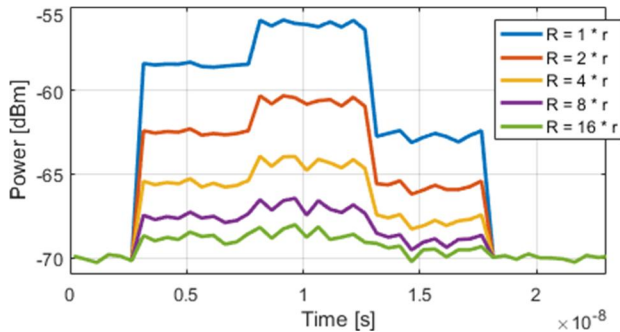


Source: own elaboration.



Consider that the radar detector receiver has a response such as that modelled on (2.2), with  $G = 100$ ,  $Z_0 = 50 \Omega$  and a receiver input-referred noise floor of  $-90 \text{ dBm/Hz}$ . Fig. 2.5 illustrates the receiver output, which represents the envelope of the input IP after gain stages, in  $\text{dBm}$  scale. In addition to the case of Fig. 2.4, in which  $R = r$ , cases in which the receiving antenna would be located at distances  $R = 2r$ ,  $R = 4r$ ,  $R = 8r$  and  $R = 16r$  from the platform are also considered.

Fig. 2.5 – Output of a logarithmic receiver with P5 and P6.



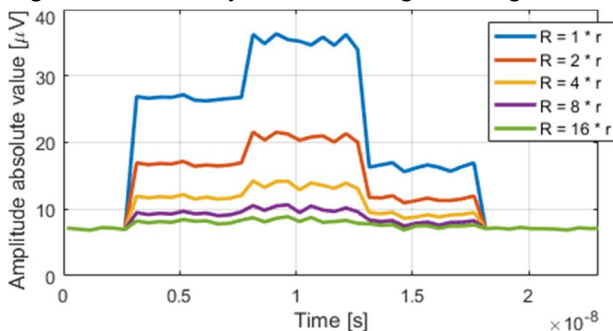
Source: own elaboration.

The input-referred noise floor appears on the output as  $-70 \text{ dBm/Hz}$ . The higher the distance  $R$ , the lower the SNR and the higher the presence of variations related to noise on the output. The response of the modelled receiver makes the leading and trailing edges of P5 not to be characterized by the same variations on the output signal in all the illustrated cases. The same occurs with the edges of P6. The inverse function  $F_i(t)$  of the nonlinear response of (2.2) is:

$$F_i(t) = \sqrt{\frac{Z_0}{A} 10^{\left[\frac{F(t)}{10}\right]}} \quad (2.3)$$

The nonlinearity correction of the cases of Fig. 2.5, obtained using the output of (2.2) as an input of (2.3), are represented in Fig. 2.6. Observe that the variations related to the leading and trailing edges of P5 present close absolute values. The same happens with the variations of P6. Also, the variations related to P5 and P6 are practically indistinct from those relative to noise on the cases in which  $R = 8r$  or  $R = 16r$ , indicating that in these cases the SNR is not enough to occur proper processing.

Fig. 2.6 – Nonlinearity correction of signals of Fig. 2.5.



Source: own elaboration.

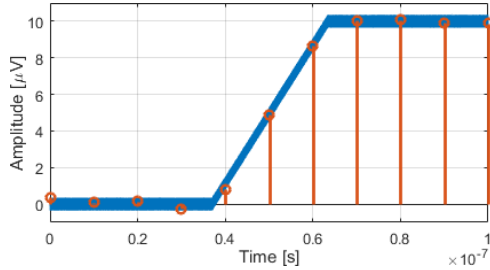
### 2.2.3 Sampling

Regarding to A/D conversion, Fig. 2.7 illustrates the sampling of the envelope leading edge of P7, whose rise time is 26.4 ns, by a radar detector whose sample time is 10 ns: (a) shows the P7 leading edge at TOA = 37 ns, and (b) shows the sample value variations related to it; (c) exemplifies the case if TOA of P7 were not 37 ns, but 42 ns, and (d) illustrates the new arrangement of sample value variations.

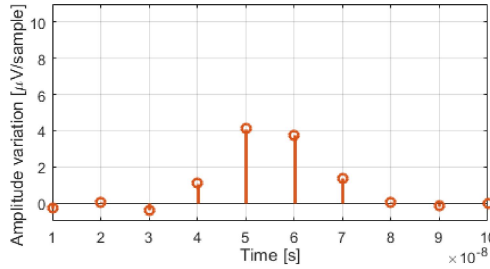
On the case in which the TOA of P7 was 37 ns, the edge measurement resulted in 4 variations between samples, as shown in (b); but if TOA were 42 ns, there would be only 3 variations related to the edge, as illustrated in (d).

Consider, from now on, a pulse with random TOA, random PW, rise time of 26.4 ns and fall time of 22.6 ns. Its leading edge does not fit in only 1 interval between the samples of a radar detector with sample time  $T_s = 10$  ns; it does not fit in only 2 intervals as well – that is why the third sentence of (2.1) determines that the probability  $P_l(\tau_1)$  is zero, just as  $P_l(\tau_2)$ . Using the second sentence of (2.1), the probability  $P_l(\tau_3)$  is 36 %. According to its first sentence,  $P_l(\tau_4)$  is 64 %. The priorly mentioned leading edge is not long enough to lie on 5 or more intervals, so again the third sentence of (2.1) rules, defining  $P_l(\tau_{5,6,7,\dots}) = 0$ . In relation to its trailing edge,  $P_t(\tau_1) = 0$ ,  $P_t(\tau_2) = 0$ ,  $P_t(\tau_3) = 74$  %,  $P_t(\tau_4) = 26$  %, and  $P_t(\tau_{5,6,7,\dots}) = 0$ . The probability that both leading and trailing edges of a pulse with both rise time and fall time like those of P7 are spread among exactly 3 intervals is only 26,6 %, while among exactly 4 intervals is only 16,6 %.

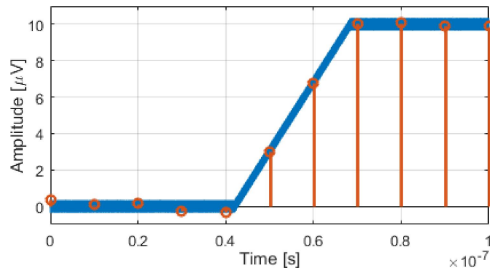
Fig. 2.7 – P7 measurements at 10 ns sample time.  
 (a) TOA = 37 ns, (b) variations related to (a),  
 (c) TOA = 42 ns, and (d) variations related to (c)



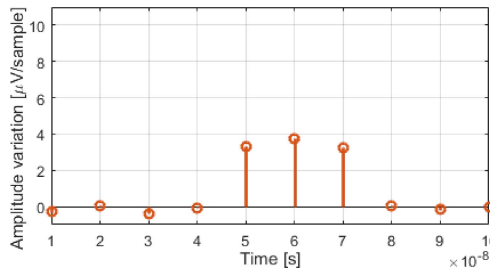
(a)



(b)



(c)

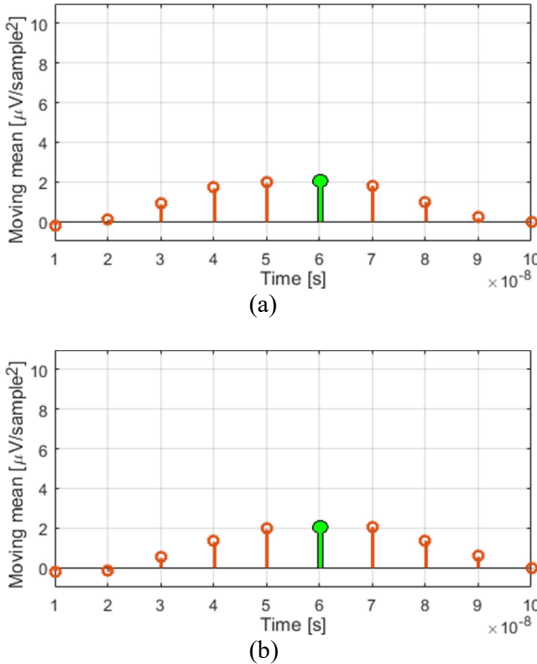


(d)

Source: own elaboration.

Fig. 2.8 illustrates the moving average procedure of the P7 sample variations in both TOA = 37 ns and TOA = 42 ns cases, with a moving average window size of 5 samples. The local maxima are highlighted.

Fig. 2.8 – Moving average of P7 sample value variations when (a) TOA = 37 ns and (b) TOA = 42 ns.



Source: own elaboration.

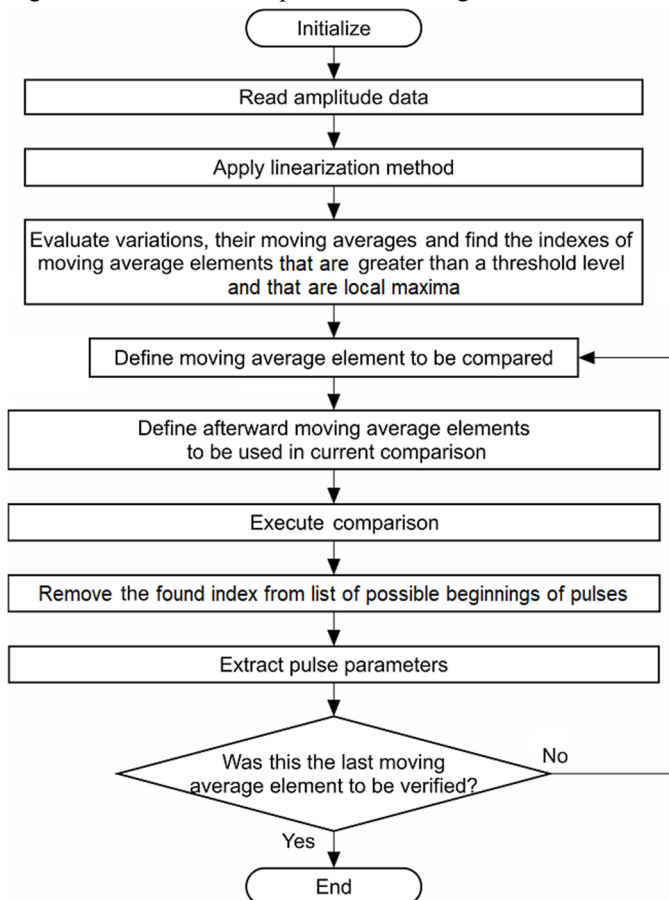
Despite the different arrangements of variations shown on Fig. 2.7 (b) and (d), Fig. 2.8 (a) and (b) show similar dispositions of the moving averaged variations, with the same sample being identified as the local maximum. This indicates that the moving average procedure makes the algorithm robust to the sampling issues.

The moving average window size is dimensioned according to the lowest bandwidth radars the radar detector is designed to confront. In parallel, the higher the window size, the greater the number of mathematical operations performed on the procedure and the required computational power.

### 2.3 PROPOSED ALGORITHM

Besides the details presented in Section 2.1 and Section 2.2, another issue received special attention on the design of the proposed pulse measurement algorithm: the higher the sampling rate  $f_s$  of a radar detector, the higher its resolution in the detection of PW and PRI, as mentioned in Section 1.2. This means that the maximum performance should always be sought, thereby allowing the largest amount of data to be processed by the hardware. Fig. 2.9 shows the flowchart that represents the algorithm to be presented.

Fig. 2.9 – Variation-based pulse detection algorithm flowchart.



Source: own elaboration.

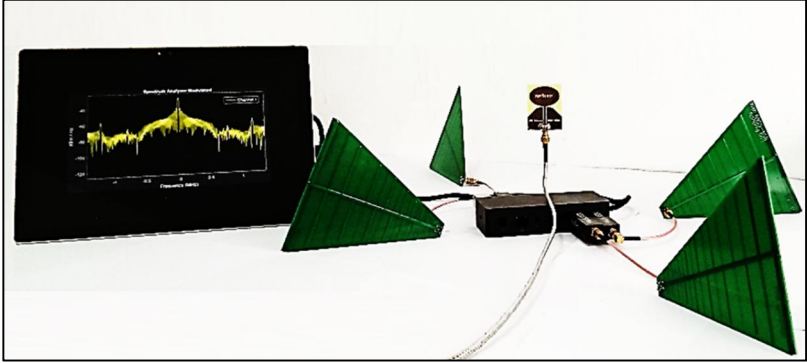
The first step of the algorithm is to correct the nonlinearity on the amplitude data vector. If the receiver response is like that modelled on (2.2), the amplitude data vector is simply used as an input of (2.3). If the response is of another type, as long as it is a nonmemory one, it may be modelled by polynomial regression, so that its inverse function may be approximated and applied to the amplitude data vector on this stage. Thereafter, variations between the nonlinearity corrected amplitude data elements are calculated and the moving average procedure is done. To circumvent the high sampling rate  $f_s$  issue, a procedure to unlink the processing of the algorithm and the high number of samples takes place. In the moving average vector, only the absolute values that exceed a variation threshold level are verified as local maxima; the moving average variations related to those that satisfy these two conditions are registered as potential beginnings or ends of pulses. From now on, the demanded computational power is related to the time-density  $\rho_p$  of pulses of the environment and not to the  $f_s$ . Following, each registered moving average variation is compared only to the afterward registered moving average variations. The first symmetric one, respecting a tolerance, defines the end of the pulse and permits the extraction of parameters as PW, TOA and PA. When a variation is detected as the end of a pulse, it is removed from the list of potential beginnings of pulses.

## 2.4 EXPERIMENTAL SETUP

The validation of the proposed algorithm has occurred with its implementation in a prototype of a four-channel SDR-based ESM system with processing on a tablet device. Its testings were performed in front of a pulse emitter also based on SDR.

The prototype utilizes  $n_{ch} = 4$  log-periodic receiving antennae, model LP850, with nominal frequency range from 850 MHz to 6500 MHz, from Kent Electronics [27]. Also, it uses  $n_{ch} = 4$  NooElec RTL-SDRs™ [28] as receivers, all of them set with an  $f_s = 2.4$  MS/s. The channels of the prototype are synchronized by known pulses emitted by a sun-flower antenna. As a processor, it uses a Microsoft Surface Pro 4™ [29] tablet device. Despite the high quality of the Surface Pro 4 tablet, this device has not the same computational power of modern radar signal processors, which employ parallel and graphics processing unit computing [30-33]. Therefore, it has provided a great opportunity to verify the algorithm applicability with low computational capability available, according to the general objective of this work. Fig. 2.10 depicts the prototype of the SDR-based ESM system.

Fig. 2.10 – SDR-based ESM system prototype.



Source: own elaboration.

The algorithm was run in Matlab™ [34]. The transfer function of the RTL-SDR was characterized and approximated by a polynomial regression of order 5, which resulted in:

$$F(x) = \frac{1.8}{10^9}x^5 - \frac{3.5}{10^7}x^4 + \frac{2.3}{10^5}x^3 - \frac{6.5}{10^4}x^2 + \frac{2.3}{10^2}x - \frac{2.8}{10^4} \quad (2.4)$$

The observation of (2.4) shows that the response of the RTL-SDR is close to an ideal linear one. The RTL-SDR output values were applied in the inverse function of (2.4), therefore the system response was really close to an ideal linear one. The moving average window size was equal to 4 samples. The variation threshold level was defined from a histogram of sample values, which discriminated the most common sample values, presumed to be those from noise. There are lots of ways of defining threshold levels and they will not be covered on this work. It is important to realize that the definition of the variation threshold based on histograms of the amplitude data vector makes the algorithm to become more sensitive on the cleanest environments. It is expected significant false alarm rates at low level signals. A fixed threshold value would avoid this behaviour, at the cost of diminishing the superimposed pulses detection rate.

The test signals, summarized on Table 2.2, were generated by an USRP® B200 SDR from Ettus Research [35], firstly with an  $f_s = 50.0$  MS/s, and after with an  $f_s = 1.0$  MS/s, to verify the robustness of the algorithm in front of low bandwidth radars. Various gain settings were used, so different rates of probability of detection of pulses  $P_d$  and of false alarm  $P_f$  could be verified according to different SNR cases.

Table 2.2 – Pulses emitted by USRP B200.

Id	First TOA ( $\mu\text{s}$ )	PW ( $\mu\text{s}$ )	PRI ( $\mu\text{s}$ )	PA (ref)	FC (GHz)	$f_s$ (MS/s)
P8	0	10	40	1	0.5	50.0
P9	5	10	40	0.5	0.5	50.0
P10	0	100	400	1	0.5	1.0
P11	50	100	400	0.5	0.5	1.0

Source: own elaboration.

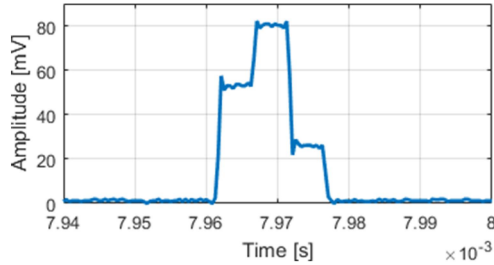
In the first experiment, only P8 was emitted, so detection  $P_d$  and false alarm  $P_f$  rates could be calculated for cases in which there were not superimposed pulses. In the second and third experiments, the PA parameters of P8 and P10 were the reference ones, and the PA of P9 and P11 were set to be half thereof. The final PAs available on the RTL-SDR input for all the cases were defined by the USRP B200 gain and are specified on each line of Table 2.3 to Table 2.5 on Section 2.5. Each experiment was done in a unique data frame of the RTL-SDR with size of  $N = 65,536$  samples. Considering an  $f_s = 2.4$  MS/s, the time  $T_f$  relative to one frame was approximately 27.3 ms. Both P8 and P9 pulses were repeated in intervals of 40  $\mu\text{s}$ . That means that, for each amplitude case, the pulse P8 was received 683 times, in the first experiment. The couples of superimposed pulses P8 and P9 were received 683 times, in the second experiment. Both P10 and P11 pulses were repeated in intervals of 400  $\mu\text{s}$ , which totalized 68 couples of pulses in the period relative to each amplitude case. Fig. 2.11 (a) and (b) illustrate, after the nonlinearity correction, received couples of P8 and P9 when the USRP B200 gain was set to 47 dB and 23 dB, respectively.

## 2.5 RESULTS AND DISCUSSION

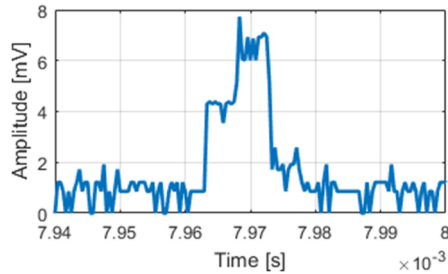
Because the proposed algorithm is based on instantaneous variations of sampled amplitudes, the results shown are based on the PA, and not on the average power or on specific SNR values. The PRI values of 40  $\mu\text{s}$  (P8 and P9) and 400  $\mu\text{s}$  (P10 and P11) were chosen just to repeat the receiving of the superimposed pulses for enough times to estimate  $P_d$  and  $P_f$  rates in a unique RTL-SDR data frame. These PRI values are unusual for pulsed signals which present their PW, and results based on the average power or SNR values would not be realistic ones. Both  $P_d$  and  $P_f$  rates were calculated, in all the cases, relative to the total number of the pulses emitted by the USRP B200 in the period.



Fig. 2.11 – A couple of received superimposed pulses with a gain of (a) 47 dB and (b) 23 dB in the USRP B200.



(a)



(b)

Source: own elaboration.

The results of the first experiment, in which P8 was received by the RTL-SDR alone 683 times, are summarized on Table 2.3, for each amplitude case. It shows that the algorithm provides  $P_d$  near a hundred percent and  $P_f$  near zero for any of the measured cases, in which the isolated pulses presented  $PA \geq 3.9$  mV.

The results of the second experiment, in which 683 couples of superimposed P8 and P9 pulses were emitted by the USRP B200, are presented on Table 2.4. The algorithm exhibits a  $P_d$  near a hundred percent when  $PA \geq 3.7$  mV., with the presence of 10 or fewer impostors on these cases (first to sixth lines). The last line indicates a drop of performance, expected to occur on amplitude cases that result on a SNR below a specific value not discriminated here, for the reasons mentioned on the beginning of this section. This performance would hamper the deinterleaving processing in a hypothetical (and very unlikely) situation in which all the pulses were superimposed.

Table 2.3 – Results of P8 alone.

PA of P8 (mV)	Detected pulses	$P_d$ (%)	False alarms	$P_f$ (%)
44.5	683	100	0	0
31.5	683	100	0	0
23.0	683	100	0	0
15.7	683	100	0	0
11.0	683	100	0	0
7.6	683	100	0	0
5.0	683	100	0	0
3.9	667	97.66	16	2.34

Table 2.4 – Results in front of P8 and P9 superimposed pulses.

PA of P8 (mV)	PA of P9 (mV)	Detected pulses	$P_d$ (%)	False alarms	$P_f$ (%)
44.5	22.0	1366	100	0	0
31.5	15.5	1366	100	5	0.37
23.0	11.8	1366	100	2	0.15
15.7	7.9	1365	99.93	1	0.07
11.0	5.4	1356	99.27	10	0.73
7.6	3.7	1364	99.85	2	0.15
5.0	2.4	1274	93.26	92	6.73
3.9	1.9	597	43.70	376	27.52

Table 2.5 – Results in front of P10 and P11 superimposed pulses.

PA of P10 (mV)	PA of P11 (mV)	Detected pulses	$P_d$ (%)	False alarms	$P_f$ (%)
44.5	22.0	136	100	0	0
31.5	15.5	136	100	1	0.74
23.0	11.8	135	99.26	2	1.47
15.7	7.9	136	100	1	0.74
11.0	5.4	135	99.26	2	1.47
7.6	3.7	136	100	2	1.47
5.0	2.4	123	90.44	5	3.68
3.9	1.9	45	33.09	6	4.41

Source of tables: own elaboration.

Table 2.5 shows the results in front of superimposed P10 and P11 pulses, which both presented  $f_s = 1.0$  MS/s. Again, on the last line, we see a drop on performance, inherent to SNR cases which are below a specific value. In fact, Table 2.5 shows a behaviour on results similar to that of Table 2.4, validating the robustness of the algorithm in front of low bandwidth pulsed signals.

## 2.6 FINAL REMARKS OF THE CHAPTER

The classification and identification of radars, which occurs with the deinterleaving of radar pulses, still suffers from the missing pulses problem, despite the efforts of latest works to make algorithms more robust with respect to this matter.

After preliminaries and case studies, a pulse measurement algorithm which is able to process superimposed pulses and decrease missing pulses rate was presented.

The proposed algorithm accomplishes tasks (a) and (b) of Fig. 1.10. It is based on the variations of the sampled amplitude envelope resulted by the superposition of pulses. It considers linear or nonlinear response receivers, high and low SNR situations, as well as the emitters bandwidth in front of the sampling rate of the radar detector.

An experiment set up with the prototype of an SDR-based ESM system with processing on a tablet device and an SDR pulse emitter showed that the performance of the proposed algorithm degrades only when the amplitude envelopes are lower than 3.7 mV on the input of the used SDR.



### 3 DOA MEASUREMENT

In the modern technological context, from the detector's point of view, the most reliable radar signal parameter is the position of the emitter relative to the detector, which enables the DOA parameter measuring. The reason for this, besides natural phenomena such as jitter and multipath, is that radars, even the civilian ones, are increasingly capable of employing agility features on FC, PW and PRI. None platform of today can move around fast enough to change its position in a considerable range in front of the time order of the PRI [1, 2, 7].

Recent works cannot exploit this reliability while achieving the objective stated on Section 1.4.1. On the one hand, phase or TOA-based methods either are computationally heavy, or they require complicated hardware [36-39]. On the other, most of the amplitude-based techniques utilize analytical formulae, offering the advantage of requiring low computational power, but demanding such a high number  $n_{ch}$  of antennae to divide the angular sector of interest so that only the main lobes of their radiation patterns are computed. In this way, patterns are considered close to Gaussian functions, like that of Fig. 1.9 [8, 40-43].

The present method, related to the task (c) of Fig. 1.10, pushes the needed number of channels  $n_{ch}$  to its inferior limit, with a technique that is not restricted to main lobe zones. Hence, it saves mathematical operations related to measuring pulses in lots of channels, besides the volume, weight and costs related to the channels themselves. The real pattern of each antenna, not necessarily Gaussian ones, and the PAs of each single pulse found in every channel are considered and compared, using simple operations, with a pre-registered matrix of relation of PAs.

Very few works, such as [44], consider the real patterns of the employed antennae. However, they do not compute that the performance of even those antennae presumed to present wideband behaviour vary as a function of FC. They evaluate DOA using only two antennae, allowing ambiguities to happen in angular sectors out of the main lobe.

Below, the design of the algorithm is shown with the aid of case studies of analytical methods subjected to real antennae patterns. Thereafter, the algorithm is presented in detail and simulations are performed. Experiments made on the roof of a building with the same SDR-based ESM system used on Section 2.4 showed that the DOA measurement distributions present Gaussian features, with a standard deviation  $\sigma$  as high as the lower the SNR. Finally, the influence of the type of receiver used on the system, tunable or wideband, is discussed.

### 3.1 PRELIMINARIES

Common amplitude-based DF algorithms find azimuthal DOA using the inverse function of formulae, with small variations, as [40-43]:

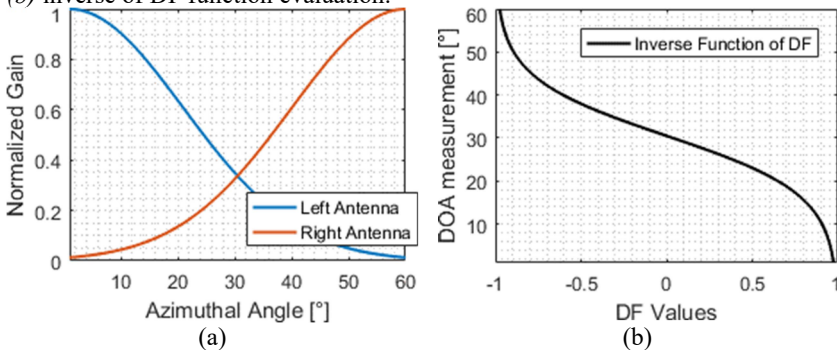
$$DF(\Phi_{rx}) = \frac{PA_{left}(\Phi_{rx}) - PA_{right}(\Phi_{rx})}{PA_{left}(\Phi_{rx}) + PA_{right}(\Phi_{rx})} \quad (3.1)$$

where  $DF: [\Phi_{left}, \Phi_{right}] \rightarrow [-1, 1]$  is the azimuthal DF function. This function is defined from  $\Phi_{left}$  to  $\Phi_{right}$ , which are the azimuthal angles  $\Phi_{rx}$  that respectively maximize the gains  $G_{rx}(\theta_{rx}, \Phi_{rx}, \lambda)$  of the left and the right receiving antennae, for a specific elevation angle  $\theta$ , in a specific wavelength  $\lambda$ . Both  $\Phi_{left}$  and  $\Phi_{right}$  can also be interpreted as the  $\Phi_{rx}$  to where the main lobes of the left and the right antennae are respectively directed.  $PA_{left}(\Phi_{rx})$  and  $PA_{right}(\Phi_{rx})$  are the PA of the same pulse found on the two receivers employed on the measuring.

This approach considers, from  $\Phi_{left}$  to  $\Phi_{right}$ , the patterns of real antennae as ideal Gaussian functions, like that of Fig. 1.9, which are bijective functions. For instance, Fig. 3.1 (a) illustrates Gaussian patterns of two antennae which aim to cover  $60^\circ$  of the azimuth of a DF system that needs  $n_{ch} = 6$  channels to cover the whole azimuth. The DF function is defined here as  $DF: [0, 60^\circ] \rightarrow [-1, 1]$ , a bijective function. The inverse function of  $DF(\Phi_{rx})$  is  $DF_i: [-1, 1] \rightarrow [0, 60^\circ]$ , which provides a DOA measurement without ambiguities – Fig. 3.1 (b).

Fig. 3.1 – Conventional amplitude-based DF methods.

(a) patterns of two antennae in the DF function domain; and  
(b) inverse of DF function evaluation.



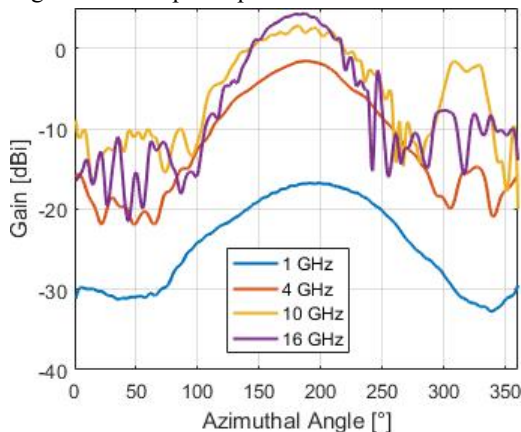
Source: own elaboration.

As seen in Section 1.2, in realistic scenarios, radar detectors face emitters that can operate with an FC parameter situated at a wide range of positions on the RF spectrum. Because of that, in (1.1) and (1.2), the gain  $G_{rx}$  of the receiving antennae of the system, which does not have information about incoming signals, must be considered a function of  $\lambda$  or FC – and therefore is written as  $G_{rx}(\theta_{rx}, \Phi_{rx}, \lambda)$ .

Fig. 3.2 shows the real radiation patterns of a generic spiral antenna, presumed to present wideband behaviour, measured at various FC within its nominal operational frequency range. The formats of the patterns, in any measured FC, barely behave like Gaussian functions from the center of their main lobes, at the azimuthal angle of  $180^\circ$ , to a range of  $+60^\circ$ , until the angle of  $240^\circ$ , or to a range of  $-60^\circ$ , until the position of  $120^\circ$ . Beyond the left and the right ranges of  $60^\circ$ , they present significant sidelobes. Their receiving gain  $G_{rx}$  functions, defined from the center of the main lobe, to the left or to the right, are not bijective functions beyond a  $60^\circ$  range. Conventional amplitude-based  $DF(\Phi_{rx})$  functions, such as (3.1), are not invertible in these cases.

To operate amplitude-based DF techniques in angular sectors outside the main lobe, more than two channels of the system are needed, so ambiguities are extinct. The relation of PAs in every channel of the system must be compared with a pre-registered matrix that contains the relation of PAs in each channel of the detector when signals are incident from various azimuthal angles. This procedure considers every sidelobe of the antennae of the radar detector.

Fig. 3.2 – Example of pattern as a function of  $\lambda$ .



Source: own elaboration.

Observing the patterns of Fig. 3.2, the sidelobes in a specific FC are not even close to that of another FC. Comparisons between a pre-registered matrix obtained in a specific FC and signals with another FC generate significant errors. To face that, knowledge of the FC parameter of each received pulse is needed and the pre-registered matrix to be used in the comparison must be defined accordingly.

Perceive that a simple way to avoid the inconveniences of the sidelobes would be to define the DF function domain with harder angle constraints. To cover the total azimuth in such a case, however, the radar detector would require more channels – and this incurs in negative effects considering the general objective of this research. To achieve this objective, the DOA measurement must be done with minimal volume, weight, costs and computational power, which means that it must demand as fewer channels as possible.

## 3.2 CASE STUDIES

### 3.2.1 Operation in the main lobe zone

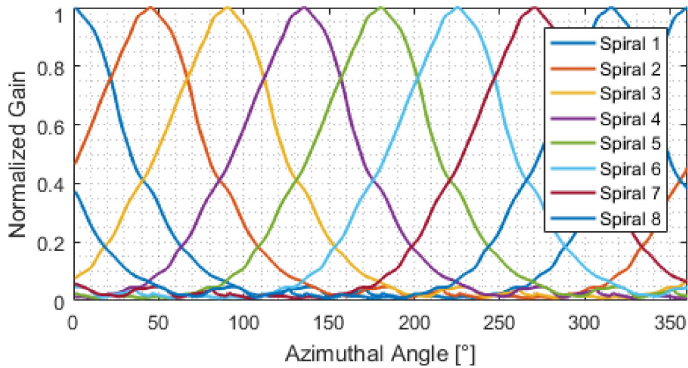
Suppose that a radar detector with  $n_{ch} = 8$  channels is equipped with eight spiral antennae identical to that of Fig. 3.2, each one pointed to a specific sector of  $45^\circ$  of the azimuth.

A pulse that presents  $FC = 4$  GHz is measured in the eight channels of the detector before an amplitude-based analytical DF technique that uses (3.1) takes place. The domains of the eight DF functions, in this circumstance, are defined in ranges of  $45^\circ$ , as  $DF_n: [(n - 1) \times 45^\circ, n \times 45^\circ] \rightarrow [-1, 1]$ ,  $n = 1, 2, \dots, 8$ . Fig. 3.3 (a) illustrates the distribution of the radiation patterns of the eight antennae dividing the  $360^\circ$  of the azimuth, at  $FC = 4$  GHz. The functions were linearized and normalized from 0 to 1. Fig. 3.3 (b) demonstrates the DOA obtaining through the numerical evaluation of the DF function stated by (3.1).

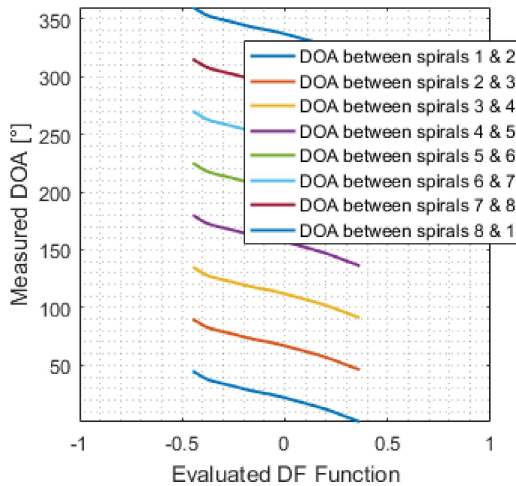
The pattern of the spiral of Fig. 3.2, at  $FC = 4$  GHz, does not present sidelobes in a range of  $45^\circ$  to the left or to the right from the center of its main lobe. With the division of the whole azimuth in eight equal angular sectors of  $45^\circ$ , every sector is covered exclusively by the main lobe of the pattern of two spirals. There are no ambiguities in the DOA measurement. Nevertheless, the costs, the volume and the weight of the equipment are relative to eight receiving channels, and, considering the time-density  $\rho_p$  of pulses, the processor must be capable of handling  $8 \rho_p$  pulses per second in the pulse measurement algorithm.



Fig. 3.3 – Amplitude-based DF technique at 4 GHz with 8 spirals.  
 (a) distribution of patterns in the azimuth; and (b) DOA evaluation.



(a)



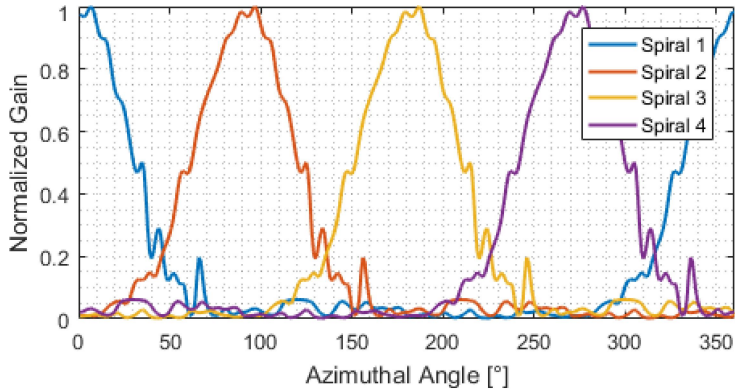
(b)

Source: own elaboration.

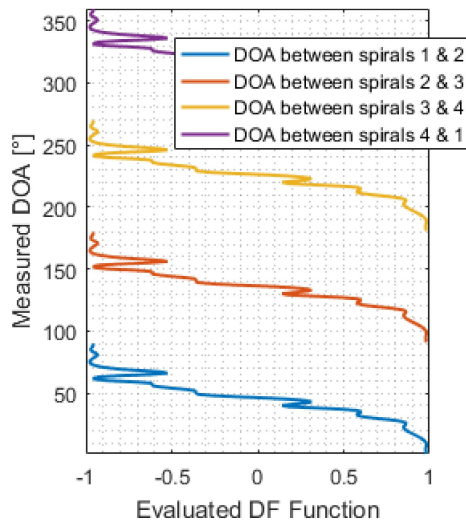
### 3.2.2 Sidelobe ambiguity

Now, suppose that another radar detector presents only  $n_{ch} = 4$  of the spirals of Fig. 3.2, each one directed to a specific sector of  $90^\circ$  of the azimuth. It receives a pulse with  $FC = 16$  GHz. Fig. 3.4 shows the linearized and normalized patterns of the antennae along the azimuth. It also demonstrates the estimation of DOA using the inverse of (3.1).

Fig. 3.4 – Amplitude-based DF technique at 16 GHz with 4 spirals. (a) distribution of patterns in the azimuth; and (b) DOA evaluation.



(a)



(b)

Source: own elaboration.

The DF functions are defined in ranges of  $90^\circ$ , and they are described as  $DF_n: [(n-1) \times 90^\circ, n \times 90^\circ] \rightarrow [-1, 1]$ ,  $n = 1, 2, 3, 4$ . At FC = 16 GHz, the radiation pattern of the spirals presents sidelobes within the range of  $90^\circ$  from the center of its main lobe, to the left and to the right, which makes the equation stated in (3.1) not characterize

bijjective functions. That is why the curves of Fig. 3.4 (b), obtained from inverting (3.1), do not look like functions.

It is clear, here, that the evaluation of analytical DF functions on angular sectors that present sidelobes of the radiation pattern may hamper the measurement. In the sector concerning spirals 1 and 2, from 0 to 90°, for instance, it is not possible to determine DOA, without ambiguities, if  $DF \leq -0.52$ , or  $0.15 \leq DF \leq 0.30$ , or  $0.58 \leq DF \leq 0.60$  or  $0.83 \leq DF \leq 0.87$  or  $DF \geq 0.97$ .

In the illustrated case, ambiguities happen because the sidelobes make signals present repetitive values of amplitudes in the two related channels, in different azimuthal angles. In order to achieve our general objective and operate with a minimal number of channels  $n_{ch}$ , which causes the division of the azimuth in angular sectors that are greater than the main lobes of the antenna patterns, ambiguities must be solved.

Observe that, in Fig. 3.4 (a), the radiation patterns of spirals 3 and 4 present small sidelobes in the azimuthal sector from 0 to 90° – which means that channels 3 and 4 have information that may be able to contribute on solving the ambiguity issue of channels 1 and 2.

### 3.2.3 Frequency of carrier dependence

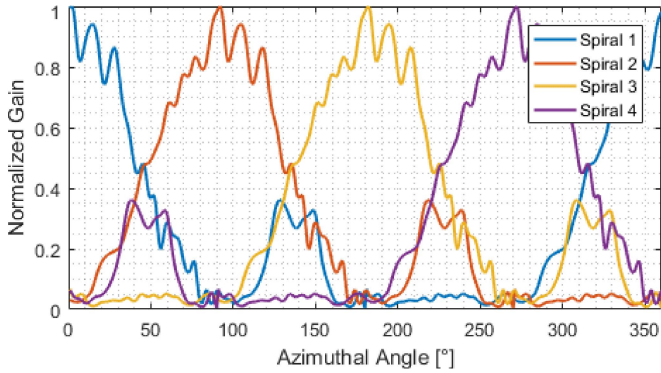
At last, consider that the same radar detector of Section 3.2.2, equipped with  $n_{ch} = 4$  identical spirals which present the radiation patterns of Fig. 3.2, receives a pulse with FC = 10 GHz. Fig. 3.5 (a) illustrates the covering of the whole azimuth by the radiation patterns of the spirals, at 10 GHz. Fig. 3.5 (b) demonstrates the new evaluation of the DF function.

Besides the ambiguities due to sidelobes which are also present at 10 GHz (now at different locations in the graph), there is the presence of an additional issue: the difference of responses of the DF function at 10 GHz and at 16 GHz.

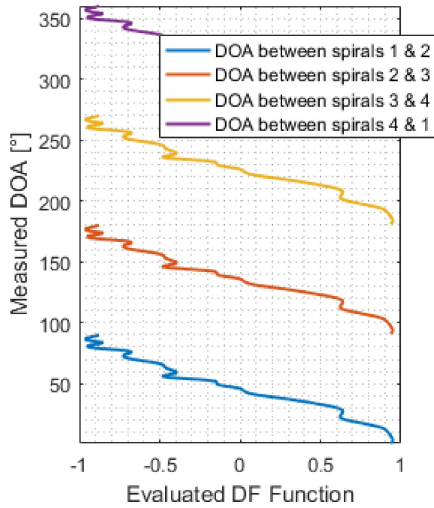
For instance, observe that, in the sector concerning spirals 1 and 2, at 16 GHz, on Fig. 3.4 (b), a value of  $DF = -0.5$  is associated to a DOA = 54°, but at 10 GHz, on Fig. 3.5 (b),  $DF = -0.5$  is associated to a DOA = 68°. At 16 GHz, a  $DF = 0.8$  is associated to a DOA = 29°, but, at 10 GHz, this value is associated to a DOA = 16°.

This behaviour causes a unique platform that present two radars with different FC to be indicated at two different azimuthal positions to the operator of the radar detector – and it indicates that traditional methods are not robust to the variation of the FC parameter.

Fig. 3.5 – Amplitude-based DF technique at 10 GHz with 4 spirals. (a) distribution of patterns in the azimuth; and (b) DOA evaluation.



(a)



(b)

Source: own elaboration.

The variation of radiation patterns with FC, even in antennae which are presumed to present wideband features, evokes the need to associate the known of FC to amplitude-based DF methods, so that the precise measurements can be done according to the proper patterns of the employed antennae – a factor that is not considered on other amplitude-based DF works [40-44].

### 3.3 PROPOSED ALGORITHM

Consider a radar detector with  $n_{ch}$  channels. A measuring procedure, in a specific FC, divides the azimuth in  $m_\phi$  equally spaced angular sectors.

In each of the  $m_\phi$  measurements, to which different azimuthal angles  $\Phi_{rx}$  are associated,  $n_{ch}$  normalized values of PA are respectively registered in the  $n_{ch}$  receiving channels. This procedure generates a collection of vectors  $\vec{v}_i$ ,  $i = 1, 2, \dots, m_\phi$ , whose elements are  $v_j$ ,  $j = 1, 2, \dots, n_{ch}$ , each one containing the relation of PA in each channel, in a specific measured  $\Phi_{rx}$  and at the specific FC. Let  $\mathcal{C}$  be the whole set which contains the collections  $C_k = \{\vec{v}_1, \vec{v}_2, \dots, \vec{v}_{m_\phi}\} \subset \mathbb{R}^{n_{ch}}$ ,  $k = 1, 2, \dots, q_{FC}$ , measured at  $q_{FC}$  different FCs of interest.

Once  $\mathcal{C}$  is known and pre-registered in the radar detector database, consider that, to each incoming pulse with known FC, an  $n_{ch}$ -dimensional vector  $\vec{p}$  of normalized PAs, measured in each channel, is associated.

The DOA of a pulse can be estimated, firstly, through the argument  $i = 1, 2, \dots, m_\phi$  that minimizes the Euclidean distance between  $\vec{p}$  and the vector  $\vec{v}_i$ , contained in a specific  $C_k$  subset, consulted per the FC of the pulse, which defines the discrete  $DOA_i$  domain:

$$d(\vec{p}, \vec{v}_i) = \|\vec{p} - \vec{v}_i\| = \sqrt{\sum_{j=1}^{n_{ch}} (p_j - v_j)^2} \quad (3.2)$$

The evaluation of the Euclidean distance between  $\vec{p}$  and the  $m_\phi$  vectors  $\vec{v}_i$  of a specific  $C_k$  subset takes  $3 n_{ch} m_\phi$  mathematical operations to complete:  $n_{ch} m_\phi$  of them are operations of subtraction,  $n_{ch} m_\phi$  of exponentiation,  $(n_{ch} - 1) m_\phi$  of sum and  $m_\phi$  of square root.

Eq. (3.2) computes the pattern of each antenna of the array, but each one of them influences differently in the resulting value of every evaluation. The use of the weighted Euclidean distance, however, equally considers every antenna of the array in each computation:

$$d'(\vec{p}, \vec{v}_i) = \sqrt{\sum_{j=1}^{n_{ch}} \left( \frac{p_j - v_j}{v_j} \right)^2} \quad (3.3)$$

The computation of (3.3) takes  $n_{ch}m_\phi$  more mathematical operations to conclude than does (3.2), due to the new division operation.

The DOA resolution in the presented method is proportional to the number  $m_\phi$  of vectors  $\vec{v}_i$  contained in each subset  $C_k$ , which defines the discrete  $DOA_i$  domain. In parallel, the higher the number  $n_{ch}$  of elements in each vector  $\vec{v}_i$ , the more information may be available to be used in both (3.2) or (3.3). However, the higher the couple  $m_\phi$  and  $n_{ch}$ , the higher the number of calculations performed on these equations. The number  $q_{FC}$  of  $C_k$  subsets registered in the detector database per FC barely influences in the workload.

The key steps of the presented DOA measurement algorithm are summarized in Frame 3.1.

Frame 3.1 – Summary of the presented DF technique.

- i. Load FC and vector  $\vec{p}$  of measured PAs of incoming pulse;*
- ii. Consult the proper pre-registered subset  $C_k$ , according to the FC of the incoming pulse;*
- iii. Evaluate Euclidean distance between vector  $\vec{p}$  and every vector  $\vec{v}_i \in C_k$ ;*  
  
*or*  
*Evaluate weighted Euclidean distance between vector  $\vec{p}$  and every vector  $\vec{v}_i \in C_k$ ;*
- iv. Assign DOA as the  $\Phi_{rx}$  associated to the  $i = 1, 2, \dots, m_\phi$  that minimized the evaluated Euclidean distances or weighted Euclidean distances.*

Source: own elaboration.

If the receivers are not capable of measuring FC, the detector must be designed with a  $C$  set that contains vectors  $\vec{v}_i$  obtained from the FC that maximizes the accuracy rate of the DOA measuring along all of the FC range of interest. The step *iii* is executed using these vectors.

### 3.4 SIMULATIONS

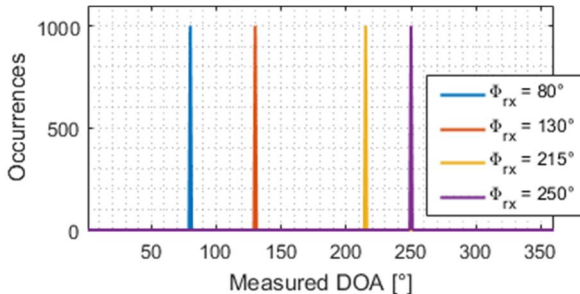
Consider the detector of Section 3.2.2, with  $n_{ch} = 4$  antennae whose patterns are illustrated on Fig. 3.4 (a). From each of the azimuthal positions  $\Phi_{rx} = 80^\circ, 130^\circ, 215^\circ$  and  $250^\circ$ , a thousand pulses arrive at 16 GHz – an FC in which, previously,  $m_\phi = 360$  measurements, in 360 different azimuthal positions  $\Phi_{rx}$ , were made to obtain a subset  $C_1 = \{\vec{v}_1, \vec{v}_2, \dots, \vec{v}_{360}\} \subset \mathbb{R}^4$  and generate the discrete  $DOA_i$  domain.

In relation to Fig. 3.4 (b), at 16 GHz, analytical methods would fail to measure DOA without ambiguities in these  $\Phi_{rx}$  cases. Suppose that the algorithm presented in Chapter 2 is employed to measure the incoming pulses and their PA in each channel, considering absence of noise firstly, and the presented DF technique is used to measure DOA.

Fig. 3.6 shows, in the discrete  $DOA_i$  domain, the measured DOA histogram, simulated using (3.2). It validates the proposed method, which accurately measures DOA without ambiguities in the absence of noise. The result obtained with (3.3) is identical in this noiseless case.

Now, consider the case in which noise influences in the PA measurement in each channel. Consider that a thousand pulses arrive from  $\Phi_{rx} = 140^\circ$  at 16 GHz. Fig. 3.7 shows the superimposed results of the simulation using both (3.2) and (3.3) when additive white Gaussian noise (AWGN) was added to pulses using the Matlab™ [34] function of same name. The function SNR parameter is equal 40, but that does not mean that the real SNR of the signal is 40, for reasons explained on Section 2.5. The formats of the pulses in each channel are also shown so their PA can be seen in front of the noise. The simulation is repeated for a value of 20 on the SNR parameter of the AWGN Matlab function and its results are illustrated on Fig. 3.8, on the same scale as that of Fig. 3.7.

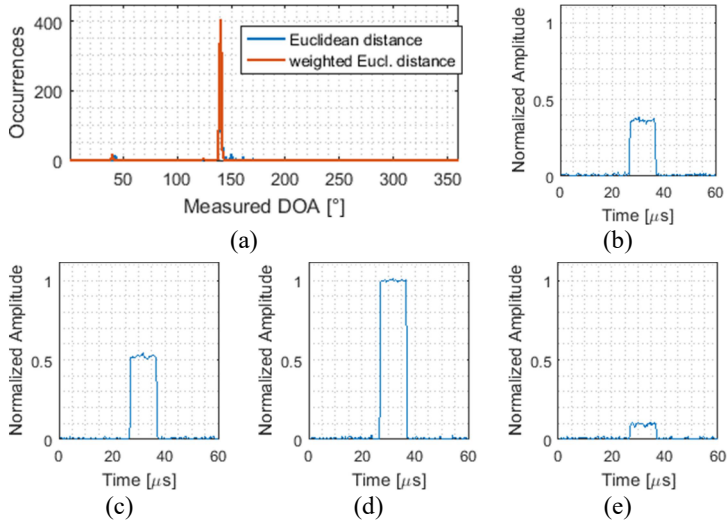
Fig. 3.6 – DOA measurements in the absence of noise.



Source: own elaboration.

Fig. 3.7 – DOA measurement simulation at high SNR.

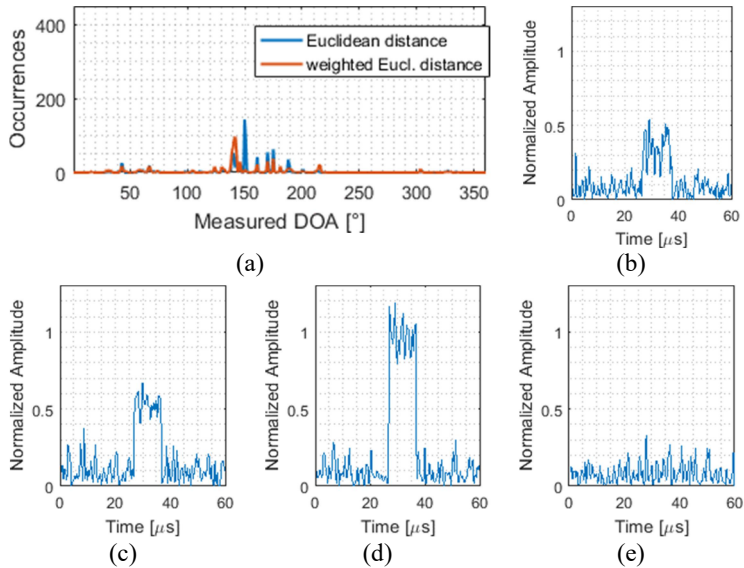
(a) histogram; and (b)-(e) examples of pulse format at channels 1-4



Source: own elaboration.

Fig. 3.8 – DOA measurement simulation at low SNR.

(a) histogram; and (b)-(e) examples of pulse format at channels 1-4



Source: own elaboration.



Fig. 3.7 and Fig. 3.8 exemplify, in the discrete  $DOA_i$  domain, the behaviour of the distributions with the SNR, with Gaussian features and a standard deviation  $\sigma$  as high as the lower the SNR. Fig. 3.8 shows that the weighted Euclidean distance, (3.3), places the Gaussian mean  $\mu$  more accurately at  $DOA_{140}$  than does the Euclidean distance, (3.2).

### 3.5 EXPERIMENTAL SETUP

The same prototype of ESM system used in Section 2.4, which employs  $n_{ch} = 4$  LP850 antennae [27] and NooElec RTL-SDRs [28], was used to verify the presented amplitude-based DF technique. The final disposition of the antennae on the array have assumed a disposition inclined at  $45^\circ$  with the horizon, due to the polarization issues of ESM systems studied on [19]. This disposition cannot be changed from now on. Fig. 3.9 depicts, without connections, the new and definitive disposition of the antennae, supported on a wooden stand.

As in Chapter 2, the experiment was performed with the aid of emissions from the USRP B200 from Ettus Research [35], and the algorithm was run in Matlab™ [34]. The  $C$  set was pre-registered as a  $C(i, j, k)$  matrix on the ESM system database. The FC chosen to verify the method was 1.5 GHz. The  $C$  matrix measuring procedure, performed on a building rooftop, counted on  $m_\phi = 180$  outdoor measurements along the whole azimuth. Thus, the resolution of the system on the discrete  $DOA_i$  domain was equal to  $2^\circ$ , and the  $C$  matrix dimensions were  $180 \times 4 \times 1$ , which can be seen as 1 page containing a  $180 \times 4$  matrix. Operational equipment whose receivers can discriminate FC must contain in their  $C$  matrix as many FC pages as the wanted accuracy

Fig. 3.9 – Definitive disposition of the antennae.



Source: own elaboration.

of DOA measurements against the variation of this parameter.

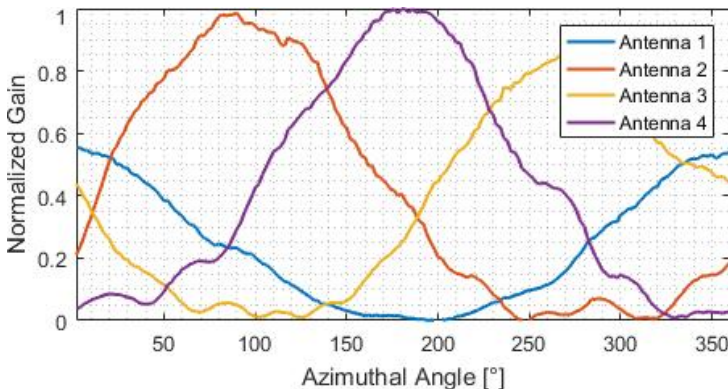
The procedure for obtaining the  $C$  matrix allowed the estimation of the normalized patterns, in outdoor conditions, of the four LP850 antennae of the prototype along the azimuth. The angular position of the antennae, their mutual coupling, reflections on the wooden stand and everything else that influences on their performance are regarded on this measurement. Fig. 3.10 shows the patterns, normalized per the values found in all the four receivers. Observe that, differently from the case studies of Section 3.2, the antennae do not present identical patterns.

To estimate  $DOA_i$ , the weighted Euclidean distance, (3.3), was used. The signals emitted by the USRP B200 had  $PW = 400 \mu s$  and  $PRI = 4 ms$ . First, they were emitted from a position of  $\Phi_{rx} = 126^\circ$ , and then from  $\Phi_{rx} = 250^\circ$ . In each position case, the receiving consisted of 50 data frames, each one with a size of  $N = 262,144$  samples, of the RTL-SDR, whose sampling rate  $f_s = 2.4 MS/s$  resulted in a receiving period of 5.46 s, which corresponds to 1,365 received pulses.

### 3.6 RESULTS AND DISCUSSION

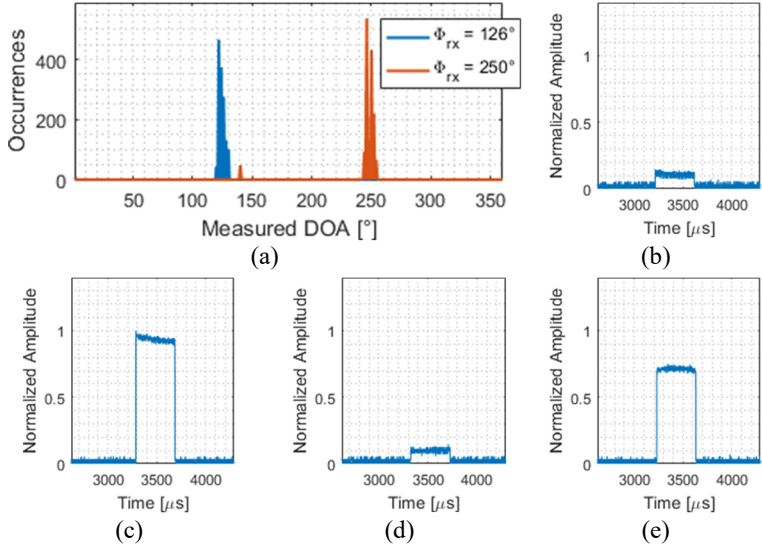
Fig. 3.11 shows, in the same graph, the measuring of DOA of the 1,365 pulses emitted from each position  $\Phi_{rx} = 126^\circ$  and  $\Phi_{rx} = 250^\circ$ . Again, SNR is not specified for the reasons stated on Section 2.5, and therefore formats of pulses are exemplified. The test was repeated with the USRP B200 emitting with a gain 12 dB lower and its results are illustrated on Fig. 3.12, on the same scale as that of Fig. 3.11.

Fig. 3.10 – Estimated prototype normalized patterns at 1.5 GHz.



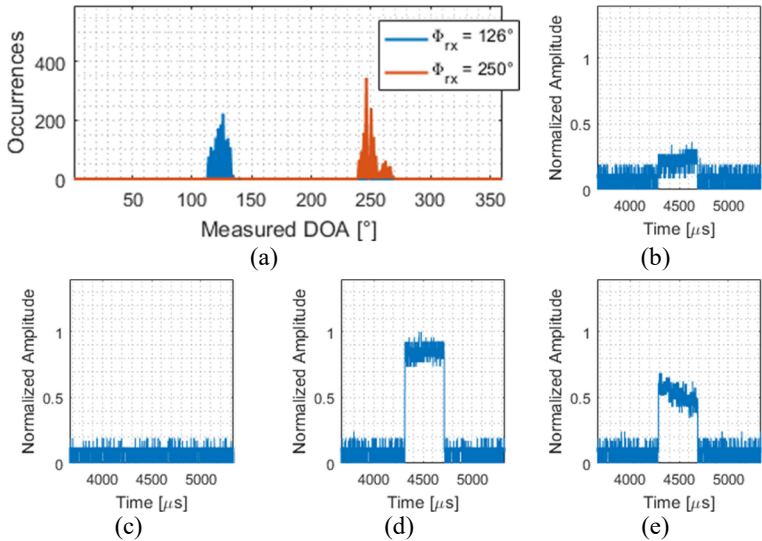
Source: own elaboration.

Fig. 3.11 – Results from DOA measurements.

(a) histogram; and (b)-(e) pulse example from  $\Phi_{rx} = 126^\circ$  at channels 1-4.

Source: own elaboration.

Fig. 3.12 – Results with signals 12 dB below.

(a) histogram; and (b)-(e) pulse example from  $\Phi_{rx} = 250^\circ$  at channels 1-4.

Source: own elaboration.

Results of both Fig. 3.11 and Fig. 3.12 show a behaviour similar to that of Fig. 3.7 and Fig. 3.8, with distributions of measurements with Gaussian characteristics, with a standard deviation  $\sigma$  as high as the lower the SNR in the channels. Moreover, they evidence that, despite the existing dissimilarity between the antennae patterns, the proposed technique correctly places the mean  $\mu$  of the Gaussians close to the DOA angle related to the real  $\Phi_{rx}$  – in the illustrated cases, at DOA = 126° and DOA = 250°.

On Section 1.2, on the explanation around (1.3) and (1.4) about the kinds of receivers typically used on radar detectors, the noise figure  $NF$  of the related LNAs and the bandwidth in the receiving  $BW_{rx}$ , wideband receivers tend to admit more noise than tunable receivers, if the other parameters are unchanged. Thus, it is expected that the distributions of DOA measurements of the proposed algorithm present higher standard deviations  $\sigma$  on systems using wideband receivers rather than on systems employing tunable receivers, if the other elements remain unchanged.

The Gaussian characteristics of the distributions verified on these results suggest, at first, that a nonparametric density estimator based on the Gaussian function may be used to cluster pulses according to their DOA, but the various standard deviations  $\sigma$  of various distributions found on an electromagnetically dense environment, besides the type of receiver used on the system, generate the challenge of choosing the correct scale of the Gaussian function of the estimator.

### 3.7 FINAL REMARKS OF THE CHAPTER

The most reliable radar signal parameter, from the detector's point of view, is the position of the emitter relative to the detector, which enables the DOA parameter measuring. Modern radars are increasingly capable of employing agility features on FC, PW and PRI, but none platform of today can move around fast enough to change its position in a considerable range in front of the time order of the PRI.

This chapter presented a method related to the task (c) of Fig. 1.10 that pushes the number of necessary channels  $n_{ch}$  to reliably measure DOA to its inferior limit. The proposal saves the mathematical operations related to measuring pulses in lots of channels, besides the volume, weight and costs related to the channels themselves.

The design of the algorithm was demonstrated with the support of case studies of traditional analytical methods subjected to real wideband antennae patterns.

Experiments performed in outdoor conditions, on the roof of a building, with the same prototype of SDR-based ESM system used on Section 2.4 showed that the DOA measurement distributions of the method present Gaussian features, with a standard deviation  $\sigma$  as high as the lower the SNR.

The Gaussian characteristics of the distributions verified on these results suggested that a nonparametric density estimator based on the Gaussian function may be used to cluster pulses according to their DOA on the task (d) of Fig. 1.10.

The influence of the type of receiver used on the system, tunable or wideband, was discussed.



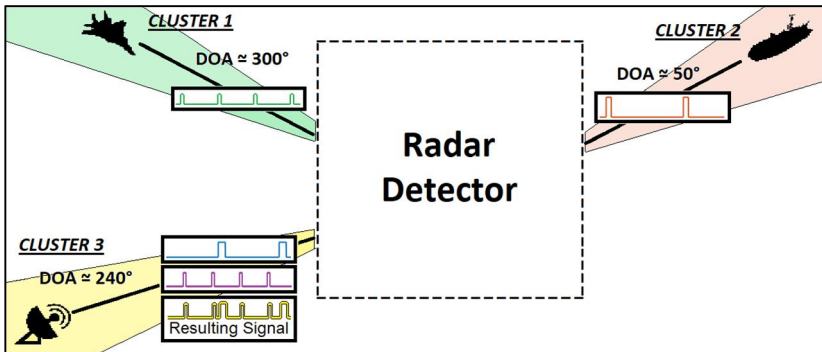
## 4 PULSE CLUSTERING

Once pulses were measured and have their DOA assigned, before identifying surrounding radars, detectors must employ pattern recognition methods to deinterleave the pulses of different emitters from one another [2, 7], as seen in Section 1.2. Various cutting-edge works cited on Section 1.5 [9-17] succeed in doing this task, but they demand great computational power and they are not aligned with the objective of this research, stated in Section 1.4.1.

This chapter presents an algorithm that takes advantage of the reliability of the position of emitters relative to the detector, measured by the DOA parameter. The technique, related to the task (d) of Fig. 1.10, separates pulses in DOA-based clusters before a final method of pattern recognition is employed. It aims to soften the final stage, allowing it to be laborious only when two or more radar platforms are azimuthally close, or a single platform has more than one radar.

Fig. 4.1 is based on the scenario of Fig. 1.3, but shows a new situation in which the terrestrial platform has turned on another radar. The radar detector, thus, receives interleaved pulses from two radars coming from the azimuthal angle associated with the terrestrial platform ( $\Phi_{rx} = 240^\circ$ ). It also receives pulses from the radars embedded on the aerial ( $\Phi_{rx} = 300^\circ$ ) and maritime ( $\Phi_{rx} = 50^\circ$ ) platforms. On the exemplified scenario, clustering the received pulses by their DOAs is sufficient to separate the signals that come from the three platforms. The final deinterleaving stage is therefore necessary only to discriminate the signals of the two radars of the terrestrial platform.

Fig. 4.1 – The clustering of pulses according to their DOA.



Source: own elaboration.

The DF technique presented on Chapter 3 provides distributions with Gaussian characteristics on the discrete  $DOA_i$  domain, with a standard deviation  $\sigma$  as high as the lower the SNR of incoming signals. Taking advantage of that, the proposed method starts from a nonparametric kernel density estimator, using the Gaussian basis function, aiming to detect pulse concentrations and to cluster them. The outcome of this endeavor is a parametric Gaussian filtering procedure. The procedure benefits from the fact that the knowledge of the PA parameter of the incoming pulses allows the prediction of the standard deviation  $\sigma$  of their distributions. This is possible because the features of the system, such as the type of the employed receiver, tunable or wideband, and the behaviour of the employed DF technique are previously known. This proposal requires less mathematical operations to conclude than the nonparametric approach.

To expose the development of the algorithm, the Gaussian filtering procedure is derived from a traditional kernel density estimator that employs the Gaussian basis function. Following that, considerations of real DOA measurement distributions obtained on Section 3.5 are studied with the aim of improving the performance of the clustering, besides saving mathematical operations. After the presentation of the detailed algorithm, at the end of the chapter, a complex scenario, with 6 distributions of DOA measurements, is processed, and the benefits and drawbacks of the method are discussed.

#### 4.1 PRELIMINARIES

As seen on Chapter 3, the distributions of DOA measurements of the proposed DF technique present Gaussian characteristics. In the discrete  $DOA_i$  domain, the mean  $\mu$  of each Gaussian indicates the azimuthal angle  $\Phi_{rx}$  from where pulses come, and the standard deviation  $\sigma$  is a function of their PA.

To detect where, on the discrete  $DOA_i$  domain, pulses are concentrated and to cluster them according to these concentrations, the algorithm must find the means  $\mu$  and the standard deviations  $\sigma$  of the Gaussians. The maximum values of a kernel density estimate, with the Gaussian basis function, at various scales, would accomplish that. Given a set of DOA measurements, with  $n_s$  measured  $doa_s$  samples,  $s = 1, 2, \dots, n_s$ , this technique would evaluate, in the discrete  $DOA_i$  domain, the mean of the Gaussian kernel function of the distances until each measured  $doa_s$  [45]:



$$\hat{f}_h(DOA_i) = \frac{1}{n_s h \sqrt{2\pi}} \sum_{s=1}^{n_s} \exp \left[ -\frac{1}{2} \left( \frac{DOA_i - doa_s}{h} \right)^2 \right] \quad (4.1)$$

where  $h$  is a Gaussian scaling factor that strongly interacts with the standard deviation  $\sigma$  of the Gaussian distributions of DOA measurements and exhibits a strong influence on the resulting density estimate.

A maneuver to avoid the uncertainty generated by the interaction between the scale  $h$  and unknown standard deviations  $\sigma$  of various distributions found on a complex scenario is to evaluate (4.1) in a large range of  $h$  values. This range is defined according to a pre-visualization of the behaviour of the standard deviation  $\sigma$  of the distributions related to the DF technique, within the dynamic range of the employed receivers. Evaluating (4.1) in this range and identifying which  $h$  value results, in each  $DOA_i$ , in the maximum value of density estimate provides not only the location of clusters, but also their size. The number of mathematical operations in this procedure, however, is proportional to the number  $n_h$  of different scaling factors  $h$  contained in the range. The knowledge of the real standard deviation  $\sigma$  of the distribution would circumvent the waste of computational power related to the evaluation of (4.1) in a large range of  $h$  values related to the whole dynamic range of the receivers.

In fact, it is possible to estimate which is the adequate  $h$  value to use in (4.1) in each situation. The PAs of the incoming pulses are known; the system is known; and there is a relation between this parameter and the standard deviation  $\sigma$  of the Gaussian distribution of the DOA measurements.

The number of mathematical operations associated to the evaluation of (4.1) following the steps above is also related to the number  $m_\phi$  of possible measured DOAs, which make up the discrete  $DOA_i$  domain, in the DF technique. This evaluation, in each of the  $n_h$  scales  $h$ , takes  $6 m_\phi n_s$  operations to conclude:  $m_\phi n_s$  of them of subtraction,  $m_\phi n_s$  of them of division,  $m_\phi (2 n_s + 1)$  of multiplication,  $m_\phi n_s$  of exponentiation and  $m_\phi (n_s - 1)$  of sum.

With the aim of saving operations, rather than evaluating (4.1), the histogram *hist* of the measured  $doa_s$  samples can be filtered, in the  $DOA_i$  domain, by pre-generated Gaussians  $g$  on the same scales  $h$ :

$$\mathcal{F}(DOA_i) = \frac{1}{h} \sum_{k=0}^{h-1} \text{hist}[DOA_{(i-k)}] g_{(h-k)} \quad (4.2)$$

As in the first described procedure, the identification of which  $h$  value results, in each  $DOA_i$ , in the maximum filtered value estimates location and size of clusters. Now, however, the number of operations in each scale  $h$  is only  $2 m_\phi h$ :  $m_\phi(h+1)$  of multiplication and  $m_\phi(h-1)$  of sum.

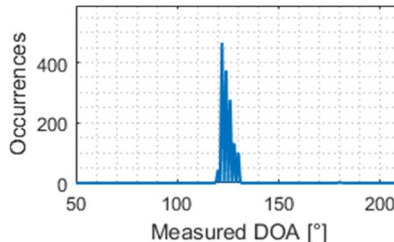
Although the DOA measurement distributions present Gaussian characteristics, they are not ideal Gaussians. Mainly in low SNR cases, the distribution of a unique radar may look like various distributions of different radars which are azimuthally close. If the system had only the information of the distributions of DOA measurements, it would not be possible to distinguish, in this case, if there is only one radar in a low SNR case or if there are various radars which are azimuthally close. This issue is solved, alongside with the correct choice of scales of Gaussian filters, with the definition of a scaled moving average procedure, whose window should be as high as the lower the PA of pulses, which smooths the distributions of DOA measurements. The choice of the correct scales  $h$  and the moving average windows  $w_{MA}$  ensures robustness to the method in front of distributions that are not close to Gaussian functions.

## 4.2 CASE STUDIES

### 4.2.1 Close to ideal Gaussian case

Fig. 4.2 is an extract of Fig. 3.11, and shows the distribution of DOA measurements, in the discrete  $DOA_i$  domain, related to the first experiment with pulses coming from  $\Phi_{rx} = 126^\circ$  made on Section 3.5.

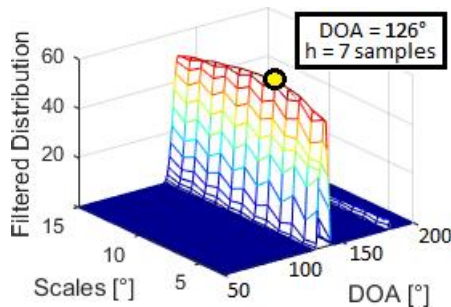
Fig. 4.2 – Histogram of DOA ( $\Phi_{rx} = 126^\circ$ ).



Source: own elaboration.

The filtering procedure of this distribution, with Gaussians at  $n_h = 13$  scales  $h$ , from  $h = 3^\circ$  to  $h = 15^\circ$ , generates the filtered matrix plotted on Fig. 4.3. Here, the lowest and highest  $h$  values are chosen according to the standard deviations  $\sigma$  of the Gaussian distributions pre-visualized when the DF technique processed pulses from the highest to the lowest limits of the dynamic range of the receivers, respectively. The scale of  $h = 3^\circ$  is related to the strongest detectable pulses below saturation, and the scale of  $h = 15^\circ$  is associated to the weakest detectable pulses above the noise floor of the receivers.

Fig. 4.3 – Filtering of histogram of Fig. 4.2.



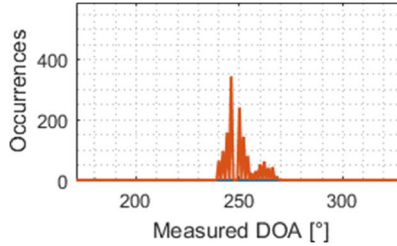
Source: own elaboration.

The local maximum found on  $DOA = 126^\circ$  and  $h = 7^\circ$  indicates that a cluster of pulses should be centered at  $DOA = 126^\circ$ , with a specific size that would be equal to  $7^\circ$ , if the distribution of Fig. 4.2 were an ideal Gaussian function. The data that generated Fig. 4.2 show that the pulses, in fact, are distributed from  $DOA = 117^\circ$  to  $DOA = 130^\circ$ , which totalizes a range of  $14^\circ$ . This indicates that a cluster size adjusting factor (CSAF) must be employed to estimate the size of clusters, due to the fact that the distributions are not ideal Gaussians.

#### 4.2.2 Not close to ideal Gaussian case

Fig. 4.4 is an extract of Fig. 3.12, and shows, in the discrete  $DOA_i$  domain, the distribution of DOA measurements related to the second experiment made on Section 3.5, with pulses coming from  $\Phi_{rx} = 250^\circ$ .

If the procedure of Section 4.2.1 were reproduced here, 3 clusters would be wrongly indicated at  $DOA = 246^\circ$ ,  $DOA = 250^\circ$  and  $DOA = 262^\circ$ . However, the knowledge of the PA of the pulses related to this distribution allows a prediction about its standard deviation  $\sigma$ , since

Fig. 4.4 – Histogram of DOA ( $\Phi_{rx} = 250^\circ$ ).

Source: own elaboration.

the features of the system and the behaviour of the employed DF technique with the employed receivers are previously known, permitting two extra actions:

- a) a scaled moving average procedure, with a window size  $w_{MA}$  according to the PA of the received pulses and the predicted standard deviation  $\sigma$  of the distribution, to smooth and unite it in a unique form; and
- b) the choice of specific values of scales  $h$  to avoid the interpretation of the single distribution as 3 different ones; this choice enables the saving of mathematical operations.

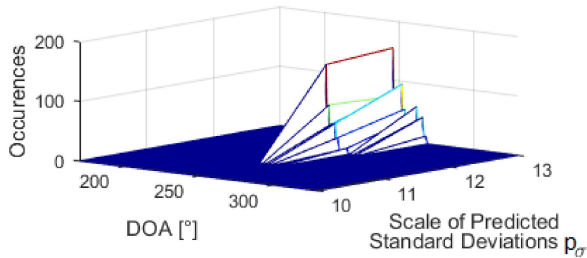
From now on, the DOA distributions are mapped into a  $DOA_i \times p_\sigma$  plane. One of its axes is associated to the DOA parameter. The other is originated from the PA parameter and it is related to a scale of predicted standard deviations  $p_\sigma$ .

The scale of predicted standard deviations  $p_\sigma$  respects the behaviour of the DF technique and receivers employed on the system. The highest predicted standard deviation  $p_\sigma$  of the scale is associated with the highest standard deviation  $\sigma$  that is observed on the distributions of DOA measurements of the system. The results of Section 3.6 show that these distributions happen when the PA is minimal within the dynamic range of the system. Therefore, pulses whose PAs are near the noise floor of the receivers are put on the highest predicted standard deviation  $p_\sigma$  of the scale. Analogously, pulses whose PAs are close to the saturation level of the receivers are put on the lowest predicted standard deviation  $p_\sigma$  of the scale, which are defined according to the lowest standard deviation  $\sigma$  that is observed on the distributions of DOA measurements of the system. The relation between the PA parameter and the scale of predicted standard deviations  $p_\sigma$  is considered linear on this work.

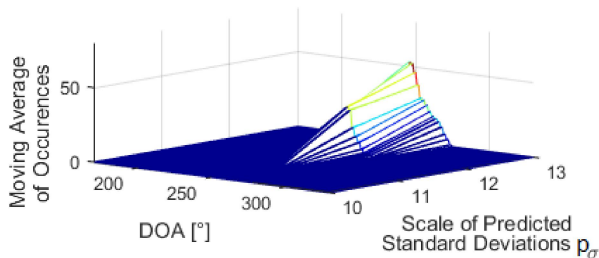
Fig. 4.5 (a) plots the distribution of Fig. 4.4 on the  $DOA_i \times p_\sigma$  plane, and (b) plots its scaled moving average. On the illustrated case, the scale of predicted standard deviations  $p_\sigma$  was divided in 13 values. These values match the  $n_h = 13$  scales (from  $h = 3^\circ$  to  $h = 15^\circ$ ), that were chosen according to the behaviour of the DF technique with the receivers that were used on the experiments of Section 3.5, namely the NooElec RTL-SDRs [28]. Remember that the second experiment of Section 3.5 was originated from emissions from the USRP B200 [35] with a gain 12 dB below from the first. The weak PAs, in that occasion, were registered and, now, they predict the highest values of the standard deviation  $\sigma$  that the distributions may present with the employed DF technique. That is why the pulses are distributed among the highest values of the predicted standard deviations  $p_\sigma$  axis, which indicates to the algorithm the use of wide moving average windows  $w_{MA}$ ; as well as high scaling factors  $h$  in the Gaussian filtering, on the next step.

Fig. 4.5 – Plot of the  $DOA_i \times p_\sigma$  plane.

(a) the pulse histogram is distributed not only in a DOA axis, but also in an axis of predicted standard deviations  $p_\sigma$ ; and (b) a scaled moving average procedure smooths the histogram on the DOA axis.



(a)

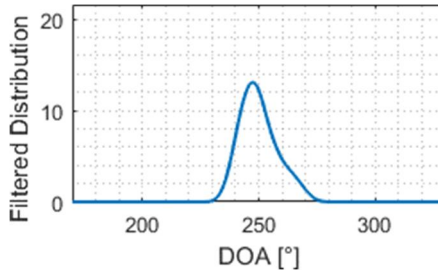


(b)

Source: own elaboration.

The PAs from the pulses from the distribution defined the filtering only at the scales  $h = 14^\circ$  and  $h = 15^\circ$ . Fig. 4.6 shows the maximum values, in each DOA, of the distribution filtered only at these  $n_h = 2$  scaling factors. Finally, the peak that indicates the local of the cluster is obtained. The scaling factor  $h$  in which it happens indicates the size of the cluster.

Fig. 4.6 – Gaussian-filtered distribution.



Source: own elaboration.

The spread of distributions of the discrete  $DOA_i$  domain on a  $DOA_i \times p_\sigma$  plane presents the drawback of enabling that a distribution with a high  $p_\sigma$  value hides behind another with low  $p_\sigma$ , from the prospect of the DOA axis. This happens when more pulses compose the lower  $p_\sigma$  distribution thereby causing its filtering to present a higher value than the one of the higher  $p_\sigma$ . In this case, the cluster size is identified as being smaller than it should be to encompass all the pulses from both distributions. The cluster is delivered to the final deinterleaving stage with missing pulses. If the clusters were identified by the local maxima of the  $DOA_i \times p_\sigma$  plane, rather than by the peaks of the maximum values in each DOA, this drawback would be eliminated. However, like [12, 13], the algorithm would be highly sensitive to reflections or scattering, being useful only in air-to-air engagements.

Consider now a scanning of the radar antenna, that amplitude-modulates pulses, with a circular pattern. In this case, when the antenna sweeps over the radar detector, the PAs gradually increase until a maximum value and then they decrease. The strongest pulses are close in the time domain, as well as in the  $p_\sigma$  axis. Even if a cluster does not comprise every received pulse, it will comprise the strongest pulses in a way that their PRI pattern is preserved within the cluster – and that is what matters to the final deinterleaving step. The other scan patterns

cause the clustering of the strongest pulses to be similar to the circular one, and so they also do not hamper the proposed method in any way.

Yet, the  $DOA_i \times p_\sigma$  plane may drastically reduce the number of operations, when compared to using the whole range of scales  $h$ . A trade-off happens between the demanded computational power and the missing pulses possibility. The technique to be presented prioritizes the computational power saving and keeps the  $DOA_i \times p_\sigma$  plane.

### 4.3 PROPOSED ALGORITHM

Consider a set of pulses distributed in a  $m_\phi \times n_h$ -dimensional array  $A$ , whose elements are  $a_{ij}$ ,  $i = 1, 2, \dots, m_\phi$  and  $j = 1, 2, \dots, n_h$ . The  $m_\phi$  rows  $i$  are related to their measured DOAs, in the discrete  $DOA_i$  domain, and the  $n_h$  columns  $j$  are related to the scale of predicted standard deviations  $p_\sigma$  of their DOA distributions, per their PAs:

$$A = \begin{pmatrix} a_{11} & \cdots & a_{1n_h} \\ \vdots & \ddots & \vdots \\ a_{m_\phi 1} & \cdots & a_{m_\phi n_h} \end{pmatrix} \quad (4.3)$$

The algorithm starts with the scaled moving average technique, which consists of a moving average procedure in each column  $j$  of  $A$ , i.e., in the elements indexed with a specific  $j$ , and  $i = 1, 2, \dots, m_\phi$ , with a moving average window  $w_{MA} \propto j$ :

$$MA(i, j) = \frac{1}{w_{MA}} \sum_{k=0}^{w_{MA}-1} a_{(i-k)j} \quad (4.4)$$

The operations related to (4.4) are executed only in columns that show at least a nonzero element, because the moving average of a column in which all the elements are zero is another column with only zero elements. Then, each column  $j$  of  $MA$ , whose elements are  $ma_{ij}$ , that shows nonzero elements is filtered by a Gaussian vector, at the proper scale  $h_j$ , chosen to match its related predicted standard deviation  $p_\sigma$ , in a way similar to (4.2), now defined as:

$$\mathcal{F}(i, j) = \frac{1}{h_j} \sum_{k=0}^{h_j-1} ma_{(i-k)j} g_{(h_j-k)} \quad (4.5)$$

Following, a  $m_\phi$ -dimensional vector  $\vec{f}$  is generated with the maximum values of each of the  $m_\phi$  rows of  $\mathcal{F}$ . The centers of the clusters are indicated by the peaks of  $\vec{f}$ . Back in  $\mathcal{F}$ , in each row that presents the same index of a peak of  $\vec{f}$ , the column  $j$  that presents the maximum value is searched. This search defines the size of the clusters.

Then, the size of clusters is adjusted by an arbitrary CSAF, since the distributions are not ideal Gaussians. Finally, all the pulses that lie in the range of a cluster are included in it. They are delivered together with the other pulses of the cluster to the final deinterleaving stage. Observe that a pulse can make up more than one cluster.

Frame 4.1 summarizes the steps of the presented DOA-based pulse clustering method.

Frame 4.1 – Summary of the presented pulse clustering technique.

- i. *Load the array  $A$ , containing the pulse distribution according to the measured DOA and  $p_\sigma$ ;*
- ii. *Execute the scaled moving average procedure on the columns of  $A$  that present nonzero elements, generating the array  $MA$ ;*
- iii. *Filter each column of  $MA$  that presents nonzero elements with a Gaussian at the proper scale  $h_j$ ;*
- iv. *Get the maximum values of each row of the filtered  $MA$  array, named  $\mathcal{F}$ , generating a vector  $\vec{f}$ ;*
- v. *Find vector  $\vec{f}$  peaks, defining the center of the clusters;*
- vi. *Find, in each row of  $\mathcal{F}$  that presents the same index of a  $\vec{f}$  peak, the columns in which the maximum happens, thereby defining the size of the clusters;*
- vii. *Adjust the size of clusters by the factor CSAF; and*
- viii. *Deliver together, to the final deinterleaving stage, the pulses that are encompassed together by each cluster.*

Source: own elaboration.



#### 4.4 EXPERIMENTAL SETUP

The validation experiment of the proposed clustering technique, similar to the experiments of sections 2.4 and 3.5, counted on the aid of a prototype of ESM system based on SDR with processing on a tablet device running Matlab™ [34]. A complex scenario was simulated by time-joining, in the same  $DOA_i \times p_\sigma$  plane, pulses received from the USRP B200 in 6 different occasions, all of them specified in Table 4.1:

Table 4.1 – Pulsed signals joined in the  $DOA_i \times p_\sigma$  plane.

Id	$\Phi_{rx}$ (°)	USRP B200 gain (dB)	Number of pulses
S1	30	80	1,444
S2	44	80	1,369
S3	126	71	1,406
S4	126	59	1,399
S5	250	59	1,400
S6	330	80	1,416

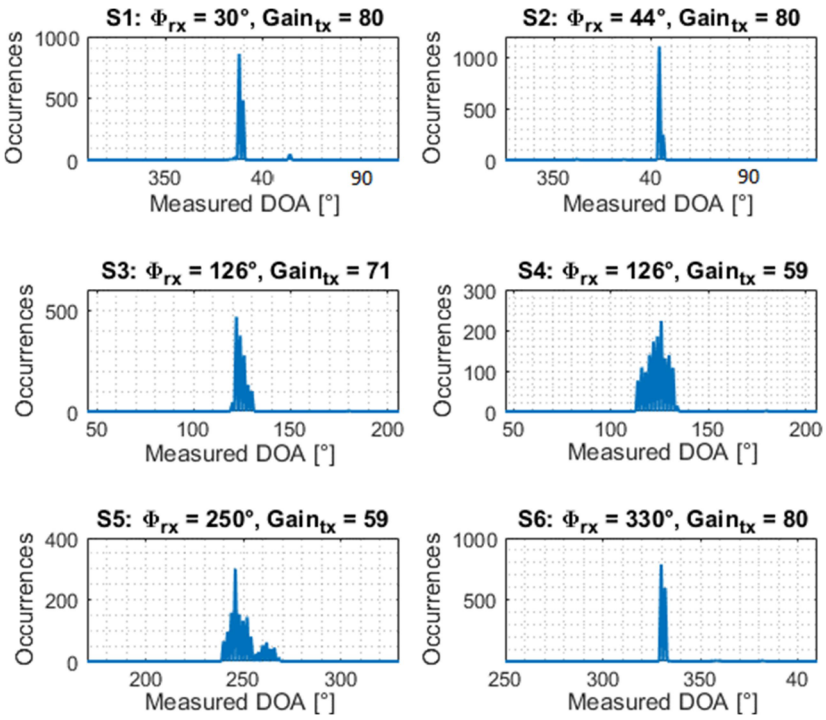
Source: own elaboration.

Fig. 4.7 shows, separately and at different scales, the DOA measurement distributions of each signal of Table 4.1. Observe the following peculiarities that have influenced on the results: the employed DF technique has assigned  $DOA = 54^\circ$  to some pulses of S1; in parallel, it is harder to visualize in the graphs, but the data demonstrate that some pulses of both S3 and S4 had their DOA measured as  $DOA = 180^\circ$ ; lastly, a  $DOA = 358^\circ$  was assigned to some pulses of S6.

The signals S3 and S4 were purposely chosen to verify the relevance of the drawback mentioned on Section 4.2.2. This drawback opposes the need of computational power and it allows, in the filtering procedure, that a distribution with a high predicted standard deviation  $p_\sigma$  hides, from the perspective of the DOA axis, behind another one with a low  $p_\sigma$ . It makes thereby the cluster present a smaller size than it should to encompass all the pulses from both distributions.

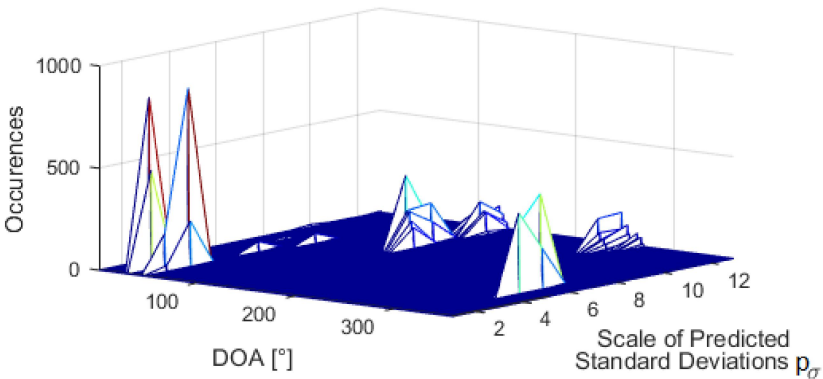
The value of the moving average window  $w_{MA}$  was defined as identical to the column index of the  $p_\sigma$  axis,  $w_{MA} = j$ , in degrees. The scale of predicted standard deviations  $p_\sigma$  was defined from 1 to 13 to match the scales  $h$ , defined from  $h = 3^\circ$  to  $h = 15^\circ$ . The results were obtained with two values for the factor to adjust the size of the cluster:  $CSAF = 1$  and  $CSAF = 2$ . The  $DOA_i \times p_\sigma$  plane is illustrated on Fig. 4.8 with the pulse distributions from S1 to S6.

Fig. 4.7 – DOA histogram of signals of Table 4.1.



Source: own elaboration.

Fig. 4.8 – Complex scenario on the  $DOA_i \times p_\sigma$  plane.

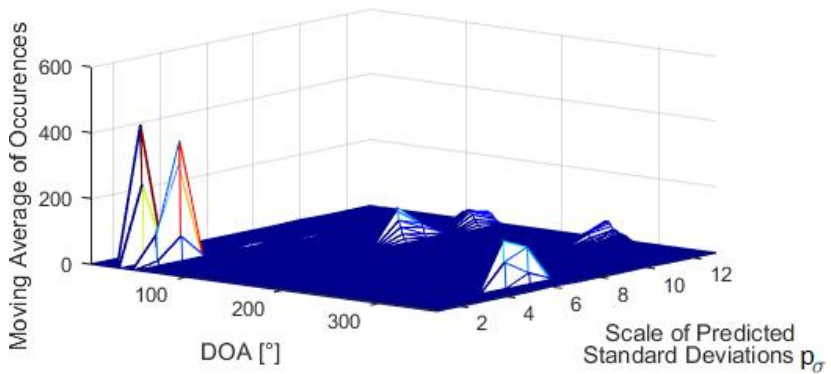


Source: own elaboration.

## 4.5 RESULTS AND DISCUSSION

On the first step of the algorithm, namely, the scaled moving average procedure illustrated on the  $DOA_i \times p_\sigma$  plane of Fig. 4.9, the distributions with high predicted standard deviation  $p_\sigma$  values became smoother than the distributions with low  $p_\sigma$  values. This happens due to the employment, along the  $p_\sigma$  axis, of moving average windows  $w_{MA}$  that are proportional to the  $p_\sigma$  itself.

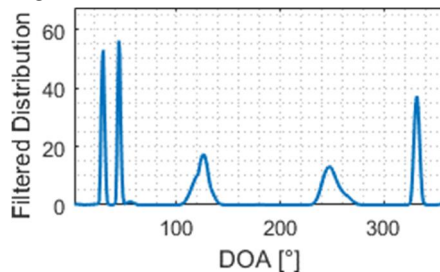
Fig. 4.9 – Scaled moving average of scenario of Fig. 4.8.



Source: own elaboration.

Owing to the diversity of PAs of the incoming pulses, the filtering step occurred at  $n_h = 12$  scaling factors, from  $h = 4^\circ$  to  $h = 15^\circ$ , and only the mathematical operations related to  $h = 3^\circ$  were saved. Fig. 4.10 shows the maximum values, in each DOA, of the filtered distribution, named vector  $\vec{f}$ .

Fig. 4.10 – Gaussian-filtered distribution.



Source: own elaboration.

The peaks of  $\vec{f}$ , in Fig. 4.10, defined the center of 8 clusters, each one centered at the DOAs specified in the second column of Table 4.2, which summarizes the results with a CSAF = 1. Its third column shows in which scale  $h$  of the Gaussians the maximum filtered distribution happened. The number of pulses encompassed by the cluster when CSAF = 1, a case in which the cluster size was defined equal to the Gaussian scale  $h$ , is shown on the fifth column, and the percentage of pulses emitted by the USRP B200 that were comprised by each cluster is shown on the sixth column.

Table 4.2 – Results with CSAF = 1.

Id	DOA (°)	Scale $h$ (°)	Cluster size (°)	Number of pulses	% relative to pulses emitted by B200
C1	30	4	4	1,346	93.21
C2	44	5	5	1,351	98.68
C3	54	10	10	48	-
C4	124	11	11	2,143	76.40
C5	180	14	14	5	-
C6	248	15	15	1,128	80.57
C7	330	7	7	1,389	98.09
C8	358	8	8	18	-

Source: own elaboration.

The sum of the number of pulses in the eight clusters of Table 4.2 results in 7,428, showing that 1,006 (11.93 %) of the 8,434 received and processed pulses stayed out of the clusters.

The clusters C3, C5 and C8 are all related to the DOAs inaccurately measured by the DF algorithm at DOA = 54°, DOA = 180° and DOA = 358°, cited on the second paragraph of Section 4.4.

The cluster C4 encompasses only 76.40 % of the pulses of S3 and S4 together. This low rate confirms the drawback mentioned on Section 4.2.2 and on the third paragraph of Section 4.4, in the  $DOA_i \times p_\sigma$  mapping procedure, of the possibility of a distribution with a high  $p_\sigma$  hiding, from the perspective of the DOA axis, behind another one with a low  $p_\sigma$ .

Besides that, the encompassing rate of pulses of the cluster C6, that deals with a distribution of S5, which is not close to a Gaussian function, is also low (80.57 %).

Table 4.3 shows the results of the experiment with CSAF = 2.

Table 4.3 – Results with CSAF = 2.

Id	DOA (°)	Scale $h$ (°)	Cluster size (°)	Number of pulses	% relative to pulses emitted by B200
C1	30	4	8	1,386	95.98
C2	44	5	10	1,351	98.68
C3	54	10	20	296	-
C4	124	11	22	2,788	99.39
C5	180	14	28	5	-
C6	248	15	30	1,298	92.71
C7	330	7	14	1,389	98.09
C8	358	8	16	18	-

Source: own elaboration.

The sum of pulses contained in the eight clusters is higher (8,531) when CSAF = 2 than when CSAF = 1, as the clusters present wider ranges. This number is higher than the total number of received and processed pulses (8,434). The reason for this is that 97 pulses (1.15 %) were in the range of two clusters, being counted twice.

The cluster C3 reaches pulses concentrated around DOA = 44°, thereby encompassing considerably more pulses than when CSAF = 1. C5 and C8 remain unchanged.

The encompassment rate of C4 rises from 76.40 % to 99.39 %. It shows that the choice of the CSAF value faces the drawback, in the  $DOA_i \times p_\sigma$  mapping procedure, of the possibility of a distribution with a high  $p_\sigma$  hiding, from the prospect of the DOA axis, behind another one with a low  $p_\sigma$ . The rate of C6 increases from 80.57 % to 92.71 %, demonstrating that the CSAF also makes the algorithm robust to distributions that present a certain dissimilarity with Gaussians, in parallel to the robustness provided by the  $DOA_i \times p_\sigma$  plane.

Observe that the change of CSAF from a value of 1 to 2 drastically decreased the missing pulses phenomenon that would happen in the last deinterleaving stage. Despite this advantage of the use of CSAF, its oversize turns the introducing of unique pulses in various clusters into a real problem to the final stage, which demands great computational power to recognize patterns in these cases. The choice of the CSAF, as well as the proportionality factor between the moving average window  $w_{MA}$  and column  $j$  of the  $DOA_i \times p_\sigma$  array, ought to consider the employed receivers and the noise features thereof, which are highly dependent on its type, tunable or wideband.

In both CSAF cases, the filtering has used  $n_h = 12$  scaling factors from the 13 available ones, due to the diversity of PAs of the incoming pulses. Therefore, only a few mathematical operations were saved. That suggests that the saving of operations should not be taken into account on the implementation of the  $DOA_i \times p_\sigma$  plane on radar detectors which are specifically made to operate in electromagnetically dense scenarios. It indicates that only the robustness of the algorithm to distributions that are not close Gaussians and the drawback of the possibility of a distribution hide behind another should be considered.

#### 4.6 FINAL REMARKS OF THE CHAPTER

This chapter presented an algorithm which takes advantage of the reliability of the position of emitters relative to the detector, measured by the DOA parameter. The technique, related to the task (d) of Fig. 1.7., separates pulses in DOA-based clusters, thereby softening the final signal processing stage, namely the interval-only pattern recognition presented on Chapter 5.

A Gaussian filtering procedure was derived from a traditional kernel density estimator that employs the Gaussian basis function. Thereafter, real DOA measurement distributions obtained on Chapter 3 was considered with the aim of improving the performance of the clustering.

The knowledge of the system, in parallel to the availability of the PA of the incoming pulses, allowed the implementation of a  $DOA_i \times p_\sigma$  mapping procedure that may drastically reduce the number of related mathematical operations.

A complex scenario, with 6 distributions of DOA measurements, was processed to verify the proposed method. When the adjusting factor CSAF was equal to 2, the encompassment rates of the clusters were  $\geq 92.71$  %.

## 5 DEINTERLEAVING INSIDE DOA CLUSTERS

The techniques presented so far on this study have considered RF peculiarities to reliably form DOA-based pulse clusters. In a radar detector, the final stage of the radar signal processing is to deinterleave pulses from various radars that may be in the same cluster [2, 7].

This chapter proposes a simple and computationally light interval-only algorithm, related to the task (e) of Fig. 1.10, to conclude the radar signal processing. It suggests changes in the initial steps of the classical technique of Mardia [18] to dispose of its sequence search procedure and save mathematical operations.

In the work of Mardia [18], the exceeding of a weighted threshold by occurrences of bins of cumulative histograms of various orders of differences of sequential TOAs (CDIF) indicates whether possible PRI patterns are present. If a possible PRI is indicated, a sequence search method detects, in the time domain, a sequence of three pulses with the possible PRI, and a projection starts searching pulses from that pattern.

Mardia's method is simple and computationally light, but, with the aim of saving mathematical operations, thereby processing more data, Milojevic and Popovic tried to improve the weighted threshold definition [24], so fewer orders of TOA difference evaluations would be needed. Unfortunately, the proposed threshold definition depends on unknown parameters of the electromagnetic environment, and not only on the parameters of the system, which turns the new method not useful to practical radar detectors. Moreover, the technique keeps the sequence search procedure, which makes it, as well as its predecessor, not robust to clusters that comprise pulses that were measured on data frames that eventually presented a large group of missing samples, cases in which TOA sequences present gaps. Also, in [18, 24], a computationally light definition about the size  $N$  of the frame to be processed is not presented.

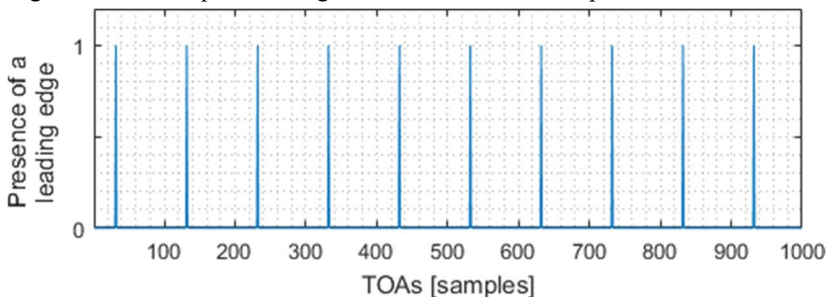
Our proposal consists of small changes in the algorithm of Mardia. It registers in a matrix not only the forward evaluated differences of TOAs that are counted on the CDIF histogram, but also the backward ones, thus avoiding the sequence search procedure. It also presents a simple way of defining the size  $N$  of the frame to be processed, besides a method of precisely estimating PRIs that are not exact multiples of the time  $T_s$  relative one sample of the A/D converter.

Below, the Mardia's method is revisited. Thereafter, the proposed changes are described, and the resulted algorithm is shown in detail. At last, a cluster containing the patterns of  $n_{tx} = 4$  radars is deinterleaved.

## 5.1 CLASSICAL APPROACH

Mardia has suggested an algorithm that combines cumulative histograms of differences of sequential TOAs, denominated CDIF, and sequence search techniques [18]. Consider the TOA of a pulse as the position of its leading edge in the time domain. Fig. 5.1 illustrates, punctually with a value of 1 in the discrete sample time domain, TOAs of a sequence of pulses of a unique radar signal, whose PRI = 100 samples of the radar detector A/D converter.

Fig. 5.1 – Pulse sequence of signal whose PRI = 100 samples.



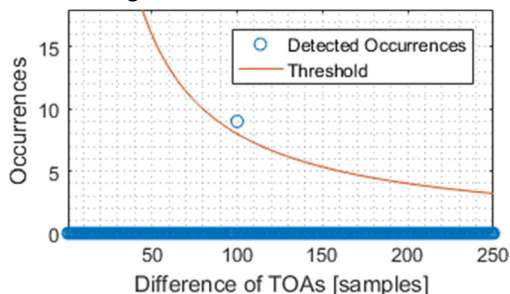
Source: own elaboration.

To achieve the highest possible resolution on the PRI estimation, the CDIF histogram bin-width must be the lowest one possible: 1 sample of the radar detector A/D converter. Fig. 5.2 shows the registering of occurrences of the first forward difference of sequential TOAs – i.e., the difference between each TOA and its first subsequent TOA – of Fig. 5.1. Possible patterns are indicated by the exceeding of a weighted threshold  $WT(diff) = N \times WF/diff$ , consisted of the size  $N$  of the data frame multiplied by a weighting factor  $WF$  over each possible difference of TOAs  $diff$ . In the case of Fig. 5.2, it is possible to discover the PRI pattern, because, in the data frame related to Fig. 5.1, in which  $N = 1000$  samples, ten intervals of 100 samples may happen. The threshold, weighted in this example by a factor  $WF = 0.8$ , is therefore defined as 8 for  $diff = 100$  samples. This threshold is surpassed by the 9 occurrences of the difference of sequential TOAs in the bin  $diff = 100$  samples.

The weighting factor  $WF$  is arbitrarily chosen. A value close to 1 avoids the indication of a true PRI pattern if there are missing pulses, but an excessive decrease of this value may cause the indication of false PRI patterns in complex scenarios.



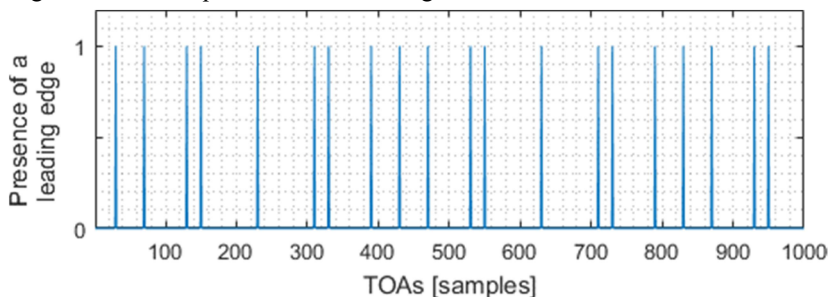
Fig. 5.2 – Histogram of first differences of TOAs of Fig. 5.1.



Source: own elaboration.

Although the simple case of Fig. 5.1 can be easily solved by the first forward differences of sequential TOAs, when more than one PRI pattern is present in the same DOA-based pulse cluster, more steps are necessary. Fig. 5.3 shows the TOAs of a sequence of pulses of two radar signals: one equal to that of Fig. 5.1, presenting  $\text{PRI} = 100$  samples, interleaved with another whose  $\text{PRI} = 80$  samples.

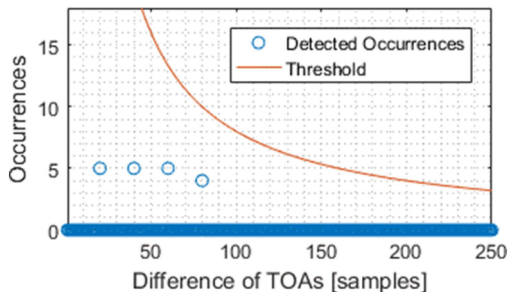
Fig. 5.3 – Pulse sequence of two radar signals.



Source: own elaboration.

Fig. 5.4 illustrates the histogram of the occurrences of the first forward differences of TOAs related to Fig. 5.3. The histogram does not reveal any occurrence in the bin  $\text{diff} = 100$  samples, because the signal whose  $\text{PRI} = 80$  samples does not allow it. Furthermore, it contains only four occurrences in the bin  $\text{diff} = 80$  samples, as the signal whose  $\text{PRI} = 100$  samples recurrently interrupts this pattern.

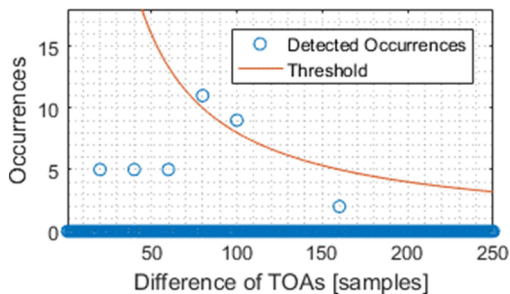
Fig. 5.4 – Histogram of first differences of TOAs of Fig. 5.3.



Source: own elaboration.

In Fig. 5.4, the weighted threshold  $WT(diff)$  is not exceeded by the occurrences of any bin of the histogram, obtained with the first forward differences of sequential TOAs. Thus, the second order of forward differences of sequential TOAs – i.e., the difference between each TOA and its second subsequent TOA – are evaluated, and their occurrences are added to the same histogram of Fig. 5.4, now shown on Fig. 5.5 and treated as a cumulative histogram,  $CDIF(diff)$ .

Fig. 5.5 – CDIF evaluated until the second difference order.

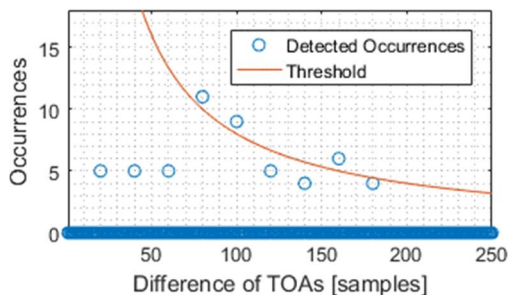


Source: own elaboration.

With the registering of the second order of forward differences of sequential TOAs on the histogram, both bins of  $diff = 80$  samples and  $diff = 100$  samples exceed their own weighted threshold  $WT(diff)$ . However, to avoid false PRI indications that may happen due to the interactions between different patterns, a confirmation is required. Higher orders of the forward differences of sequential TOAs are evaluated not only until the occurrences of a specific bin exceeds its

threshold,  $CDIF(diff) > WT(diff)$ , but also until the occurrences of the bin of its second harmonic does so,  $CDIF(2 \times diff) > WT(diff)$ , or until a pre-determined order of differences, defined by the number of pulses of the cluster. Fig. 5.6 shows the CDIF of the third forward differences.

Fig. 5.6 – CDIF evaluated until the third difference order.



Source: own elaboration.

At first, it seems that the pattern with  $PRI = 80$  samples is indicated, as  $CDIF(80) > WT(80)$  and  $CDIF(160) > WT(160)$ . However,  $CDIF(160) < WT(80)$ . In the illustrated scenario, the threshold conditions are satisfied only on the fourth order of forward differences. In this occasion,  $diff = 80$  samples is declared a possible PRI, and a method called sequence search is initialized. If various bins simultaneously achieve the conditions to enter the sequence search, only the least  $diff$  related to them is declared a possible PRI able to enter it.

On the sequence search, initially, a sequence of three pulses that are separated by intervals equal to the possible PRI is searched. Once the sequence is found, it is taken as reference, and a projection through the whole sample time domain verifies if there are leading edges around positions displaced from multiples of the possible PRI. At the end, the number of detected edges is compared with another threshold. If the sequence search confirms a pattern, the PRI in question is assigned to its pulses, they are deleted from the cluster and the process may start again.

This procedure processes firstly the lower PRI patterns and, once they are recognized, their pulses are deleted from the cluster. As a result, the higher PRI patterns are processed with the absence of those pulses that were interrupting them.

It is possible, in a sequence, for a leading edge to be displaced from its expected location, due to the very common case in which the

incoming pulsed signal PRI is not an exact multiple value of the time  $T_s$  relative to one sample of the radar detector A/D converter. In [18, 24], the authors have not presented a way of estimating the precise PRI of the incoming pulses, with decimal or centesimal specifications. Moreover, natural jitter and measurement inaccuracies of the A/D converter contribute to this phenomenon of displacement of leading edges. Due to these factors, the only way of reliably implementing the sequence search is by a self-adjusting loop that continuously corrects the projection of the possible PRI along the whole frame of data, respecting a tolerance of samples. Still, if a frame eventually presents a large group of missing samples, the sequence may break and the procedure may fail.

At last, neither Mardia nor Milojevic and Popovic presented a computationally light solution to the issue about the size of the frame to be processed. For instance, consider that a DOA-based pulse cluster presents pulses emitted by two radars, but, due to their radar antenna scans, one pattern begins and ends before the other inside the cluster, and there is only a time-intersection between them. If the whole data frame relative to all the pulses contained in the cluster is considered, the weighted threshold  $WT(diff) = N \times WF/diff$  will be unachievable for both patterns, as the size  $N$  of the data frame will be oversized. The methods of both [18, 24] divide the cluster in smaller pieces in the time domain and process independently each one of them. The processing of a piece does not influence on the processing of another piece.

## 5.2 PROPOSED CHANGES

### 5.2.1 Suppression of the sequence search procedure

In the proposal of Mardia [18], after the CDIF histograms are formed, the data related to the various orders of the forward differences of sequential TOAs are discarded. Once both the occurrences of a bin  $CDIF(diff)$  and  $CDIF(2 \times diff)$  exceed the threshold  $WT(diff)$ , the sequence search begins, which, in resume, consists in a verification, in the time domain, if there exist other pulses located at distances near the possible PRI after and before each pulse.

Given that the forward differences of sequential TOAs at various orders are evaluated in the initial steps of the algorithm, the information about the existence of pulses at a distance near the possible PRI after other pulses was already evaluated in the occasion of the satisfaction of the weighted threshold conditions. The missing information is only about the existence of pulses at a distance near the possible PRI before

other pulses. This information can be raised by verifying if pulses are registered as being located near the possible PRI after another pulse. Another possibility is to evaluate, in the initial steps, in parallel to the forward differences of sequential TOAs, at the same orders, the backward differences of sequential TOAs – that is, the difference between each TOA and its precedent TOAs. Two matrixes containing the forward and backward differences of sequential TOAs related to each pulse are registered in the formation of the CDIF.

Now, when a possible PRI is indicated by the satisfaction of the weighted threshold conditions, all the pulses containing values close to the possible PRI in the forward and backward differences of sequential TOAs matrixes are marked as being part of the sequence. To prevent pulses from wrongly being marked due to the interactions of patterns, the second harmonic of the possible PRI is also checked in both the forward and the backward differences relative to each pulse. It is not necessary to count how many pulses are a part of the sequence: this calculation is already done in the formation of the CDIF histogram.

This procedure not only substitutes the self-adjusting loop of the sequence search, but it also provides robustness in front of the possibility of the cluster have been generated by a frame eventually presented a large group of missing samples.

### 5.2.2 Precise PRI estimation

Disregard, at this moment, the natural jitter and measurement inaccuracies of the A/D converter. The CDIF histogram bin-width of 1 sample causes signals that present simple PRIs that are not exact multiple values of the sample time  $T_s$  to have their counts spread between two bins. A moving average, with window size equal to 2 samples, is necessary to avoid that this spread makes the threshold not be reached by a bin. After a bin  $diff'_k$  of the moving averaged  $CDIF'$  histogram exceeds the weighted threshold, the precise  $PRI$  can be estimated by its expectation  $E'$ , obtained through the weighted average:

$$E'(PRI) = \frac{diff'_k CDIF'(diff'_k) + diff'_{k-1} CDIF'(diff'_{k-1})}{CDIF'(diff'_k) + CDIF'(diff'_{k-1})} \quad (5.1)$$

By computing the natural jitter and measurement inaccuracies of the A/D converter, the moving average window is increased according to the behaviour of the system in front of these phenomena, and extra terms around the  $diff'_k$  are inserted on (5.1).

### 5.2.3 Definition of the size of the frame to be processed

Regarding the size of the frame to be processed, this work proposes that, firstly, the algorithm runs over the entire frame related to the first TOA until the last TOA contained in the whole DOA-based cluster, no matter the period related to it. Ordinarily, the backward and forward differences of TOAs related to each of the pulses of the whole cluster are registered. If the weighted threshold conditions related to the whole DOA-based cluster are satisfied by some bin of the CDIF histogram (fundamental and second harmonic), the forward and backward differences of TOAs of each pulse are verified. Those pulses presenting differences close to the possible PRI and its second harmonic have their PRI assigned. Then, these pulses are excluded from the DOA-based cluster and the process may start again without them.

If the weighted threshold conditions related to the whole DOA-based cluster are not satisfied by any bin of the CDIF histogram until a pre-defined maximum order of differences, defined by the number of present pulses, the cluster is divided in small subclusters, according to its inner time-density of pulses. A kernel density estimator, like the one described by (4.1) in Chapter 4, but now in the sample time domain, indicates concentrations of pulses. A comparison of variations of the kernel density estimate indicates the begin and the end of each time-density-based subcluster. This comparison is such as that made on the pulse measurement algorithm, in Chapter 2. It includes the moving average step described there.

The time-length  $N_j$  of the subcluster  $j$  defines its new threshold function  $WT_j(diff) = N_j \times WF/diff$ . A  $CDIF_j(diff)$  histogram is generated for the subcluster  $j$ . It is verified by the new weighted threshold  $WT_j(diff)$ , always respecting a maximum order of differences of TOAs, which is defined by its number of pulses present.

At any moment, if a  $CDIF_j(diff) > WT_j(diff)$  and  $CDIF_j(2 \times diff) > WT_j(diff)$ , not only the pulses of the subcluster  $j$  have their forward and backward differences of TOAs verified, but all the pulses of the entire DOA-based cluster have it. The detected PRI is assigned to all of them. All these pulses are excluded from the whole cluster – and from every subcluster as well. Following, the algorithm may begin again evaluating the first order of differences of sequential TOAs and mounting the  $CDIF_j(diff)$  histogram from that time-density-based subcluster  $j$ . Now, however, the already PRI-assigned pulses are

absence. The algorithm stops when there is a minimum number of pulses left in the DOA-based cluster.

#### 5.2.4 Extra threshold condition

The procedure presented in Section 5.2.3 allows, in a computationally light way, the processing of received data related to large periods. This is possible due to a method that identifies small time-density-based subclusters, related to patterns that begin and end within the DOA-based cluster.

However, if a pattern that occurs in a large period is interrupted by pulses of various shorter patterns, the interrupted pattern needs the evaluation of high orders of differences of sequential TOAs until its threshold conditions can be satisfied. In this occasion, the occurrences in the bins of the harmonics of the PRI of the interrupted pattern may become close to the occurrences of the bin of the fundamental. Then, before the occurrences of the bin of the fundamental exceed the threshold, it happens the threshold exceeding by the occurrences of the bins of the related second and fourth harmonics – since their thresholds are divided by 2 and by 4, in relation to that of the fundamental. In this case, the second harmonic is falsely indicated as a possible PRI.

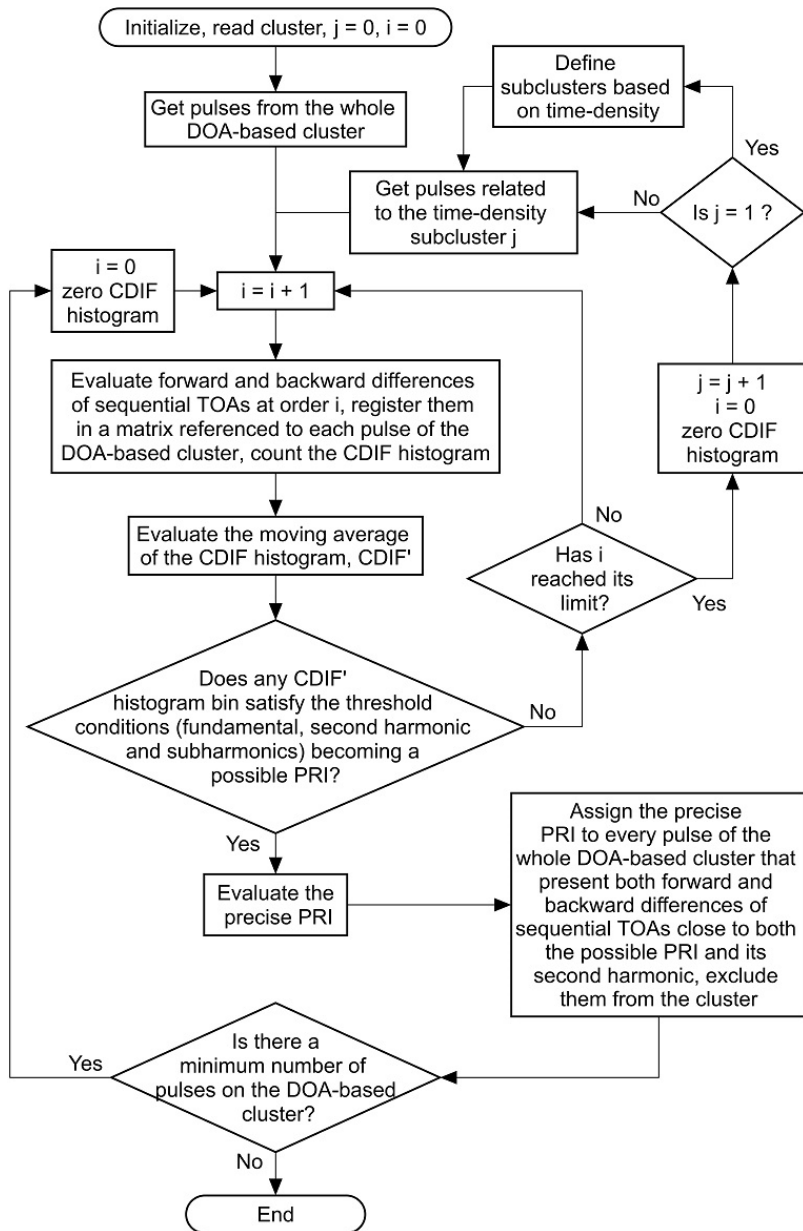
Due to this possibility, it is necessary to introduce a new threshold condition in the algorithm: whenever the occurrences of a bin of a specific  $diff$  exceeds the weighted threshold, the bins of its first three subharmonics ( $diff/2$ ,  $diff/3$  and  $diff/4$ ) are verified, and the occurrences in each one of them may not be higher than those of the bin related to  $diff$  itself.

The final algorithm threshold conditions can be resumed so as:

- a) the occurrences of a bin related to a specific  $diff$  exceed the threshold related to it,  $CDIF(diff) > WT(diff)$ ;
- b) the occurrences of the bin  $2 \times diff$  exceed the threshold related to  $diff$ ,  $CDIF(2 \times diff) > WT(diff)$ ; and
- c) the occurrences of the bins related to  $diff/2$ ,  $diff/3$  and  $diff/4$  may not be higher than those related to  $diff$ ,  $CDIF(diff/i) < CDIF(diff)$ ,  $i = 2, 3, 4$ .

Fig. 5.7 shows the flowchart that represents the final presented algorithm.

Fig. 5.7 – Proposed algorithm flowchart.



Source: own elaboration.



### 5.3 VALIDATION

The proposed algorithm was implemented in Matlab™ [34]. A DOA-based cluster containing signals from  $n_{tx} = 4$  radars was simulated as if it were the data acquisition of 4 frames of the ESM system prototype based on the NooElec RTL-SDR [28]. It was simulated that the RTL-SDR was operating with a sampling rate of  $f_s = 2.4$  MS/s, and that each frame had size of  $N = 65,536$  samples, which totalizes a receiving period of 109.2 ms. The large period of 4 frames of the RTL-SDR was considered due to the need of synchronization of the system on real operations [3], as mentioned in Section 1.2.

On realistic scenarios, different functions of radar antenna gain  $G_{tx}(\theta_{tx}, \Phi_{tx})$  and different scan patterns amplitude-modulate signals. Hence, pulses of some radars may be undetected in relevant periods of the processing. This peculiarity was also simulated, thereby testing the method described in Section 5.2.3, concerning a computationally light definition of the frame size to be handled by the interval-only algorithm.

Table 5.1 summarizes, in view of the above described parameters of the RTL-SDR, the  $n_{tx} = 4$  simulated pulsed signals, R1-R4, considering a different radar antenna scan pattern to each one.

Table 5.1 – Pulsed signals in the same DOA-based cluster.

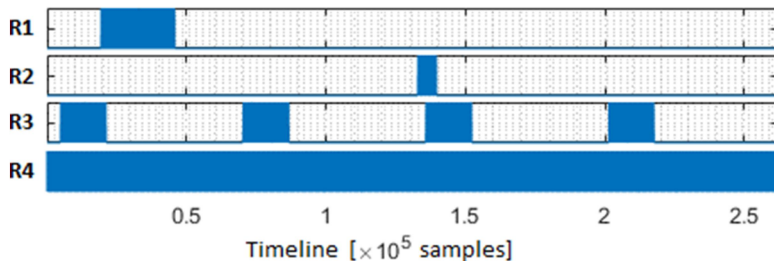
Id	Scan pattern	Illumination period (ms)	PRI ( $\mu$ s)	PRI (samples)	Number of pulses
R1	circular	8.1 - 19.2	254.5	610.9000	44
R2	sector	55.4 - 58.2	104.5	250.8000	27
R3	lobe switching	2.0 - 8.8	48	115.2000	566
		29.3 - 36.1			
		56.6 - 63.4			
		83.9 - 90.7			
R4	lock on	0 - 109.2	200	480.0000	547

Source: own elaboration.

The third column of Table 5.1 refers to the radar antenna scan pattern issue. It is related to periods in which the PAs are sufficient to the detection of pulses, allowing a TOA to be measured. The fourth column shows the signal PRIs, in  $\mu$ s, and the fifth one shows the same parameter, but related to the sample time  $T_s$  of the RTL-SDR. Observe that the PRIs of R1-R3 are not exact multiple values of  $T_s$ , so the precise PRI estimation, obtained with (5.1), can be verified.

The distribution, in the sample time domain, of the signals of Table 5.1 is illustrated in Fig. 5.8.

Fig. 5.8 – Timeline of R1-R4 signals inside cluster.

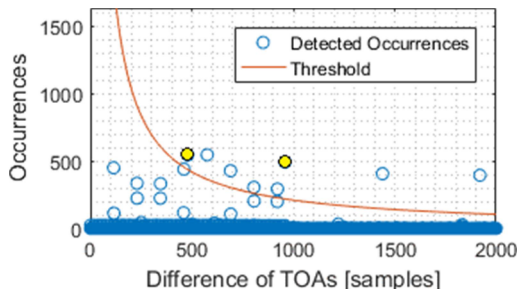


Source: own elaboration.

The threshold factor was defined as  $WF = 0.8$ . The maximum order of differences of sequential TOAs, to the whole DOA-based cluster and to the time-density-based subclusters, was defined as 20 or as the number of pulses into the cluster/subcluster divided by 5, the least of them. The  $CDIF'$  histogram moving average window was equal to 2. The kernel density estimator scale was defined as 5,000 samples, and the moving average window of its variations was 200 samples.

Firstly, on the processing of the whole DOA-based cluster, the algorithm evaluated the differences of sequential TOAs and their related CDIF until the order 10, when the occurrences  $CDIF(480)$  and  $CDIF(960)$  exceeded the weighted threshold  $WT(480)$ , indicating a pattern with  $PRI = 480$  samples, related to the signal R4. Fig. 5.9 shows the CDIF histogram of that occasion, with the mentioned occurrences highlighted.

Fig. 5.9 – CDIF evaluated until the tenth difference order.



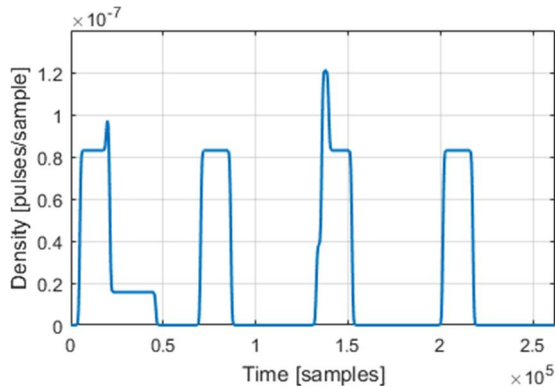
Source: own elaboration.

On the above processing, the couple  $CDIF(960)$  and  $CDIF(1920)$  exceeded  $WT(960)$  before the evaluation of the tenth order of differences of sequential TOAs. This happened because the pattern of R4 is interrupted various times along the time-line shown on Fig. 5.8 by the pulses of R1-R3. It was the extra threshold condition detailed on Section 5.2.4 that contributed to prevent that a pattern with  $PRI = 960$  samples were falsely indicated.

After the correct exclusion of the pulses which presented differences of TOAs close to both 480 and 960 samples in both the forward and the backward differences of TOAs matrixes, the processing of the whole DOA-based cluster began again, and the differences of sequential TOAs and their related CDIF were evaluated until the maximum pre-determined order of 20, with no more patterns indicated.

In this way, the algorithm entered in the procedure described in Section 5.2.3. The kernel density estimator was used as described by (4.1) in Chapter 4, but in the sample time domain, to define the time-density-based subclusters. Fig. 5.10 illustrates the evaluated density estimate. This figure can be faced to Fig. 5.8. Notice that the pulses of R4 were already deleted from the DOA-based cluster.

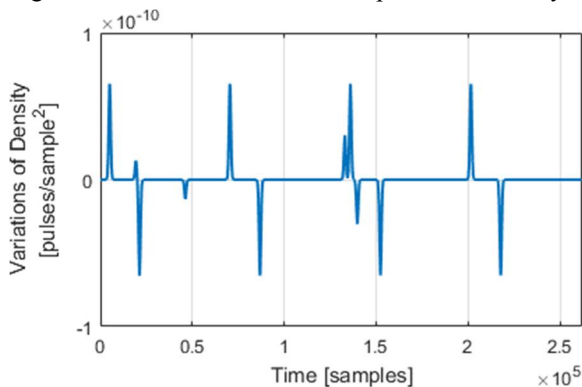
Fig. 5.10 – Estimate of the time-density of pulses.



Source: own elaboration.

The variations related to the density estimate illustrated on Fig. 5.10 are illustrated on Fig. 5.11. Similar to the procedure of the pulse measurement algorithm presented on Chapter 2, the local peaks of the moving average of the density variations characterize begins and ends of the subclusters.

Fig. 5.11 – Variations related to the pulse time-density estimate.



Source: own elaboration.

Table 5.2 summarizes the identified time-density-based subclusters. Observe that 6 subclusters are indicated, due to the scan pattern of R3 and to the absence of the pulses of R4. The scanning of R3 causes 4 concentrations of pulses. The pulses of R4 occupied the whole DOA-based cluster and, at this stage, was already deleted.

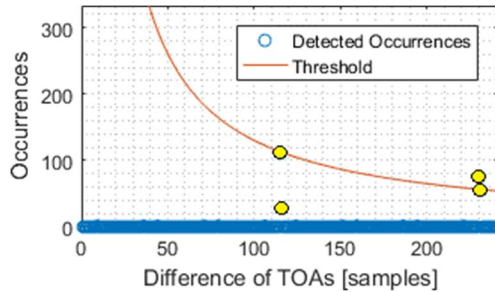
Table 5.2 – Detected time-density-based subclusters.

Id	begin (samples)	begin (ms)	end (samples)	end (ms)
SC1	4,856	2.0	21,104	8.8
SC2	19,016	7.9	46,016	19.2
SC3	70,288	29.3	86,648	36.1
SC4	132,832	55.3	139,608	58.2
SC5	135,840	56.6	152,200	63.4
SC6	201,392	83.9	217,632	90.7

Source: own elaboration.

On the processing of the subcluster SC1, only two orders of differences of sequential TOAs were needed so the threshold conditions were satisfied. Fig. 5.12 shows the related CDIF histogram. It seems that the threshold conditions are not satisfied, as  $CDIF(115) < WT(115)$ ,  $CDIF(116) < WT(116)$ ,  $CDIF(230) < WT(115)$  and, finally,  $CDIF(231) < WT(116)$ . Observe that a moving average procedure, in which the window size is equal to 2 samples, compute together the occurrences in both  $diff = 115$  samples and  $diff = 116$  samples, and

Fig. 5.12 – CDIF of subcluster SC1, until the second order.



Source: own elaboration.

also those in both the  $diff = 230$  samples and  $diff = 231$  samples, resulting in a  $CDIF'$  moving averaged histogram.

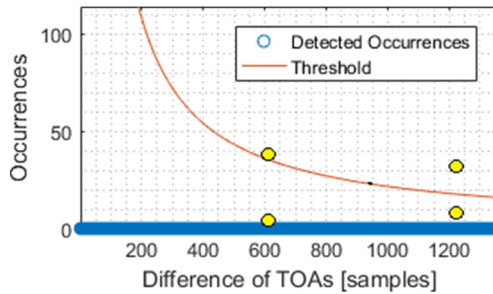
The estimation of the precise PRI using (5.1) in the data related to the case of Fig. 5.12, with 4 digits after the decimal point, was evaluated as  $E'(PRI) = 115.2014$  samples, a value close to the PRI of R3. This was the PRI value assigned to the pulses related to the pattern.

When the pattern of SC1 was recognized as presenting a  $PRI = 115.2014$ , the backward and forward differences of sequential TOAs matrixes related to all the pulses of the whole DOA-based cluster were verified. All the pulses presenting values close to both  $115.2014$  and  $2 \times 115.2014$  in both matrixes had their PRI-assigned as  $115.2014$ . Thereafter, they were excluded from the whole DOA-based cluster, becoming also absent from the time-density-based subclusters SC3, SC5 and SC6, as they were a part thereof.

The processing of the subcluster SC2 was similar to its predecessor, SC1, diverging from it only by the fact that it did not cause pulses from other subclusters to be identified as being part of the same pattern. The processing also benefited from the moving average procedure, and the precise PRI was estimated as  $E'(PRI) = 610.9048$  samples, close to the PRI of R1. Fig. 5.13 illustrates the related CDIF histogram, that were mounted with differences of TOAs until the second order.

The SC3 processing consisted of only a verification that the subcluster had zero pulses, and then the maximum order of differences of sequential TOAs was also defined as zero. Therefore, no evaluation was made, and the algorithm skipped to the next subcluster, saving computational power.

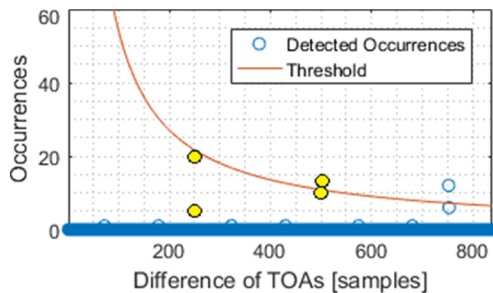
Fig. 5.13 – CDIF of subcluster SC2, until the second order.



Source: own elaboration.

The SC4 processing occurred up to the third order of differences of sequential TOAs, and its precise PRI was estimated as  $E'(PRI) = 250.8000$ . Fig. 5.14 shows the related CDIF histogram.

Fig. 5.14 – CDIF of subcluster SC4, until the third order.



Source: own elaboration.

The processing of the subclusters SC5 and SC6 did not happen, due to the fact that in the end of the processing of the subcluster SC4 there was not a sufficient amount of pulses in the DOA-based cluster to characterize a pattern.

Table 5.3 summarizes the results of the above described processing by showing the variations of the evaluated precise PRIs in front of the true PRIs of R1-R4. It also shows, for each signal, the number of pulses that had their PRI correctly assigned.

Table 5.3 – Results of the interval-only technique.

Id	Measured PRI (samples)	Variation relative to original (%)	Correct-PRI assigned pulses	% relative to original
R1	610.9048	$7.8 \times 10^{-6}$	43	97.73
R2	250.8000	0	26	96.30
R3	115.2014	$1.2 \times 10^{-5}$	559	98.76
R4	480.0000	0	547	100

Source: own elaboration.

The third column of Table 5.3 shows that the precise PRI estimation technique provides PRI measurements with errors of the order of  $10^{-5}$ . Also, the rates of correct-PRI assigned pulses contained on its fifth column demonstrate that the substitution of the sequence search procedure by the forward and backward matrixes did not jeopardize the performance of the method.

The interval-only techniques presented on this chapter allow the discovering and the deinterleaving of PRI patterns within DOA-based clusters of pulses.

Once radar signals are completely deinterleaved from one another, their parameters can be compared with a pre-registered database to finally identify each one of them.

#### 5.4 FINAL REMARKS OF THE CHAPTER

This chapter was related to the task (e) of Fig. 1.7. It presented a simple and computationally light interval-only algorithm to conclude the radar signal processing in a radar detector, recognizing PRI patterns inside the DOA-clusters available after the accomplishment of the task (d) Fig. 1.7.

The method is based on the Mardia's classical technique [18]. It has changed the initial steps of the algorithm proposed in [18], registering in a matrix not only the forward evaluated differences of TOAs that are counted on the CDIF histogram, but also the backward ones. This maneuver enabled the avoidance of the sequence search procedure is avoided and the saving of mathematical operations.

Also, a simple way of defining the size of the frame to be processed, and a method of precisely estimating PRIs that are not exact multiples of the time  $T_s$  relative to the sample of the A/D converter were presented.

At last, a DOA-based cluster containing  $n_{tx} = 4$  patterns was deinterleaved as an example. Results showed that the precise PRI can be estimated with an error of the order of  $10^{-5}$ , and at least 96.30 % of the pulses of the patterns had their PRI correctly assigned.



## 6 CONCLUSIONS

Radars emerged in the 20th century as an innovative way of electronic sensing. They resulted from interactions between technology and military philosophy.

Nowadays, they feature as an indispensable utility. Their applications are becoming increasingly common, varying in different complexities, and the capability to locate and identify them provides lots of advantages, in both civilian and military contexts.

However, the complexity to process radar signals makes the design of radar detectors very challenging. In a modern scenario, before discriminating radar signals, detectors must deinterleave the signal resulted from the superposition of signals received from many emitters, which can be positioned, each one, at a different direction and distance. In parallel, the modern world frequently requires characteristics of low volume, weight and costs on its electronic equipment.

From these issues, the research questions stated on Section 1.2 have arisen. These questions are about the way of designing radars with restricted resources and the possibility of doing it with low volume, weight, costs and processing capabilities.

To face the requirements imposed by the research questions, this work aimed at proposing signal processing techniques that considers RF peculiarities to soften the processing workload and to allow the design of radar detectors which present low volume, weight, costs and available computational power.

First, in Chapter 1, the problem related to this research was introduced and modelled. The necessary tasks to accomplish the related radar signal processing were summarized in Fig. 1.10.

A pulse measurement technique that can process pulses which are superimposed in the time domain, thereby contributing to diminish the missing pulses phenomenon was presented on Chapter 2. The proposed method, related to tasks (a) and (b) of Fig. 1.10, differs from conventional ones as it focuses on the variations of the resulting amplitude envelopes of signals. An experiment implemented on an SDR-based ESM system showed that the performance of the proposed algorithm degrades only when the amplitude envelopes are lower than 3.7 mV on the input of the used SDR.

A DF technique that pushes the number of employed channels  $n_{ch}$  that are necessary to reliably measure the DOA parameter to its inferior limit was presented on Chapter 3. This method, related to the

task (c) of Fig. 1.10, contributes to save mathematical operations related to measuring pulses in lots of channels. It also contributes to save the volume, weight and costs related to the channels themselves. The method is not restricted to the main lobe zone of the antennae of the radar detector, allowing each antenna to cover a larger angular sector than they would do in conventional analytical methods. The real pattern of each antenna and the PAs of each single pulse found in every channel are considered and compared with a pre-registered matrix of relation of PAs, using a weighted Euclidean distance evaluation. Experiments with the same prototype of SDR-based ESM system used on Chapter 2 showed that the DOA measurements of the method present distributions with Gaussian features, with a standard deviation  $\sigma$  as high as the lower the SNR.

Taking advantage of the reliability of the position of the emitter relative to the detector, a DOA-based pulse clustering technique was introduced on Chapter 4. The clustering method, related to the task (d) of Fig. 1.10, uses a parametric Gaussian filtering procedure. It benefits from the fact that the knowledge of the PA parameter of the incoming pulses allows the prediction of the standard deviation  $\sigma$  of their distributions, since the features of the system and the behaviour of the employed DF technique are previously known. A complex scenario with 6 distributions of DOA measurements was processed, and, when the adjusting factor CSAF = 2, the encompassment rates of the clusters were  $\geq 92.71$  %.

At last, an interval-only method was derived, in Chapter 5, from the classical technique of Mardia [18], to recognize PRI patterns inside the DOA-clusters. The proposed algorithm, related to the task (e) of Fig. 1.10, changes the initial steps of the algorithm proposed in [18], registering in a matrix not only the forward evaluated differences of TOAs that are counted on the CDIF histogram, but also the backward ones, so the sequence search procedure is avoided and mathematical operations are saved. The chapter also presented a simple way of defining the size of the frame to be processed, and a method of precisely estimating PRIs that are not exact multiples of the time  $T_s$  relative to the sample of the A/D converter. Results showed that the precise PRI can be estimated with an error of the order of  $10^{-5}$ , and at least 96.30 % of the pulses of the patterns had their PRI correctly assigned.

The methods introduced on this research allow that radar signals be fully deinterleaved from one another. Every step of the algorithms, as well as the whole of the work, was designed to be computationally light.

The proposed methods answer the research question (a) of Section 1.2, as they describe the way of designing radar detectors with restricted resources. This dissertation as a whole shows that it is possible to do that with features of low volume, weight, costs and processing capabilities, thereby answering the research question (b) of Section 1.2.

Aligned with these features, on a future work, the pulse and DOA measurement algorithms, respectively presented on chapters 2 and 3, may be implemented on field programable gate arrays (FPGA). In parallel, the pulse clustering technique and the interval-only pattern recognition method, respectively described on chapters 4 and 5, may be implemented on a Raspberry Pi [46]. Regarding the technological tendencies of today, another future work would be to embed the whole system on a drone and share the information about the surrounding radars via Internet of Things (IoT).



## REFERENCES

- [1] SKOLNIK, M. **Radar handbook**. 3<sup>rd</sup> edition. New York: McGraw-Hill Education, 2008.
- [2] WILEY, R. **Electronic intelligence: the interception and analysis of radar signals**. Boston: Artech House Inc, 2006.
- [3] SEUTÉ, H. *et al.* Why synchronization is a key issue in modern Electronic Support Measures. In: INTERNATIONAL RADAR SYMPOSIUM (IRS), 16., 2016, Dresden. *Anais...* New York: IEEE, ago. 2015, p. 794-799.
- [4] TUNCER, T. E.; FRIEDLANDER, B. **Classical and modern direction-of-arrival estimation**. Burlington: Academic Press Inc., 2009.
- [5] RAZAVI, B. **RF Microelectronics**. 2nd edition. Upper Saddle River: Prentice Hall, 2011.
- [6] STUTZMAN, W. L.; THIELE, G. A. **Antenna theory and design**. 3rd edition. New York: John Wiley & Sons Inc, 2012.
- [7] NERI, F. **Introduction to electronic defense systems**. Raleigh: SciTech Publishing Inc., 2006.
- [8] LASSER, G.; FILIPOVIC, D. A wide-band spiral based amplitude-only azimuth direction finding system. In: IEEE INTERNATIONAL SYMPOSIUM ON ANTENNAE AND PROPAGATION (APSURSI), 54., 2016, Fajardo. *Anais...* New York: IEEE, out. 2016, p. 1823-1824.
- [9] AHMAD, A.; AYENI, J.; KAMAL, S. Determination of the pulse repetition interval (PRI) agility of an incoming radar emitter signal using instantaneous power analysis. In: AFRICON, 10., 2015, Addis Ababa. *Anais...* New York: IEEE, nov. 2015, p. 1-4.
- [10] GENÇOL, K.; KARA, A.; AT, N. New wavelet-based features for the recognition of jittered and stagger PRI modulation types. In: SIGNAL PROCESSING AND COMMUNICATIONS APPLICATIONS CONFERENCE (SIU), 23., 2015, Malatya. *Anais...* New York: IEEE, jun. 2015, p. 2134-2137.

- [11] GENÇOL, K.; KARA, A.; AT, N. A wavelet-based feature set for recognizing pulse repetition interval modulation patterns. **Turkish Journal of Electrical Engineering & Computer Sciences**, v. 24, p. 3078-3090, 2015.
- [12] Y. H. KIM *et al.* Radar scan pattern analysis for reduction of false identification in electronic warfare support systems. **IET Radar, Sonar & Navigation**, v. 8, n. 7, p. 719-728, ago. 2014.
- [13] GREER, T.H. **Automatic recognition of radar scan type**. United States patent US 6 697 007, out. 2004.
- [14] GENÇOL, K.; KARA, A.; AT, N. Improvements on deinterleaving of radar pulses in dynamically varying signal environments. **Digital Signal Processing Magazine**, v. 69, p. 86-93, 2017.
- [15] LIU, Y.; CUI, H. A novel self-adaptive density-based clustering algorithm for radar signal sorting. In: IET INTERNATIONAL RADAR CONFERENCE, 19., 2015, Hangzhou. *Anais...* New York: IEEE, abr. 2016, p. 1-7.
- [16] YANG, Q. *et al.* A sorting algorithm based on adaptive density threshold for unknown radar signals. **Electronic Information Warfare Technology**, v. 27, n. 1, p. 16-19, 2012.
- [17] SHENG, Y.; HOU, C.; SI, W. Extract pulse clustering in radar signal sorting. In: INTERNATIONAL APPLIED COMPUTATIONAL ELECTROMAGNETICS SOCIETY SYMPOSIUM (ACES), 3., 2017, Florença. *Anais...* New York: IEEE, maio 2017, p. 1-2.
- [18] MARDIA, H. K. New techniques for the deinterleaving of repetitive sequences. **IEE Proceedings F - Radar and Signal Processing**, v. 136, n. 4, p. 149-154, ago. 1989.
- [19] MELLO, R. G. L.; JUNQUEIRA, C. C. M. Polarization diversity on ESM systems. **Journal of Microwaves, Optoelectronics and Electromagnetic Applications**, São Paulo, v. 16, p. 273-283, 2017.
- [20] MELLO, R. G. L.; ROSO, N. A.; SOUSA, F. R.; JUNQUEIRA, C. C. M.; CHINATTO, A. Proposta de um MAGE RDS com processamento em tablet: desafios de hoje e perspectivas do amanhã. **Revista Spectrum**, Brasília, v. 1, p. 17-22, 2016.

- [21] MELLO, R. G. L.; SOUSA, F. R.; JUNQUEIRA, C. C. M. SDR-Based radar-detectors embedded on tablet devices. In: SBMO/IEEE MTT-S INTERNATIONAL MICROWAVE AND OPTOELECTRONICS CONFERENCE (IMOC), 12., 2017, Águas de Lindoia. *Anais...* New York: IEEE, dez. 2017, p. 1-5.
- [22] MELLO, R. G. L.; SOUSA, F. R.; JUNQUEIRA, C. C. M.; CHINATTO, A. Demonstrador de um sistema MAGE com a antena do P-95 e processamento em tablet. In: SIMPÓSIO DE APLICAÇÕES OPERACIONAIS EM ÁREAS DE DEFESA (SIGE), 19., 2017, São José dos Campos. *Anais...*
- [23] MELLO, R. G. L.; SOUSA, F. R. Precise techniques to detect superimposed radar pulses on ESM systems. **IET Radar, Sonar & Navigation**, 2018.
- [24] MILOJEVIC, D. J.; POPOVIC, B. M. Improved algorithm for the deinterleaving of radar pulses. **IEE Proceedings F - Radar and Signal Processing**, v. 139, n. 1, p. 98-104, Feb. 1992.
- [25] MA, S. *et al.* Pulse Sorting Algorithm Using TDOA in Multiple Sensors System. **Advanced Materials Research**, v. 571, p. 665-670, 2012.
- [26] POTTER, C.; BULLOCK, A. Nonlinearity correction of microwave diode detectors using a repeatable attenuation step. **Microwave Journal**, v. 36, p. 272, 1993.
- [27] KENT ELECTRONICS. Printed circuit board (PCB) antennas, 2018. Disponível em: <<http://www.wa5vjb.com/>>. Acesso em: 25 maio 2018.
- [28] NOOELEC INC. About RTL-SDR, 2018. Disponível em: <<http://www.rtl-sdr.com/about-rtl-sdr>>. Acesso em: 25 maio 2018.
- [29] MICROSOFT. Surface Pro 4, 2018. Disponível em: <<http://www.microsoft.com/en-us/surface/devices/surface-pro-4/overview>>. Acesso em: 25 maio 2018.
- [30] FALLEN, C. *et al.* GPU performance comparison for accelerated radar data processing. In: SYMPOSIUM ON APPLICATION ACCELERATORS IN HIGH-PERFORMANCE COMPUTING, 1., 2011, Knoxville. *Anais...* New York: IEEE, set. 2011, p. 84-92.

- [31] GAO, J.; WANG, J.; LAI, Z. GPU-accelerated mismatched filter for analog TV-based passive radar. In: CIE INTERNATIONAL CONFERENCE ON RADAR (RADAR), 11., 2016, Guangzhou. *Anais...* New York: IEEE, out. 2017, p. 1-5.
- [32] RUPNIEWSKI, M. *et al.* A real-time embedded heterogeneous GPU/FPGA parallel system for radar signal processing. In: INTL IEEE CONFERENCES ON UIC/ATC/SCALCOM/CBDCOM/IOP/SMARTWORLD, 7., 2016, Toulouse. *Anais...* New York: IEEE, jan. 2017, p. 1189-1197.
- [33] ZHANG, C.; YANG, Q.; DENG, W. High frequency radar signal processing based on the parallel technique. In: IET INTERNATIONAL RADAR CONFERENCE, 19., 2015, Hangzhou. *Anais...* New York: IEEE, abr. 2016, p. 1-4.
- [34] THE MATHWORKS INC. Matlab R2017a, 2018. Disponível em: <<http://www.mathworks.com>>. Acesso em: 25 maio 2018.
- [35] ETTUS RESEARCH. USRP B200, 2018. Disponível em: <<http://www.ettus.com>>. Acesso em: 25 maio 2018.
- [36] THANH, H. T.; HA, T. N.; VAN YEM, V. Novel direction finding algorithm based on phase locked loop with low computational complexity. In: INTERNATIONAL CONFERENCE ON ADVANCED TECHNOLOGIES FOR COMMUNICATIONS (ATC 2013), 6., 2013, Ho Chi Minh City. *Anais...* New York: IEEE, jan. 2014, p. 437-442.
- [37] KOBZEV, A. V.; MURZIN, M. V. Application of ring antenna arrays for the phase direction finding of radio signal sources with unknown modulation. In: INTERNATIONAL CONFERENCE ON ANTENNA THEORY AND TECHNIQUES (ICATT), 6., 2015, Kharkiv. *Anais...* New York: IEEE, jun. 2015, p. 1-3.
- [38] Ng, Y. *et al.* Measurement-wise recursive TDoA-based localization using local straight line approximation. In: AUSTRALIAN AND NEW ZEALAND CONTROL CONFERENCE (ANZCC), 1., 2017, Gold Coast. *Anais...* New York: IEEE, fev. 2018, p. 184-189.



- [39] LEE, K.; KWON, H.; YOU, K. TDOA based geolocation using IRLS algorithm. In: INTERNATIONAL CONFERENCE ON INTELLIGENT INFORMATICS AND BIOMEDICAL SCIENCES (ICIIBMS), 2., 2017, Okinawa. *Anais...* New York: IEEE, fev. 2018, p. 92-95.
- [40] AL-TARIFI, M. A.; FILIPOVIC, D. S. On the Assessment of antenna patterns for wideband amplitude-only direction finding. **IEEE Antennae and Wireless Propagation Letters**, v. 17, n. 3, p. 385-388, mar. 2018.
- [41] AL-TARIFI, M. A.; FILIPOVIC, D. S. Amplitude-only direction finding using squinted stabilized-pattern horn antennae in W-band. In: IEEE INTERNATIONAL SYMPOSIUM ON ANTENNAE AND PROPAGATION (APSURSI), 54., 2016, Fajardo. *Anais...* New York: IEEE, out. 2016, p. 1183-1184.
- [42] CAZDEN, J.; FILIPOVIC, D. Wideband amplitude-only direction finding subsystem with conical spirals. In: IEEE INTERNATIONAL SYMPOSIUM ON ANTENNAE AND PROPAGATION & USNC/URSI NATIONAL RADIO SCIENCE MEETING, 55., 2017, San Diego. *Anais...* New York: IEEE, out. 2017, p. 1103-1104.
- [43] LOPEZ, D. G.; FILIPOVIC, D. S. On the design of millimeter-wave antennae for amplitude-only direction finding. In: IEEE INTERNATIONAL SYMPOSIUM ON PHASED ARRAY SYSTEMS AND TECHNOLOGY (PAST), 5., 2016, Waltham. *Anais...* New York: IEEE, jan. 2017, p. 1-8.
- [44] MITROVIĆ, N. M.; PONJAVIĆ, M. M. Multichannel 2-D direction finding based on differential amplitude detection. **IEEE Sensors Journal**, v. 15, n. 9, p. 5064-5070, set. 2015.
- [45] ANAND, S. *et al.* Semi-supervised kernel mean shift clustering. **IEEE Transactions on Pattern Analysis and Machine Intelligence**, v. 36, n. 6, p. 1201-1215, jun. 2014.
- [46] RASPBERRY PI. Teach, learn, and make with Raspberry Pi, 2018. Disponível em: <<http://www.raspberrypi.org>>. Acesso em: 25 maio 2018.